MARTIN MARIETTA ENERGY SYSYEMS LIBRARIES

3 4456 0319970 4

ORNL/TM-11420

ornl

OAK RIDGE
NATIONAL
LABORATORY

MARTIN MARIETTA

Particle Transport in Pellet Fueled JET Plasmas

L. R. Baylor

OAK RIDGE NATIONAL LABORATORY
CENTRAL RESEARCH LIBRARY
CIRCULATION SECTION
4500N ROOM 175
LIBRARY LOAN COPY
DO NOT TRANSFER TO ANOTHER PERSON
If you wish someone else to see this report, send in name with report and the library will arrange a loan.

OPERATED BY
MARTIN MARIETTA ENERGY SYSTEMS, INC.
FOR THE UNITED STATES
DEPARTMENT OF ENERGY

This report has been reproduced directly from the best available copy.

Available to DOE and DOE contractors from the Office of Scientific and Technical Information, P.O. Box 62, Oak Ridge, TN 37831; prices available from (615) 576-8401, FTS 626-8401.

Available to the public from the National Technical Information Service, U.S. Department of Commerce, 5285 Port Royal Rd., Springfield, VA 22161.
NTIS price codes—Printed Copy: A09 Microfiche A01

This report was prepared as an account of work sponsored by an agency of the United States Government. Neither the United States Government nor any agency thereof, nor any of their employees, makes any warranty, express or implied, or assumes any legal liability or responsibility for the accuracy, completeness, or usefulness of any information, apparatus, product, or process disclosed, or represents that its use would not infringe privately owned rights. Reference herein to any specific commercial product, process, or service by trade name, trademark, manufacturer, or otherwise, does not necessarily constitute or imply its endorsement, recommendation, or favoring by the United States Government or any agency thereof. The views and opinions of authors expressed herein do not necessarily state or reflect those of the United States Government or any agency thereof.

ORNL/TM-11420
Dist. Category UC-421

Fusion Energy Division

PARTICLE TRANSPORT IN PELLET FUELED JET PLASMAS

L. R. Baylor

Date published: January 1990

Prepared for the
Office of Fusion Energy
Budget Activity No. AT-10

Prepared by the
OAK RIDGE NATIONAL LABORATORY
Oak Ridge, Tennessee 37831-6285
operated by
MARTIN MARIETTA ENERGY SYSTEMS, INC.
for the
U.S. DEPARTMENT OF ENERGY
under contract DE-AC05-84OR21400

MARTIN MARIETTA ENERGY SYSYEMS LIBRARIES

3 4456 0319970 4

CONTENTS

LIST OF FIGURES v

PREFACE ix

ACKNOWLEDGMENTS xi

ABSTRACT xiii

1. PELLET FUELING OF TOKAMAKS 1

1.1 Introduction to Pellet Fueling 1

1.2 Tokamak Confinement Devices 4

1.3 Pellet Injection in Tokamaks 8

2. MULTIPLE PELLET INJECTION ON THE JET TOKAMAK . . . 12

2.1 JET Tokamak Configuration 12

2.2 JET Multiple Pellet Injection System 16

2.2.1 Pellet injector description 16

2.2.2 Pellet injector installation and operation 18

2.3 Pellet Diagnostics 21

2.4 Plasma Diagnostics 22

2.4.1 Far-infrared interferometer 25

2.4.2 Electron cyclotron emission spectrometer 27

2.4.3 Soft X-ray detector arrays 27

2.4.4 D_α and visible bremsstrahlung detection 30

3. EXPERIMENTAL OBSERVATIONS 32

3.1 Pellet Penetration and Deposition 32

3.2 Pellet Fueling Efficiency 40

3.3 Electron Density Profile Evolution 42

3.4 Heating of Pellet Fueled Plasmas 45

3.5 Energy and Particle Confinement 53

3.6 Impurity Effects 55

4. PARTICLE TRANSPORT IN TOKAMAKS 61

4.1 Classical Transport 61

4.2 Neoclassical Transport in Tokamaks 65

4.2.1 Electron and ion transport 67

4.2.2 Impurity transport 75

4.3 Fluctuation Induced Transport in Tokamaks 77

5. PARTICLE TRANSPORT IN JET PELLET FUELED DISCHARGES 81

5.1 Particle Balance Analysis 82

5.2 Particle Transport Modeling 93

5.2.1 Theoretical foundation 95

5.2.2 Modeling results 98

5.3 Particle Transport Scaling 113

6. ANOMALOUS PARTICLE TRANSPORT 122

6.1 Anomalous Transport Mechanisms 122

6.1.1 Electron drift wave instabilities 123

6.1.2 Ion pressure gradient driven instabilities 126

6.1.3 Magnetic field stochasticity 136

6.2 Calculations of Fluctuation Induced Transport in JET 137

7. DISCUSSION OF RESULTS 150

8. SUMMARY AND CONCLUSIONS 154

LIST OF REFERENCES 157

APPENDIX A PTRANS NUMERICAL METHODS 163

APPENDIX B PTRANS SOURCE CODE LISTING 169

LIST OF FIGURES

FIGURE PAGE

1.1 Schematic representation of a tokamak confinement device 6

1.2 Tokamak geometry and coordinate system 7

2.1 Cutaway view of the JET tokamak 13

2.2 Locations of diagnostic, heating, and fueling systems on JET . . . 15

2.3 Cutaway view of the ORNL multi-pellet injector 17

2.4 Schematic of the pellet injection system installation on JET 19

2.5 View of the ORNL multi-pellet injector as installed on the pellet injection box on JET 20

2.6 Photographs of in-flight pellets fired by the ORNL multi-pellet injector 23

2.7 Data display for a typical pellet from the pellet data acquisition system 24

2.8 Schematic showing lines of sight for three diagnostics in the JET poloidal cross section 26

2.9 Comparison of LIDAR measured electron density profile with the inverted profile from the FIR interferometer data 28

2.10 Contour and 3-dimensional plots of pellet ablation as seen by the vertical soft X-ray camera 29

3.1 Comparison of pellet penetration determination from soft X-ray measurement and D_α measurement 33

3.2 Pellet penetration calculation by the neutral and plasma shielding model compared with measured penetration 34

3.3 The ratio of measured to calculated pellet penetration as a function of pellet speed 36

3.4 Pellet particle deposition and D_α emission for pellets with penetration to 2.85 m 38

3.5 Vertical soft X-ray channel emission during a 6 mm pellet injection event 39

3.6 Fueling efficiency as a function of pellet penetration 41

3.7 Electron density evolution in a pellet fueled discharge 43

3.8 Electron density peaking factor as a function of pellet penetration 200 ms after injection 44

3.9 Electron density evolution of a multi-pellet fueled 4 MA discharge (14960) and a similar gas fueled discharge (14961) 46

3.10 Electron density profile and q profile (from TRANSP) in an ICRF heated pellet fueled discharge 47

3.11 Temporal evolution of plasma parameters with ICRF and NBI heating after pellet injection 49

3.12 Plasma parameters and MHD activity of a pellet fueled discharge with ICRF and NBI heating 51

3.13 The poloidal magnetic field fluctuation level $|\tilde{B}_\theta|$ for $n = 1$ in four 3 MA discharges after 4 mm pellet injection 52

3.14 Plasma stored energy as a function of input power for 3 MA, 3.2 T limiter discharges with ICRF heating 54

3.15 Particle confinement comparison between pellet fueled and non-pellet fueled discharges 56

3.16 Soft X-ray emissivity in a pellet fueled peaked density profile discharge 58

3.17 Plasma parameters and impurity radiation after multi-pellet fueling with peaked density profile 60

4.1 Magnetic well caused by nonuniform magnetic field 66

4.2 Schematic of trapped-particle orbits in a tokamak 69

4.3 Schematic representation of neoclassical particle and thermal diffusivity coefficients (D, χ) as a function of the electron-ion collision frequency (ν^*_{ei}) 74

5.1 The local electron source profile for an NBI and ICRF heated discharge 84

5.2 Results of a particle balance calculation of electron particle fluxes 86

5.3 Electron collisionality parameter ν^*_e in pellet fueled JET discharges 87

5.4 Electron neoclassical (Ware) pinch velocity profile evolution in an ICRF heated, pellet fueled discharge 89

5.5 Results of a particle balance calculation of the effective particle diffusivity in a multi-pellet fueled peaked density profile discharge . 91

5.6 Plot of diffusive particle flux as a function of density gradient during ohmic heating decay of peaked density profile 92

5.7 Comparison of calculated and measured electron density evolution in a multi-pellet fueled discharge 99

5.8 Comparison of calculated and measured electron density evolution in a non-pellet fueled discharge 101

5.9 Particle diffusion coefficient for ohmic and ICRF heated discharges 102

5.10 Comparison of the determined effective diffusion coefficient with the calculated neoclassical diffusion coefficient 103

5.11 Comparison of measured and calculated density evolution using a temperature-dependent diffusion coefficient and neoclassical pinch . 105

5.12 Comparison of measured and calculated density profile evolutions for ohmic and ICRF heated discharges 107

5.13 Density profile evolution calculation sensitivity to variations in diffusivity magnitude 108

5.14 Comparison of density profile evolution for three empirical particle transport models 110

5.15 Effective particle diffusivity (electron) at $r/a = 0.3$ as a function of density profile peakedness 114

5.16 Effective particle diffusivity (electron) at $r/a = 0.3$ plotted as a function of local density and volume-averaged density 116

5.17 Effective particle diffusivity (electron) at $r/a = 0.3$ as a function of local electron temperature 118

5.18 Effective particle diffusivity (electron) at $r/a = 0.3$ as a function of local $\eta_e = L_{n_e}/L_{T_e}$ 119

5.19 Effective electron thermal diffusivity at $r/a = 0.3$ as a function of density profile peakedness 121

6.1 Geometry for an electrostatic drift wave 124

6.2 Experimental η_e profile and calculated η_i^{CRIT} from Romanelli and Briguglio [72] along with temperature and density scale lengths. . . 129

6.3 Experimental particle diffusivity compared with theoretical η_i-mode diffusivities for a peaked density profile pellet fueled discharge . . . 132

6.4 Evolution of the calculated particle diffusivity D and convective velocity v from the Romanelli and Briguglio [72] η_i theory 134

6.5 Evolution of the parameter η_e during the auxiliary heated phase of a pellet fueled peaked density discharge 135

6.6 Profiles of the calculated generalized forces in the quasilinear fluctuation transport theory for an ICRF heated, pellet fueled discharge 143

6.7 Profiles of electron drift frequency and fluctuation amplitude calculated for an ICRF heated, pellet fueled peaked density profile discharge 145

6.8 Profiles of the relative magnitude of the particle flux terms from the quasilinear fluctuation transport theory 146

6.9 Profiles of the experimentally determined electron heat flux and the calculated fluctuation induced heat flux 147

A.1 PTRANS finite difference mesh 166

B.1 Flowchart of the particle transport modeling code PTRANS . . . 171

PREFACE

This document was originally published as a dissertation in partial fulfillment of the requirements for the degree of Doctor of Philosophy in Physics from the University of Tennessee, Knoxville.

ACKNOWLEDGMENTS

There are many people who deserve my thanks for their help in the completion of this dissertation and my graduate studies at the University of Tennessee. I would like to thank Dr. Stan Milora and the Fusion Energy Division of Oak Ridge National Laboratory for providing the opportunity to work at the Joint European Torus (JET) on such an exciting project. My appreciation goes to Steve Combs, Charlie Foust, and the entire crew of ORNL engineers and technicians who designed and built the ORNL multi-pellet injector that was installed on JET. I would like to thank the entire pellet injection group at JET, in particular Drs. Peter Kupschus, Greg Schmidt, Tom Jernigan, Mogens Gadeberg, and David Swain, for their support. I would also like to thank the U.S. Department of Energy and the JET Joint Undertaking for supporting the pellet fueling collaboration and providing such a stimulating environment to work in. I thank my graduate committee and Drs. Wayne Houlberg and Stan Milora for guiding my dissertation research efforts. Finally, I would like to thank my wife Diane and my parents for their constant encouragement throughout my years of full-time employment combined with graduate study.

I would like to recognize the transport modeling work of Dr. R. Hulse of PPPL as having inspired the transport modeling efforts reported here. The use of software developed by Drs. D. Muir and N. Gottardi at JET is gratefully acknowledged. Assistance with the far-infrared interferometer data from Dr. J. O'Rourke is greatly appreciated, as are the efforts of the entire JET operational and experimental teams.

This work is supported by the U.S. Department of Energy under contract DE-AC05-84OR21400 with Martin Marietta Energy Systems, Inc.

ABSTRACT

Pellet fueling experiments have been carried out on the Joint European Torus (JET) tokamak with a multi-pellet injector. The pellets are injected at speeds approaching 1400 m/s and penetrate deep into the JET plasma. Highly peaked electron density profiles are achieved when penetration of the pellets approaches or goes beyond the magnetic axis, and these peaked profiles persist for more than two seconds in ohmic discharges and over one second in ICRF heated discharges. In this dissertation, analysis of electron particle transport in multi-pellet fueled JET limiter plasmas under a variety of heating conditions is described.

The analysis is carried out with a one and one-half dimensional radial particle transport code to model the experimental density evolution with various particle transport coefficients. These analyses are carried out in plasmas with ohmic heating, ICRF heating, and neutral beam heating, in limiter configurations. Peaked density profile cases are generally characterized by diffusion coefficients with a central ($r/a < 0.5$) diffusivity $\sim 0.1\,\mathrm{m}^2/\mathrm{s}$ that increases rapidly to $\sim 0.3\,\mathrm{m}^2/\mathrm{s}$ at $r/a = 0.6$ and then increases out to the plasma edge as $(r/a)^2$. These discharges can be satisfactorily modeled without any anomalous convective (pinch) flux. Auxiliary heated peaked density profile discharges with MHD activity that is measurable at the edge show rapid redistribution of central density which can be explained by temperature-dependent changes in the transport coefficients. Particle balance calculations of particle diffusivity in the plasma core region show a reduction in diffusivity with density peakedness. Correlation with locally determined η_e shows a general increase in diffusivity as η_e increases above ~ 1.5. In

all cases, neoclassical particle diffusion coefficients are substantially smaller than the determined values.

Fluctuation induced transport is frequently suggested as the mechanism for the anomalous particle and heat fluxes in tokamaks. As part of our analysis, we compare the calculated anomalous electron particle and heat fluxes with the theoretical fluxes from the neoclassical quasilinear formulation of fluctuation induced transport using electron and ion drift waves as the dominant fluctuation mechanism. The Onsager symmetry found in this fluctuation induced transport theory is then used to examine the correlation between the anomalous electron particle and heat flux.

CHAPTER 1

PELLET FUELING OF TOKAMAKS

The task of fueling a magnetically confined fusion plasma has become one of many problems that need to be solved to satisfy the requirements for the attainment of an economical power producing fusion reactor. In a reactor there will be a continuous loss of fusion fuel due to containment losses and fusion reactions. These losses of fuel particles will have to be replenished by the injection of fuel mass to keep the reacting plasma ignited. One method of injecting fuel mass that has been developed is the injection of a high speed pellet of solid fuel.

1.1 Introduction to Pellet Fueling

In this section we introduce the physics aspects of fueling magnetically confined hydrogenic plasmas with frozen pellets of deuterium. The injection of solid deuterium pellets for the fueling of a plasma was first advocated by Spitzer [1] in 1954. He argued that injection of pellets of fuel would be more efficient than gas puffing fuel close to the walls of the device, as these particles would be the first to be lost from the containment volume. Since that time, plasma fueling by injection of frozen hydrogenic pellets at high speed has been proposed and used to overcome the limitations of edge gas puff fueling. The technical development of pellet injectors and their use on plasma confinement devices has advanced to the point of being able to demonstrate the capacity to fuel a plasma and even improve plasma performance. A neutral pellet with speeds of a few hundred meters per second will easily penetrate the scrape-off layer plasma and penetrate into the

confining magnetic fields to deposit virtually all of its particles in the main discharge as it completely evaporates from the plasma heat. Pellet fueling has thus become one of the primary methods available to replenish the charged particles that constitute the plasma as they are lost from the containment volume.

In addition to pellet fueling, edge gas puffing, wall recycling, and neutral beam injection (NBI) make up the fueling mechanisms in the present day set of experimental plasma confinement devices. Recycling is the process of material surfaces absorbing fuel gas and releasing it back into the plasma. Edge gas puffing and wall recycling are similar in that neutral hydrogenic gas (the fuel) originates near the solid surfaces that surround or are in contact with the plasma. Gas puffing is accomplished by injecting gas through an electronically controlled small orifice valve near the plasma edge. The valve is either preprogrammed or servo controlled to maintain a preset plasma density. Recycling always plays an important role in fueling through particle trapping and diffusion in the wall and limiter which then eventually desorb and release cold gas. Neutral beam injection provides a fuel source, but the source rate is not very large and the beam penetration is reduced with higher density, and therefore less fueling is accomplished in the plasma center.

The neutral gas at the edge from gas puffing and recycling is transported into the plasma by a diffusion-like movement. Charge-exchange processes act to perpetuate the existence of a neutral particle, but ionizations destroy the neutral. In tokamak plasmas with a large radius, very few neutrals reach the core of the plasma, and therefore charged particle transport must be responsible for central plasma fueling. The inward charged particle transport in tokamaks has been proposed to be the result of an inward particle convection that can be anomalously larger than the theoretically predicted convection due to collisional transport and

is not yet completely understood. Since this process is not fully understood, there is some question as to whether the transport mechanism responsible for inward charged particle transport in experimental devices will scale to reactor conditions. This makes it uncertain whether edge gas puffing would be able to fuel a plasma under reactor conditions.

Although gas puffing is much simpler than pellet fueling or NBI, its efficiency for fueling has been shown to have limitations. During gas puffing, large quantities of the fuel (up to 80%) end up embedded in the limiter and wall of the vacuum chamber, reducing the fueling efficiency to as low as 20%. Pellet fueling deposits the fuel in the confined plasma rather than the recycling layer at the plasma edge and therefore has a much higher fueling efficiency. The pure fuel of the pellet also dilutes the impurities in the plasma and may reduce the impurity influx that is related to the recycling process. A final advantage to pellet fueling is the capability of controlling and peaking the density profile by tailoring the local deposition to obtain an advantageous shape.

Replenishment of the charged particles that constitute the plasma is required on the order of the characteristic particle confinement time given by

$$\tau_p = \frac{N_p}{-dN_p/dt}, \tag{1.1}$$

where $-dN_p/dt$ is the loss rate of plasma particles and N_p is the total number of plasma particles (electrons) in the absence of fuel sources. Measurement of τ_p as defined is virtually impossible because the continuous influx of plasma particles and neutrals from the surrounding walls gives rise to a residual source of fuel that cannot be entirely eliminated. The relationship between the confinement time τ_p and the fueling rate ϕ can be written as

$$\frac{dN_p}{dt} = -\Gamma A + \phi_R + \phi_g + \phi_p \tag{1.2}$$

$$= -\frac{N_p}{\tau_p} + R(t)\frac{N_p}{\tau_p} + \phi_g + \phi_p$$

$$= \frac{-N_p}{\tau_p^*} + \phi_g + \phi_p,$$

where $\tau_p^* = \tau_p/[1 - R(t)]$ and $R(t)$ is the global recycling coefficient which is defined as the fraction of particles lost to the limiter and wall that return to the plasma containment volume. The terms ϕ_g and ϕ_p are the influx of particles from gas puff and pellet fueling, respectively, Γ is the outward particle flux, and A is the plasma surface area.

A number of questions remain regarding pellet fueling of fusion relevant devices. Some of these questions are: what effect does pellet penetration have on plasma performance, what improvements do pellet fueled plasmas demonstrate for particle and energy confinement over gas puff fueled plasmas, can pellets fuel the central plasma sufficiently to make an impact on fusion reactions, what is the maximum permissible pellet size, and can repetitive pellet fueling sustain a steady-state plasma. These are all questions that the current set of pellet fueling experiments on JET are designed to address.

1.2 Tokamak Confinement Devices

The tokamak confinement device is now the most advanced magnetic confinement concept. Current operating tokamaks obtain well confined, stable plasmas with densities and temperatures approaching those required for fusion breakeven (where the fusion power output equals the input power). There are still, however, many problems that remain to be solved to reach the performance required for a safe, reliable, and economical power producing fusion reactor. In this section we describe the fundamental features of tokamaks, which have been extensively reviewed in the literature [2–5].

The tokamak (a Russian acronym for toroidal chamber of magnetic coils) is a toroidally shaped plasma confinement device that uses a toroidal electric field to break down a gas in the toroidal vacuum chamber. As shown in Fig. 1.1, the toroidal plasma is confined in a helical magnetic field produced by the superposition of a strong toroidal field, B_ϕ, generated by external coils, and a poloidal field, B_θ, produced by a current driven within the plasma itself. The toroidal geometry and coordinate system of the tokamak are shown in Fig. 1.2. The variables r, θ, and ϕ are the radial coordinate, the angle in the poloidal direction, and the angle in the toroidal direction, respectively.

The toroidal plasma current is derived from the transformer action of a primary coil on the inside of the torus which changes the magnetic flux that links the toroidal plasma and produces a toroidal electric field. The resulting toroidal electric field drives the plasma current, thus producing the poloidal magnetic field. The poloidal magnetic field within the plasma provides a radially inward ($-\hat{r}$) equilibrium force to balance the outward expansion forces. The poloidal field is smaller than the toroidal field in order to meet the Kruskal-Shafranov criterion [2] for stability from helical perturbations, which in circular geometry is

$$q(a) = \frac{aB_\phi(a)}{R_0 B_\theta(a)} > 1, \tag{1.3}$$

where q is the "safety factor" (defined as the number of times a magnetic field line winds toroidally, divided by the number of times it winds poloidally), a is the minor radius, R_0 the major radius, m is the minor azimuthal mode number, and n is the toroidal mode number. At rational surfaces, $r = r_s$, the magnetic field lines close on themselves, and the safety factor satisfies the condition

ORNL–DWG 90-5577

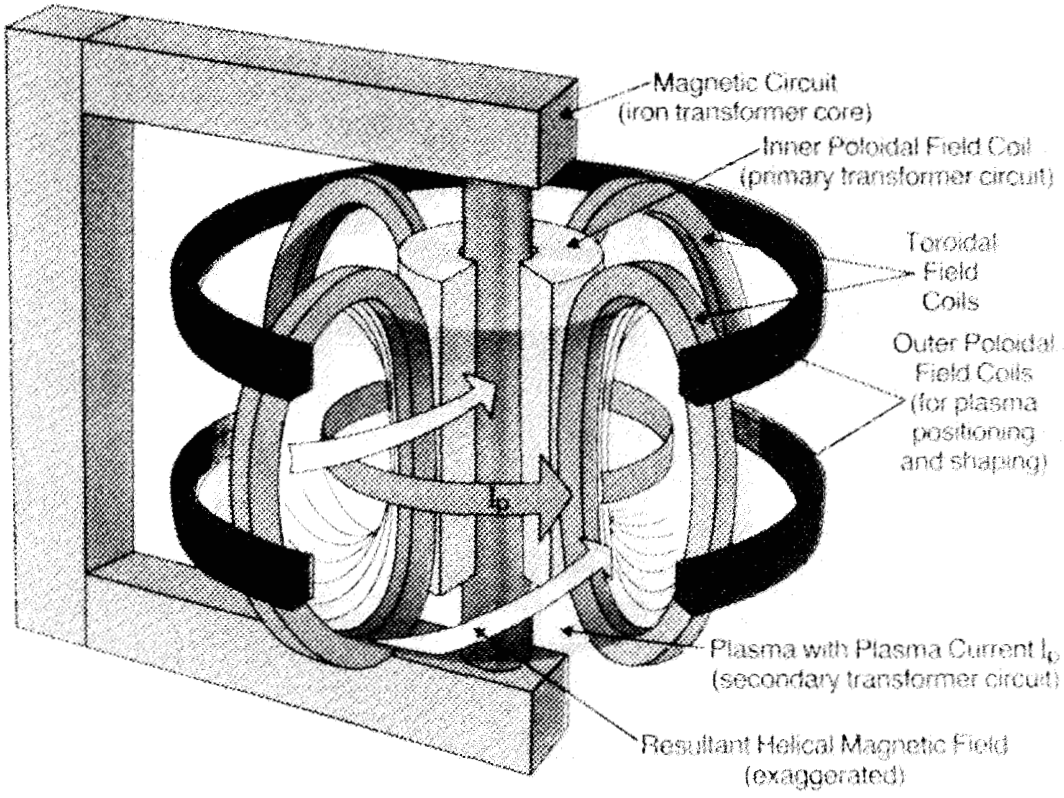

Fig. 1.1 Schematic representation of a tokamak confinement device. This figure shows the pulse transformer used to induce a plasma current I_p parallel to the large externally applied toroidal field B_ϕ. Outer poloidal field coils shape the cross-section of the current carrying plasma ring and maintain it in radial and vertical equilibrium. Not shown is the vacuum vessel inside the toroidal field coils. Figure courtesy of JET Joint Undertaking.

ORNL-DWG 89M-2916 FED

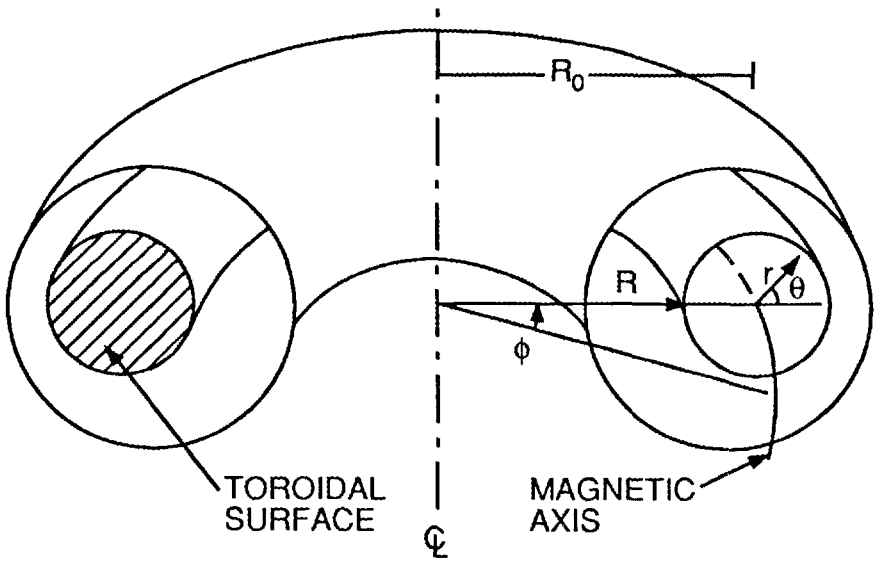

Fig. 1.2 Tokamak geometry and coordinate system.

$q(r_s) = m/n$, with m and n being integers. A vertical magnetic field, generated from toroidally wound coils, is also applied to counter the outward $(+\hat{r})$ expansion tendency of the entire plasma produced by (1) the plasma pressure gradient, (2) poloidal current crossed with the toroidal magnetic field, and (3) toroidal current crossed with the poloidal magnetic field. This vertical field strengthens the poloidal magnetic field on the outside of the torus and weakens it on the inside, hence causing the inner magnetic surfaces to be shifted out relative to the outer surfaces.

Ohmically heated tokamaks typically reach an electron temperature of 1–3 keV. Because the electrical conductivity is proportional to $T_e^{3/2}$, Joule heating becomes less effective at higher temperatures. It follows that auxiliary heating

is required to reach the necessary temperatures for breakeven energy from D-T reactions ($\sim$ 10 keV). The primary methods used in tokamaks for auxiliary heating are injection of neutral particle beams that give up their energy through collisions primarily with the ions and ion cyclotron radio frequency (ICRF) wave heating that couples energy to particles (ions) in resonance with the wave; their subsequent collisions transfer this energy to the nonresonant particles (electrons).

1.3 Pellet Injection in Tokamaks

In this section, we examine the general results of pellet injection experiments that have been done on tokamaks. Detailed reviews have been published in the literature [6,7].

The first pellet injection experiments on a tokamak were done at Oak Ridge National Laboratory on the Oak Ridge Tokamak (ORMAK) [8] in 1976. Since that time, studies of pellet fueling have been performed on a number of tokamak devices, including ISX-A [9], ISX-B [10], PDX [11], Alcator-C [12], TFTR [13,14], ASDEX [15,16], Doublet III [17,18], and TFR [19]. These studies have shown that substantial fueling of particles can be accomplished with pellets that have speeds in excess of a few hundred meters per second. Increases in plasma mass by as much as 100% of the pellet mass have been observed, and increases in particle confinement time, τ_p, and energy confinement time, τ_E, have also been observed. In the Alcator-C experiments, τ_E in pellet fueled plasmas showed an improvement over gas puffed discharges, and at very high densities led to record values of $\bar{n}_e\tau_E$ beyond the Lawson criterion limit [12]. The beneficial improvements in confinement properties that have been observed experimentally on several tokamaks are generally associated with modification to the plasma density and/or temperature profiles as a result of the pellet particle deposition profile.

Particle transport after pellet injection in ohmic plasmas gives a relatively homogeneous picture. The global particle confinement time is increased compared to edge fueled cases, partly as a consequence of the deeper fueling. In cases where pellet injection is accompanied by reasonably low edge recycling, the plasma density builds up much faster and significant changes in the particle diffusion coefficient D and inward particle convection v have been seen [12,16]. The density profile has been seen to modestly peak on axis with moderate or even shallow pellet penetration in multiple pellet fueled plasmas [16,17]. The complete physical explanation for this phenomenon has yet to be determined. Peaked density profiles following pellet injection are frequently seen to be followed by an accumulation of impurities in the center. The increase in density seems to be limited by these impurities, which radiate away substantial power. In most cases analyzed, the plasma energy confinement has shown similar behavior to the plasma particle confinement. Improved global energy confinement times in ohmic plasmas are always accompanied by buildup of average density and especially central density by the pellets. At high densities, the energy confinement time of gas puffed discharges saturates, while pellet fueled discharges have exhibited improved confinement [12]. In some cases, improvements of 70% relative to gas fueling have been reported, particularly in ohmically heated discharges. The potential for improving the confinement properties of the plasma and the benefits from such improvements have generated a high level of interest in pellet fueling. While the cause of the enhanced confinement has not been identified conclusively, it is apparently associated with a central peaking of the plasma density profile and/or a reduction in recycling of ions in the plasma edge region. Strong peaking of the plasma density profile is accomplished in present experiments as the high speed pellet penetrates the plasma and deposits fuel preferentially in the hotter,

denser central plasma core, where the ablation rate of the hydrogenic pellet is greatest.

Various pellet ablation models [20–23] have been proposed to predict the pellet penetration and lifetime in the plasma. Comparison of experimental studies of pellet ablation with theory demonstrates that pellets are shielded from the hot electrons of the plasma. The neutral shielding theory of pellet ablation and the neutral and plasma shielding theory have been used successfully to model pellet ablation in several experiments [24–26]. In these models, the incident plasma electrons interact with the ablated particles, which expand spherically with high density and low temperature near the pellet surface, and the ablated particles flow along the magnetic field lines. The pellet surface is protected by a neutral gas shield, with a thickness given by the hydrodynamic solution of the gas expansion assuming spherical symmetry, and by a tube of cold ionized plasma, which extends along the magnetic field. The incident electrons provide the dominant heat flux because they have a much larger velocity than that of the ions. The heat flux to the pellet surface is calculated from convective flows of electrons along the magnetic field through both the tube of cold plasma and the dense neutral gas shield and fast neutral beam ions normal to the magnetic field only through the neutral gas shield, which they can enter since their gyro-orbits are larger than the effective pellet ionization radius.

The deposition of particles into the plasma from the pellet is related to the change in pellet radius through the approximate expression from the neutral gas shielding model (for deuterium) [21] given in terms of the local electron temperature T_e (eV) and plasma electron density $n_e\,(\mathrm{m}^{-3})$ as:

$$\frac{dN}{dt} = -8\pi n_s {r_p}^2 \frac{dr_p}{dt} = 1.5 \times 10^{18}\, n_e^{1/3}\, T_e^{1.64}\, r_p^{4/3} \quad \text{(atoms/s)}, \qquad (1.4)$$

where $n_s = 3.1 \times 10^{28}\ \mathrm{m}^{-3}$ is the molecular number density of the solid pellet and r_p is the pellet radius in meters. This differential equation must be solved at each location in the plasma to keep track of the pellet radius. This expression, which is valid in the high-temperature regime ($T_e > 1$ keV), forms a qualitative scaling law taking into account shielding from the neutral gas cloud around the pellet. If the injection velocity is high enough to permit penetration to the plasma center, the strong electron temperature dependence will ensure a centrally peaked ion source term.

Pellet fueled tokamak plasmas have been shown to give improved plasma performance and greatly extend the experimental parameter space and thus contribute to a better understanding of plasma transport phenomena. The prospect of higher energy and particle confinement due to more central deposition of fuel particles might open the possibility of maximizing the fusion performance at higher $\bar{n}_e$ as obtained with pellet fueling. Experiments with pellet fueling on the present-day larger tokamaks such as JET will hopefully resolve some of the remaining questions and enable the extrapolation of pellet fueling results to the next generation of ignition devices. These results may then help us determine whether pellet fueling will be necessary to supply the makeup fuel in a fusion reactor.

CHAPTER 2

MULTIPLE PELLET INJECTION ON THE JET TOKAMAK

2.1 JET Tokamak Configuration

In this section we describe the JET tokamak in its configuration during the multiple pellet injection experiments. The Joint European Torus (JET) is currently the largest tokamak plasma confinement device in the world [27]. The JET tokamak shown in Fig. 2.1 can drive a toroidal plasma current of up to 7 MA, which resistively heats the plasma to temperatures of a few keV. In addition to ohmic heating, JET also has available 20 MW of ion cyclotron resonance frequency (ICRF) heating and 20 MW of neutral beam injection (NBI) heating that are needed to reach the relatively high plasma temperatures required for fusion breakeven (where the fusion energy produced equals the energy used to heat and confine the plasma).

The toroidal magnetic field on JET is generated from 32 D-shaped copper coils that produce a maximum of 3.5 T at the magnetic axis. The vacuum vessel of JET during the initial pellet fueling experiments was covered with graphite tiles and coated with carbon to provide a low-Z material wall boundary to the plasma. The inner wall was covered with armored carbon tiles, and the outer wall has two water-cooled toroidal belt limiters approximately 1 m above and below the horizontal midplane. The wall and limiters were coated with evaporated beryllium in the later pellet fueling experiments in 1989. Eight ICRF antennas sit between the belt limiters on the outer wall. Each antenna is surrounded by

ORNL-DWG 90-5578

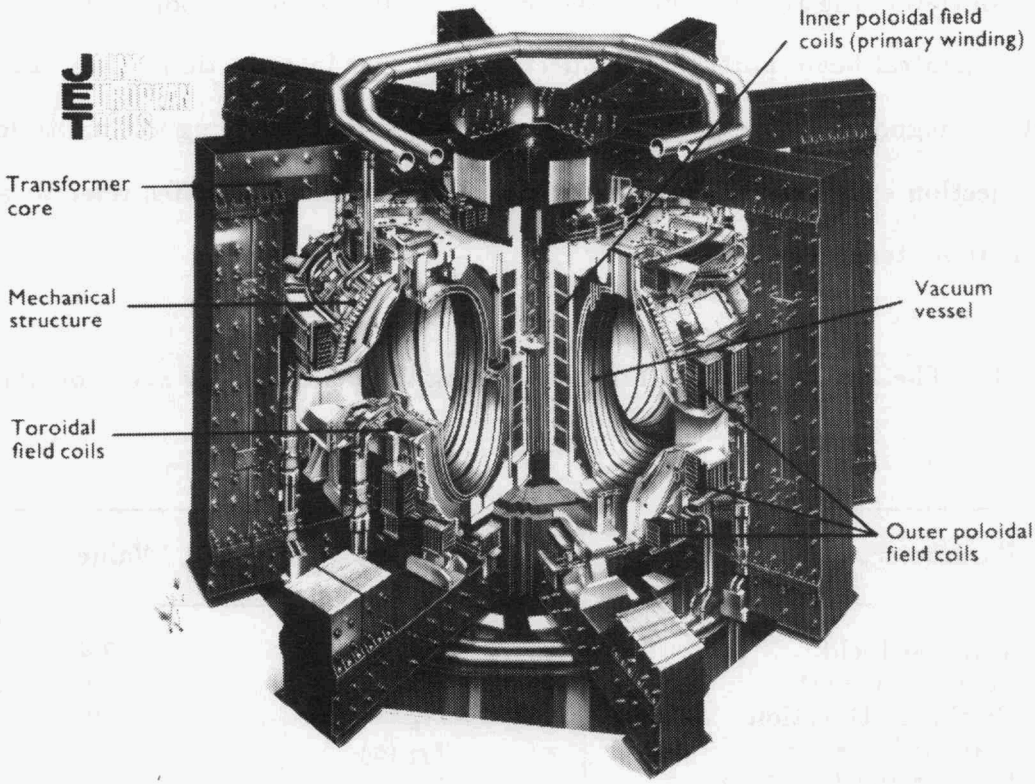

Fig. 2.1 Cutaway view of the JET tokamak. Figure courtesy of JET Joint Undertaking.

water-cooled carbon tiles and has a carbon-coated nickel screen. The plasma fuel is provided by a programmable gas introduction system which puffs in gas at rates up to $\simeq 1 \times 10^{22}$ particles per second. The NBI heating system also provides a particle source of approximately 1×10^{20} neutrals per megawatt of power injected into the plasma.

A plan view of the JET vacuum vessel in Fig. 2.2 shows the locations of the RF antennas, neutral beam ports, pellet injection port, gas introduction valves, and important diagnostics. The parameters of the JET tokamak during the multiple pellet injection experiments are given in Table 2.1. The coordinates refer to a vessel at room temperature.

Table 2.1 The JET tokamak parameters during the pellet fueling experiments.

Parameter	Symbol	Value
Toroidal Field	B_t (T)	≤ 3.4
Plasma Current	I_p (MA)	≤ 7.0
Discharge Duration	t_p (s)	≤ 30
Flattop Duration	t_{ft} (s)	≤ 20
RF Heating Duration	t_{rf} (s)	≤ 20
Minor Radius (Horizontal)	a (m)	1.2
Plasma Major Radius	R_0 (m)	2.96
Plasma Aspect Ratio	R_0/a	≥ 2.37
Plasma Elongation	b/a	≤ 1.68
Electron Temperature	T_e (keV)	≤ 12
Electron Density	n_e (m^{-3})	$\leq 2 \times 10^{20}$
ICRF Power	P_{RF} (MW)	≤ 20
NBI Power	P_{NB} (MW)	≤ 20

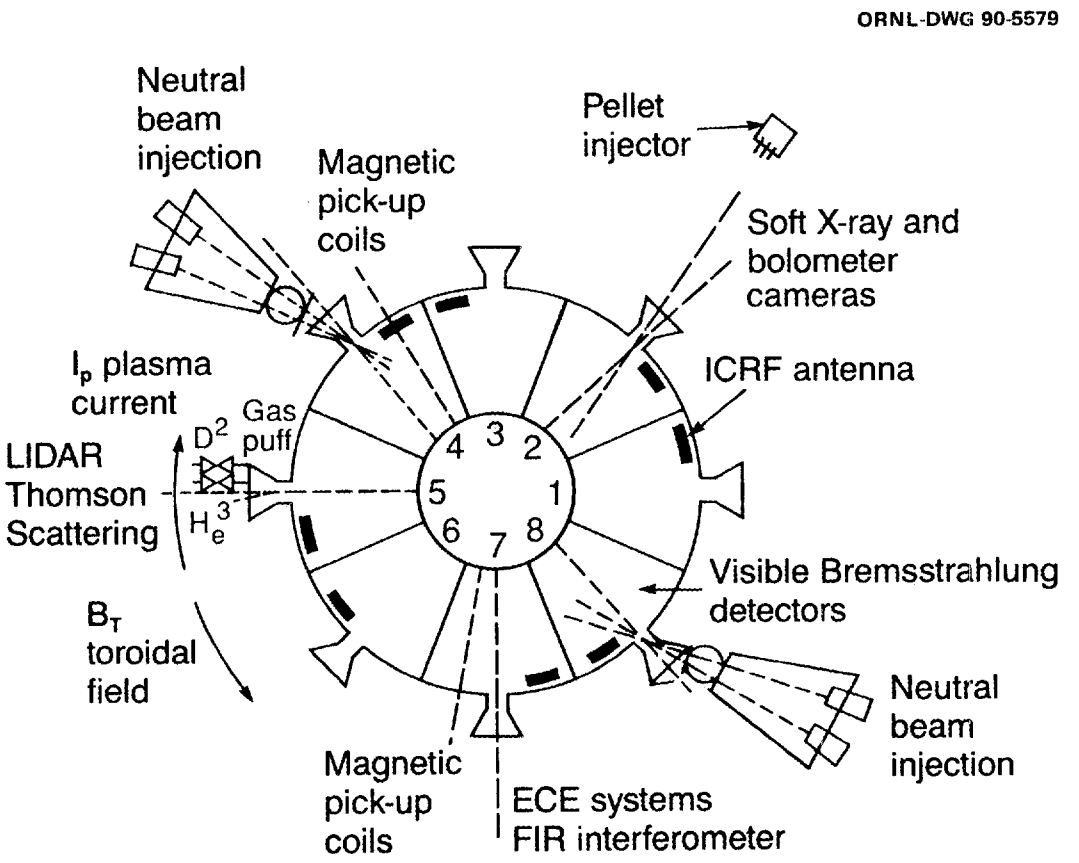

Fig. 2.2 Locations of the diagnostic, heating, and fueling systems on JET.

2.2 JET Multiple Pellet Injection System

In 1986 the United States Department of Energy and the JET Joint Undertaking began an international pellet fueling collaboration that provided for a multiple pellet injector to be designed and built at Oak Ridge National Laboratory (ORNL) for pellet fueling experiments on JET. The injector was installed on JET in May 1987 and, after an initial commissioning period, was used in a series of pellet fueling experiments through 1989. This dissertation is the result of analysis on the first year and a half of experiments carried out with the ORNL injector by a joint team of U.S. and JET scientists.

2.2.1 Pellet injector description

The ORNL multiple pellet injector is a repeating pneumatic injector with three independent guns and has been described by Combs and Milora [28,29]. The three guns produce multiple right cylinder pellets of frozen deuterium that nominally have a diameter and length of 2.7 mm, 4 mm, and 6 mm. An artist's depiction of the injector in cutaway view is shown in Fig. 2.3. The maximum repetition rates of the guns are 5 Hz, 2.5 Hz, and 1 Hz, respectively, for quasi-steady-state conditions ($>$ 10 s). The approximate number of deuterium atoms contained in each size pellet based on ideal size is 9.29×10^{20}, 3.08×10^{21}, and 1.04×10^{22}, respectively, using $20.089 \times 10^{-6}\,\mathrm{m}^3/\mathrm{mol}$ as the molar volume of deuterium at a temperature of 14 K [30].

The principle of operation of the injector is pneumatic acceleration. Each of three independent injectors is cooled by liquid helium to below 20 K to condense deuterium to a solid slush which is then extruded past a chambering mechanism by a motor-driven piston. A solenoid-driven chambering mechanism cuts a

ORNL-DWG 87-2148 FED

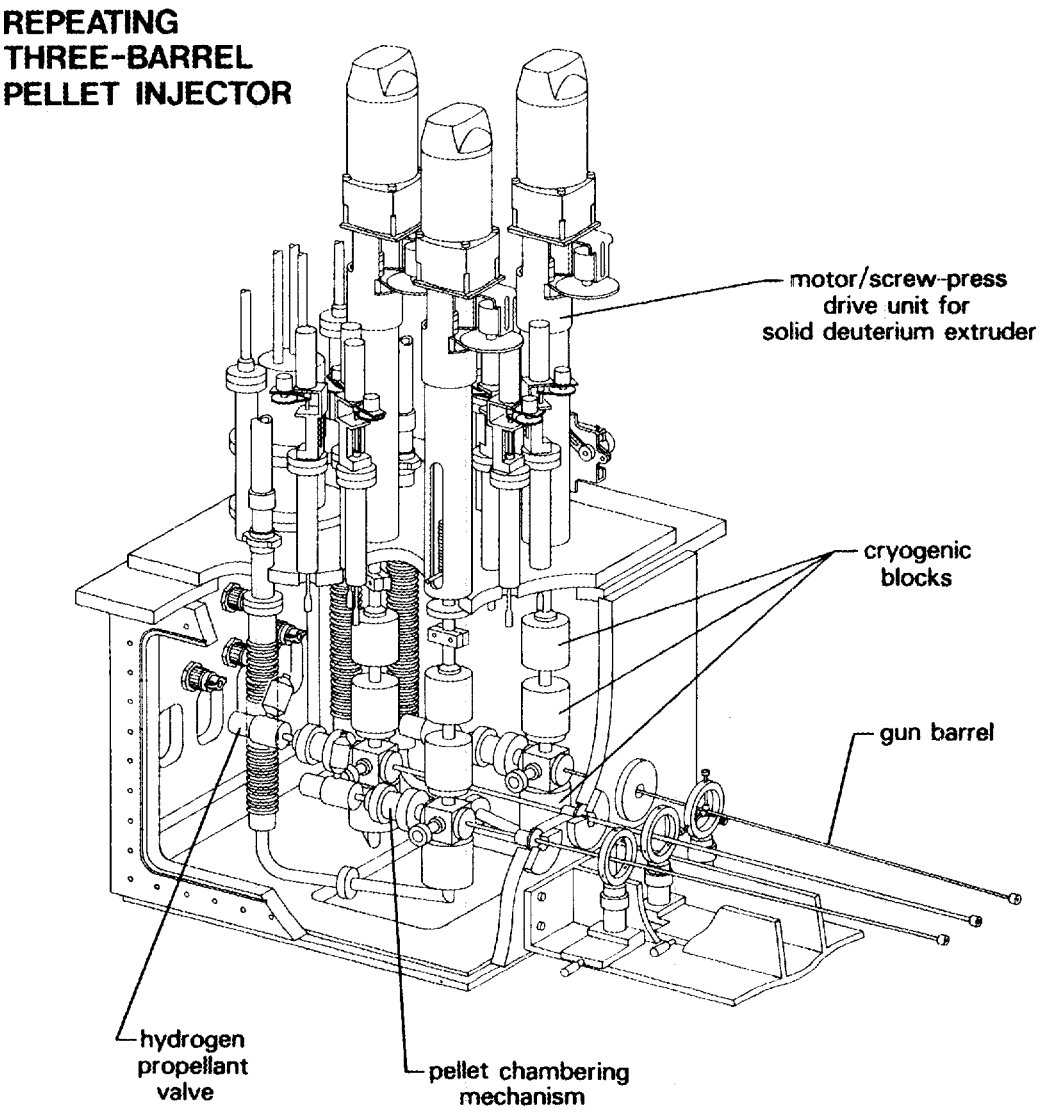

Fig. 2.3 Cutaway view of the ORNL multi-pellet injector.

cylindrical pellet out of the extrusion and loads the pellet into the barrel milliseconds before the pellet is fired. A high-pressure fast solenoid valve is operated when the chambering mechanism is engaged and propellant gas (typically 70 bar hydrogen) accelerates the pellet down the barrel. The hydrogen propellant gas and deuterium fuel gas are introduced to the injector through a gas manifold which regulates pressures and allows purging of the system between operations. A 100 ℓ/s turbomolecular pump is used to keep the injector enclosure pressure well below 10^{-3} mbar.

2.2.2 Pellet injector installation and operation

The injector is installed on the JET tokamak on the rear panel of a large cryocondensation pump box known as the Pellet Injection Box (PIB). The PIB is mounted to a horizontal midplane port on JET through a 6 in. diameter line through which the pellets are injected. Inside the 50 m^3 PIB is a liquid helium cryopump with a pumping speed of 8.6×10^6 ℓ/s for H_2. The PIB provides pumping to prevent the propellant gas following the pellet (approximately 30 bar $\cdot$ ℓ of hydrogen) from reaching the tokamak plasma, and it pumps the excess solid deuterium extruded through each gun during a firing sequence of pellets (approximately 5 bar $\cdot$ ℓ per extrusion). A flow restrictor tube (6 cm diameter, 1 m long) for each gun is also located at the exit of the PIB to limit the gas flow to 60 ℓ/s. A schematic representation of the pellet injection lines through the PIB is shown in Fig. 2.4, and Fig. 2.2 shows where the PIB is connected to the tokamak. A photograph of the pellet injector installation on the rear of the PIB is shown in Fig. 2.5. A detailed account of the pellet injector interface to the JET machine is given by Kupschus in Ref. [31].

The injector is operated through a stand-alone control and data acquisition system that is based on a programmable logic controller (PLC) and a Digital

ORNL-DWG 90-7780

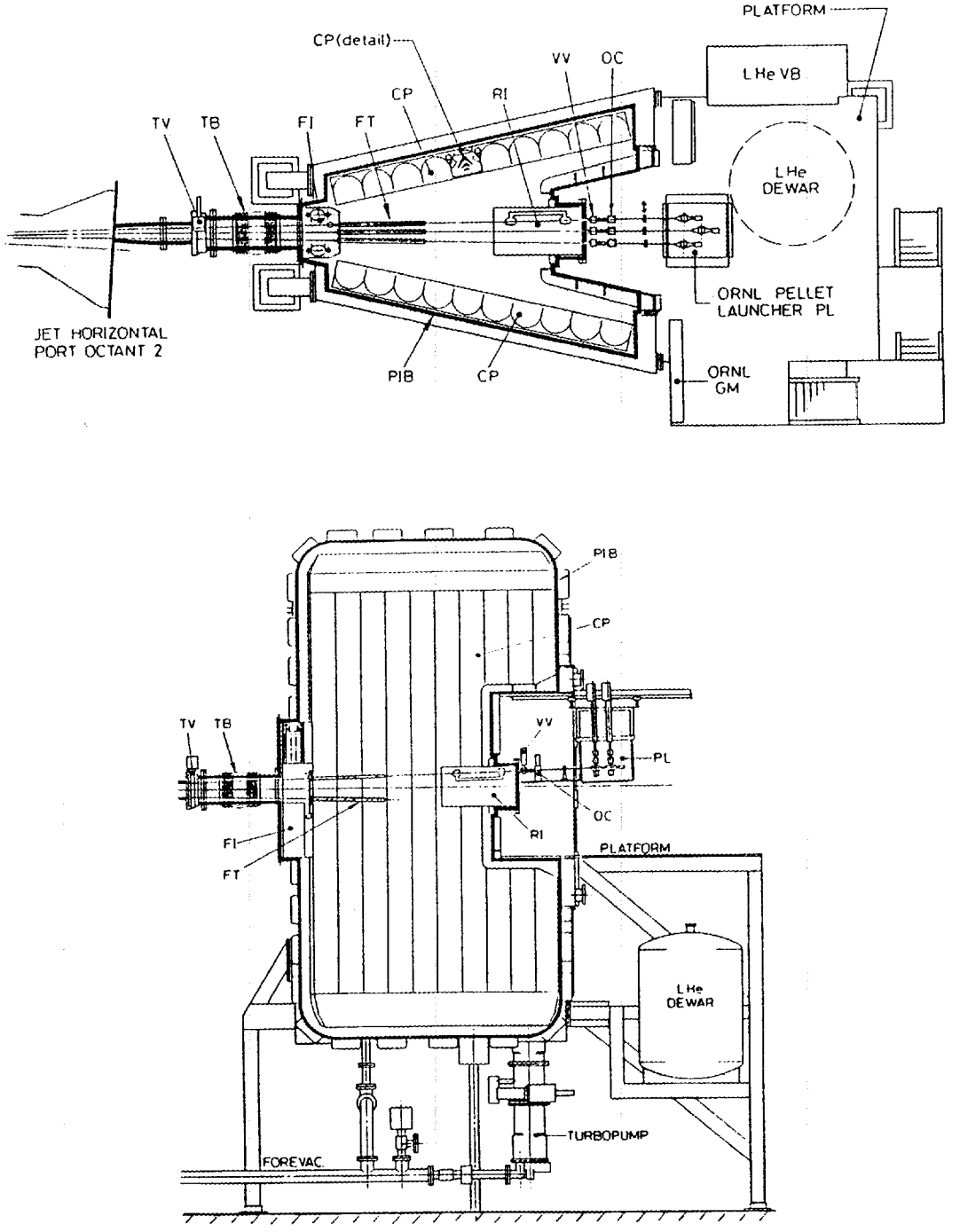

Fig. 2.4 Schematic of the pellet injection system installation on JET. The top illustration is a plan view and the bottom is an elevation.

ORNL/PHOTO 100-90

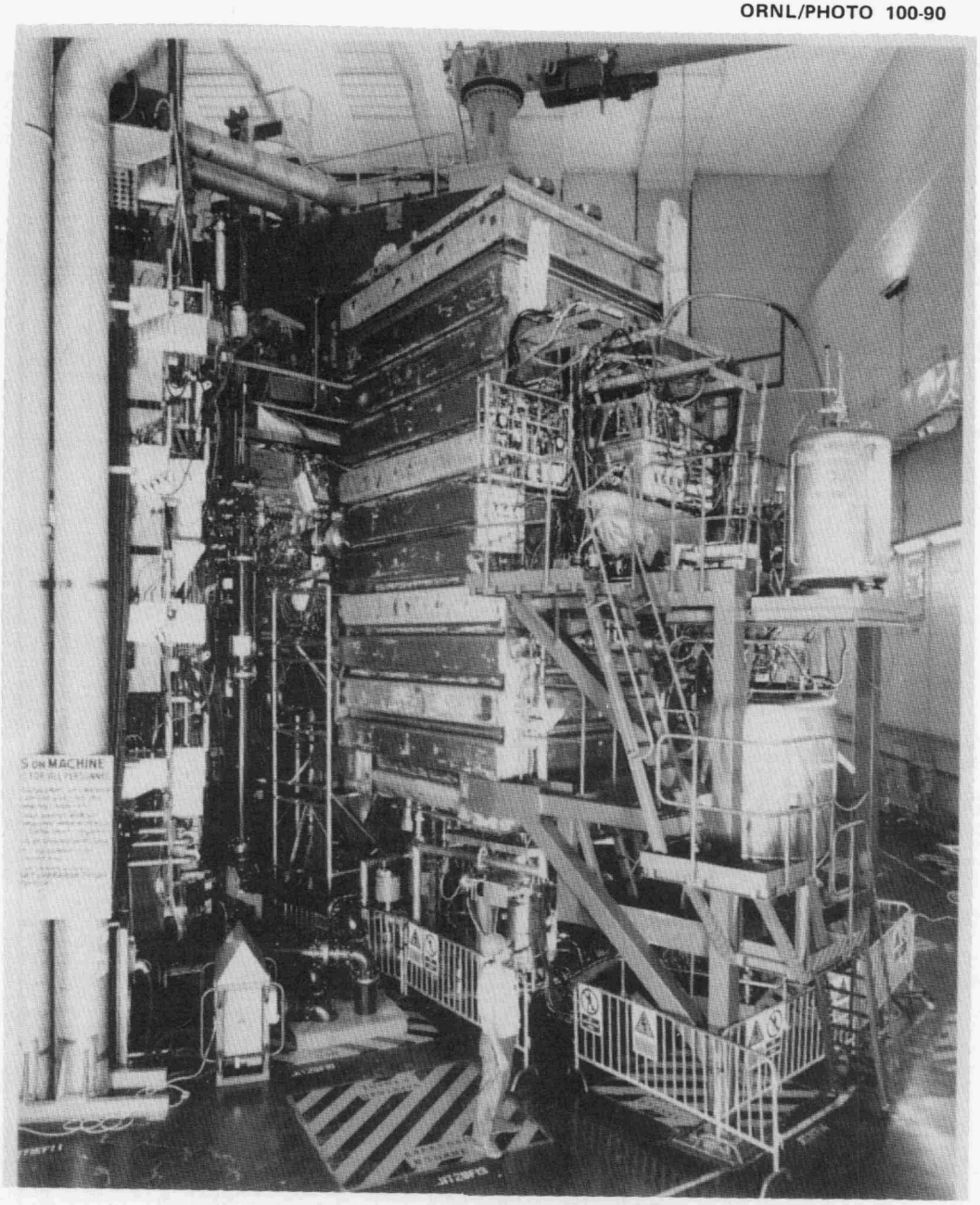

Fig. 2.5 View of the ORNL multi-pellet injector as installed on the pellet injection box on JET. Photograph courtesy of JET Joint Undertaking.

Equipment Corporation MicroVAX II computer [32, 33]. The computer uses a CAMAC link to transmit operator commands through an RS-232 CAMAC module to the PLC, display injector status on CAMAC driven color graphic mimic displays, acquire data from transient digitizers, and transfer commands and data to the JET Control and Data Acquisition System (CODAS) computers. The firing of pellets is controlled by a microcomputer based firing sequencer which sends precise timing pulses to the power supplies that drive the injector mechanisms and also sends clocking pulses to the transient digitizers. Once a pellet firing sequence is programmed in, the operation of the injector is automatically controlled through the discharge including a real-time protection system that monitors important plasma parameters and will inhibit pellet injection if it threatens plasma operation. The transient data collected from pellet diagnostics are used to determine pellet speed, mass, and pellet penetration depth into the plasma. These data are archived with the JET experimental data on the JET mainframe computer.

2.3 Pellet Diagnostics

The JET multi-pellet injection system has diagnostics for measuring pellet parameters and injector performance. These diagnostics consist of a video monitor of the extrusion to check the quality of the ice, a barrel pressure transducer, an accelerometer on the injector chambering mechanism, a fiber-optic pellet interrupter triggering system, a microwave bridge for determining pellet mass, and a photodiode for measuring pellet ablation line emission. The double microwave cavity bridge is a direct measure of the pellet mass [34]. The fiber-optic interrupter triggering system is used to trigger a flash lamp and video frame store camera system to provide shadow-graph pictures of the pellets in flight. Typical

video pictures of the three sizes of pellets in flight after they leave their respective barrels of the injector are shown in Fig. 2.6. The speed of the pellet is determined from the time delay between the fiber-optic interrupter trigger signal and the microwave bridge signal of the first cavity.

The photosensitive diode is attached to the bottom of the torus through a periscope and is used to measure the Balmer alpha (D_α) line emission from the ablation of the pellet, i.e., the red line of the Balmer series at 6563 Å, corresponding to the transition between the upper quantum state $n = 3$ to the lower state $n = 2$. The fiber-optic trigger, microwave bridge, and D_α signals are summed through a summing amplifier and digitized at a 1 MHz sampling rate with a LeCroy 8210 transient digitizer. A typical set of data taken by the pellet data acquisition system for an injected pellet is shown in Fig. 2.7. A timing signal corresponding to the time the pellet crosses the limiter is generated electronically from the pellet speed measurement and is shown in the D_α trace of Fig. 2.7. The penetration is then determined by the time duration from the limiter timing signal to the end of the D_α signal.

Measurements of the pellet diagnostics have provided useful performance data from the large number of pellets fired. In particular, the pellet speed from the guns is typically $\sim$ 1230 m/s at an operating pressure of 70 bar and is quite consistent. The pellet mass is similarly quite consistent, with over 85% of the pellets during a typical 240 pellet run having a mass within $\pm 5\%$ of the average.

2.4 Plasma Diagnostics

The JET experiment has been built with a comprehensive set of plasma and machine diagnostics which produce high-quality data. A general survey of these

ORNL/PHOTO 101-90

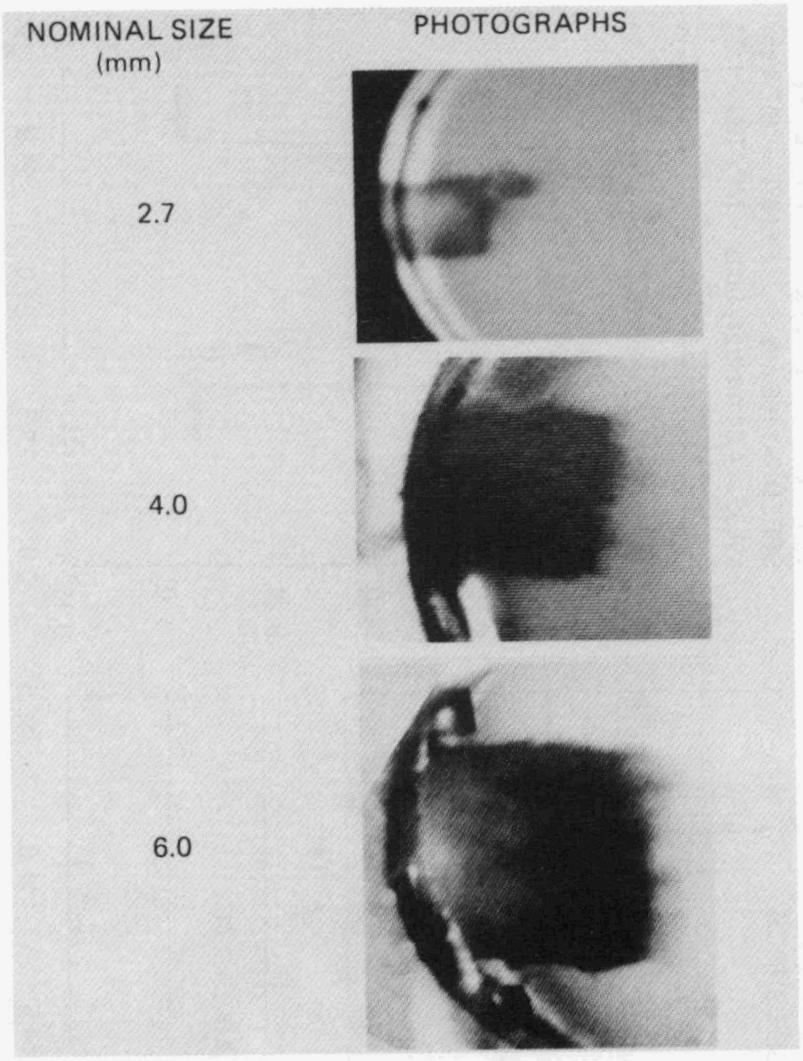

Fig. 2.6 Photographs of in-flight pellets fired by the ORNL multi-pellet injector. The shadow photographs were taken 20 mm from the end of the gun muzzles.

ORNL-DWG 89M-2819 FED

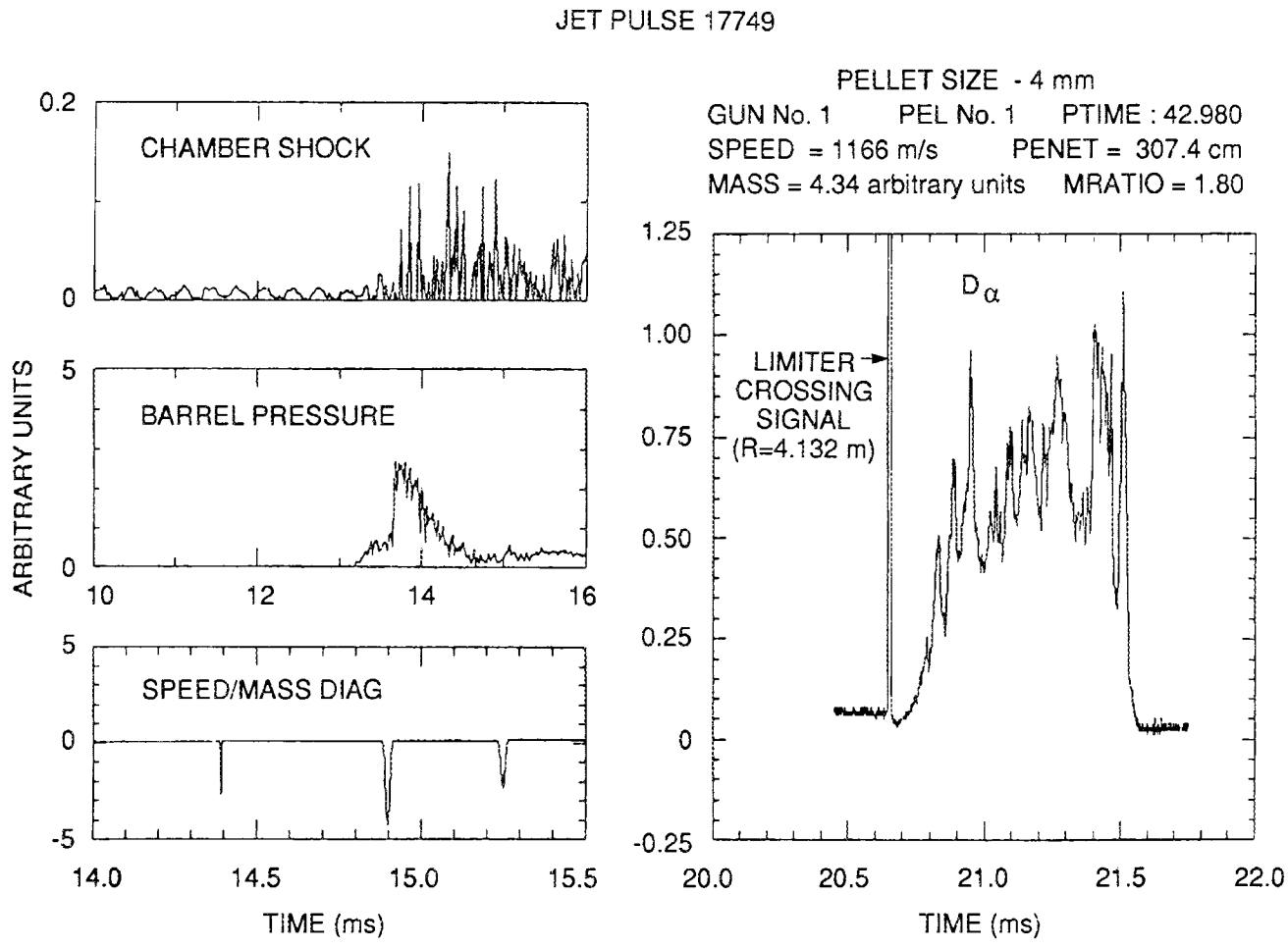

Fig. 2.7 Data display for a typical pellet from the pellet data acquisition system.

diagnostics and the data they produce is given in Ref. [35]. Some of the diagnostics have specific importance to the pellet fueling experiments and are described in more detail in this section.

2.4.1 Far-infrared interferometer

The far-infrared (FIR) interferometer diagnostic on JET [36] is a multichannel interferometer used to measure the change of phase experienced by a coherent beam of radiation propagated through the plasma which is proportional to the line integral of electron density. The interferometer light source is a deuterated hydrocyanic acid (DCN) laser which operates at a wavelength of 195 μm. The light source is modulated at 100 kHz with a rotating cylindrical grating and split into six vertical chords and a vertical reference leg as shown in Fig. 2.8. The FIR interferometer has a measurable range from 10^{18} to $2 \times 10^{20}\,\mathrm{m}^{-3}$ and has time resolution of $\approx 10^{-4}$ s.

An inversion of the interferometer data using a generalization of the Abel inversion technique for the non-circular flux surface geometry is routinely done to give density profiles. It is assumed in the inversion that the electron density is a constant on the flux surfaces. This has been verified by comparison of the inverted interferometer electron density profiles with Thomson scattering data from the JET LIDAR diagnostic [37] which is capable of measurements every two seconds throughout the discharge. An example of a comparison of the two measurements is shown in Fig. 2.9. The two experimentally determined profiles generally show good agreement; however, the inverted profiles cannot reproduce fine structures in the density profile owing to the sparse number of interferometer chords. Typically the line integral of the density is measured to an accuracy of 1%, which after inversion gives an accuracy on the central density of $\sim 5\%$.

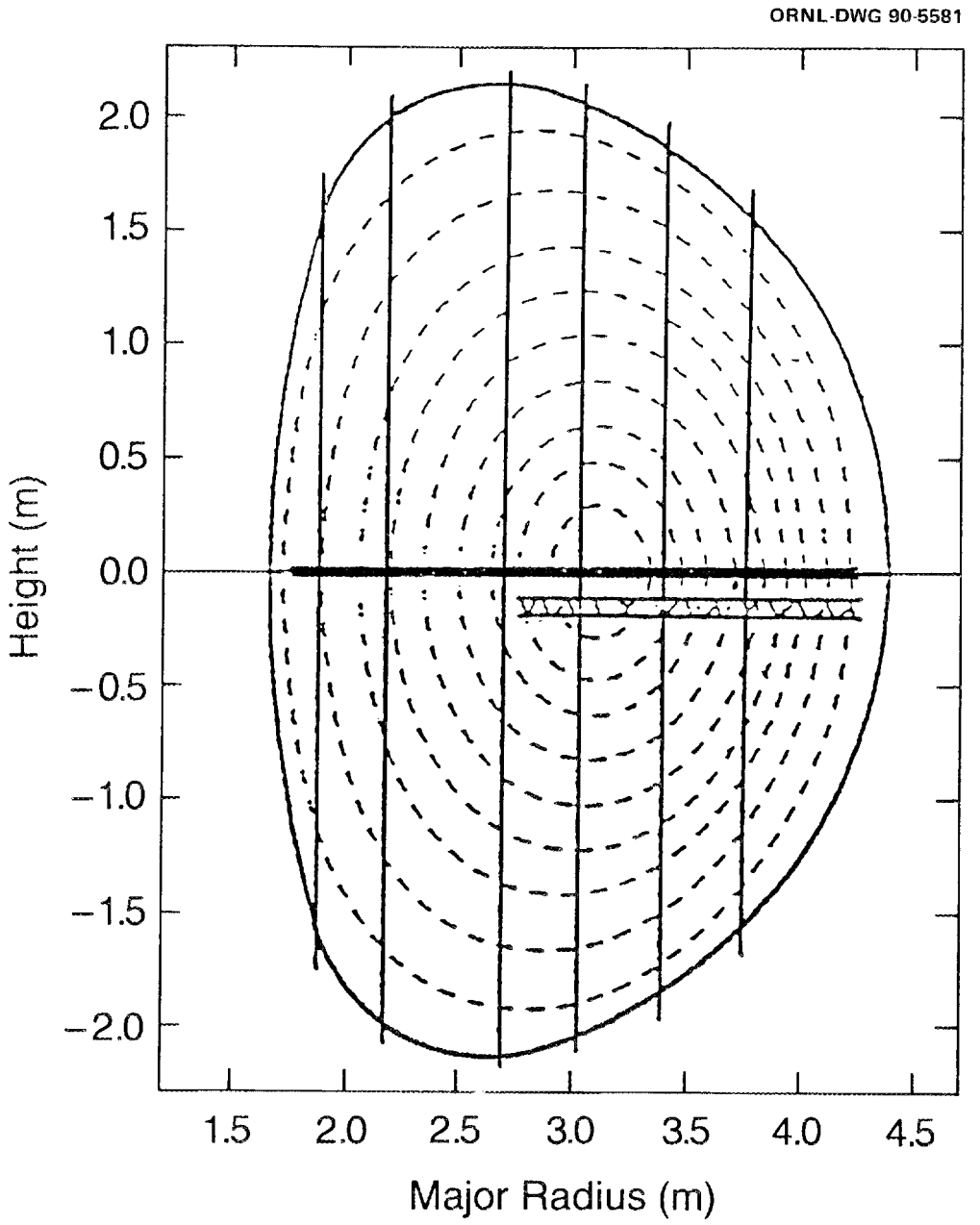

Fig. 2.8 Schematic showing lines of sight for three diagnostics in the JET poloidal cross section. The vertical lines are sightlines of the six interferometer channels, the thick line is the LIDAR sightline, and the hatched zone is the ECE sightline.

2.4.2 Electron cyclotron emission spectrometer

The primary method used for electron temperature measurement on JET is electron cyclotron emission (ECE). A radial profile of electron temperature is determined with data from a scanning Michelson interferometer system [38]. The second harmonic emission intensity is proportional to the electron temperature from the blackbody level relation $I(\omega) = \omega^2 T/8\pi^3 c^2$, and thus an inversion must be performed to obtain the local temperature. The inversion must use the magnetic field geometry determined from an equilibrium calculation to determine the radial position of emission and is therefore subject to error. The absolute accuracy is estimated to be within $\pm 10\%$, and relative accuracy between spatial points is within $\pm 5\%$.

2.4.3 Soft X-ray detector arrays

A set of soft X-ray detector arrays has been installed on JET and is primarily intended for fluctuation and instability studies. The single vertical and three horizontal arrays are located on the same octant of JET as the pellet injection system as shown in Fig. 2.2. This fortuitous location makes it possible to view the ablation of the pellet with 200 kHz fast digitization windows around the pellet events. Figure 2.10 shows typical soft X-ray data from an injected 4 mm pellet. The penetration of the pellet can be determined from the contour plot of the data as shown in the figure. The major radius at which the signal ends along the line of trajectory is the furthest point of pellet penetration. The soft X-ray diagnostic is also useful in determining light impurity behavior. Since high-Z contributions to the soft X-ray radiation are small, the radiation is primarily due to carbon and oxygen bremsstrahlung.

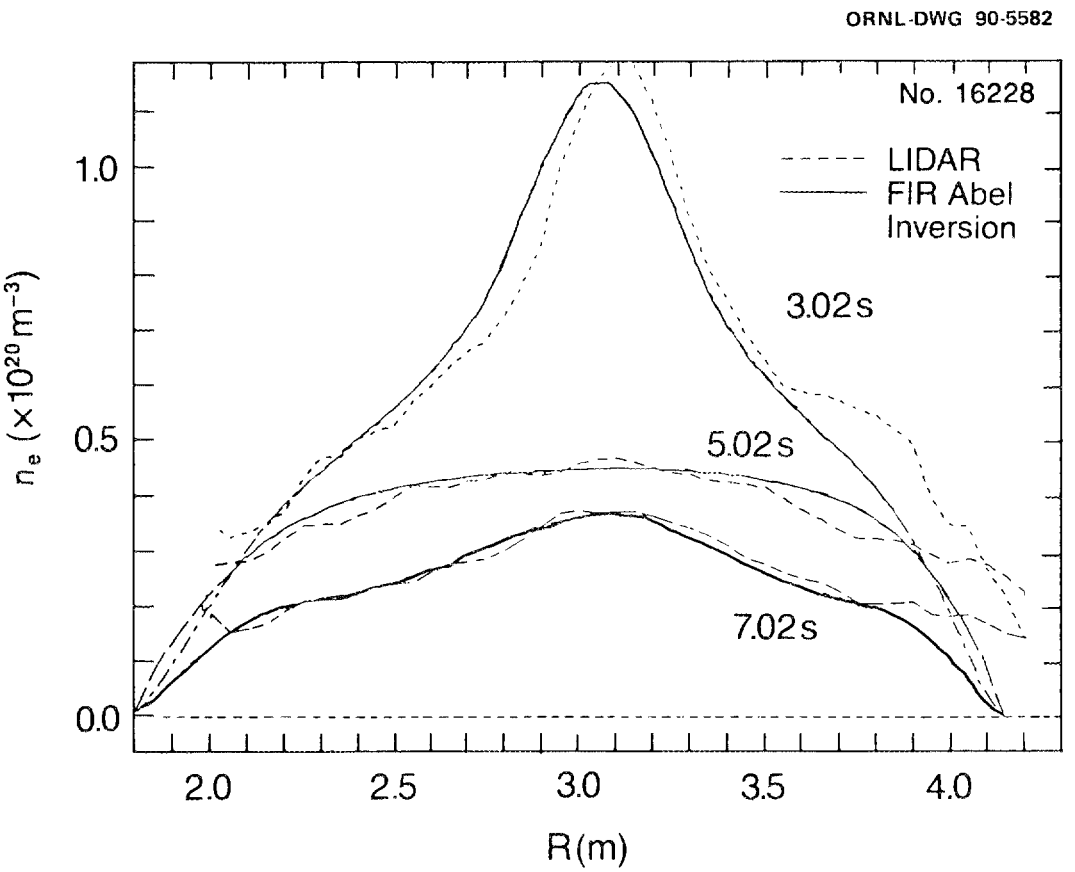

Fig. 2.9 Comparison of LIDAR measured electron density profile with the inverted profile from the FIR interferometer data.

ORNL-DWG 90-5583

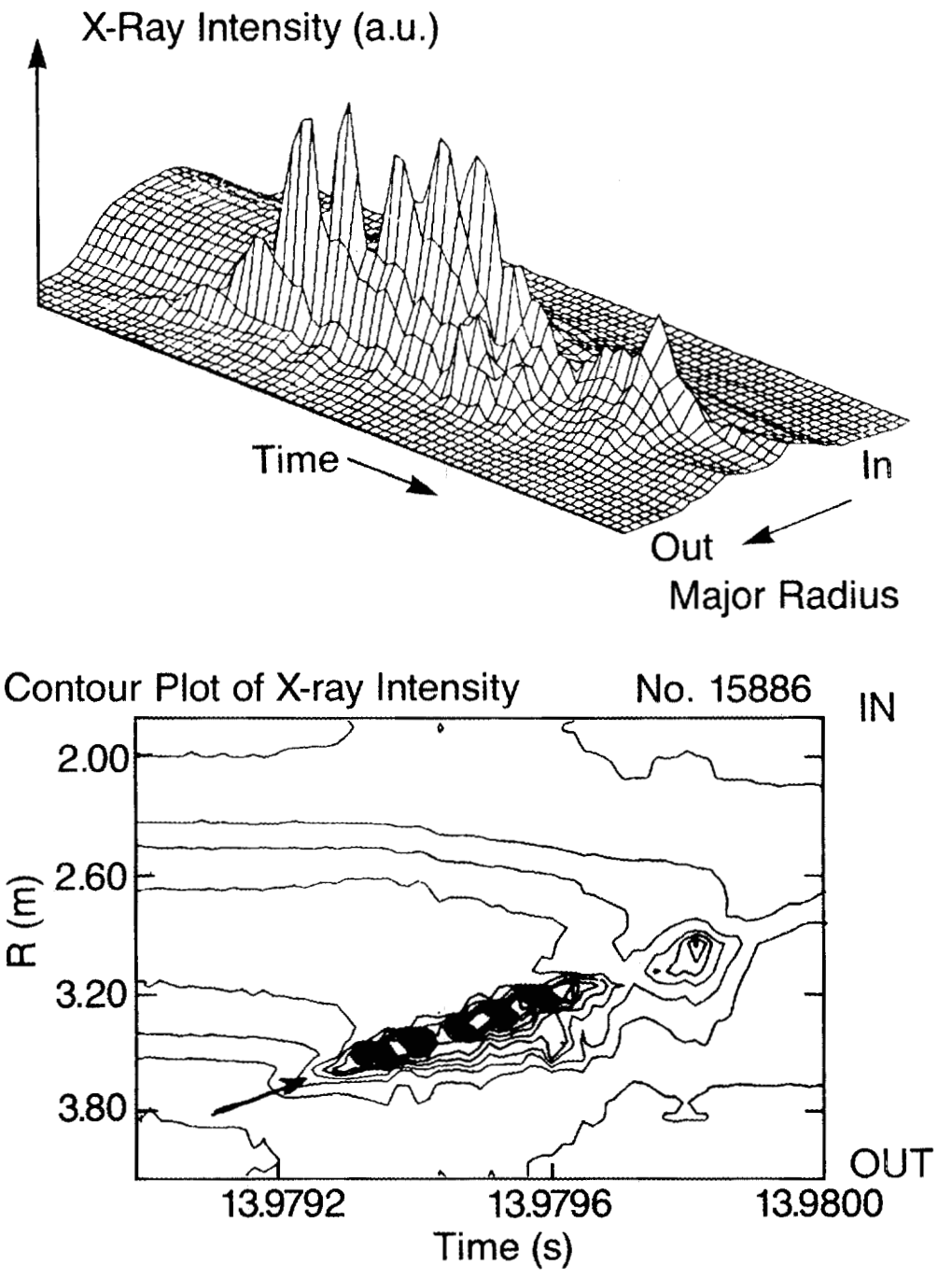

Fig. 2.10 Contour and 3-dimensional plots of pellet ablation as seen by the vertical soft X-ray camera. X-ray intensity is plotted versus time and major radius.

2.4.4 D_α and visible bremsstrahlung detection

Detection of D_α light and visible bremsstrahlung emission from the plasma is accomplished with a number of discrete detectors and a poloidal array of detectors. The total bremsstrahlung emissivity given from the plasma with electron temperature T_e (eV), electron and ion densities n_e, n_i (m^{-3}), and ion charge Z_i is given by [39]

$$E_{\text{brem}} = \frac{C_b}{\lambda} \frac{n_e n_i Z_i^2 g_{\text{ff}}\, e^{-hc/\lambda T_e}}{T_e^{1/2}} \qquad (\text{photons/s/m}^3/\text{Å/s} - \text{r}), \tag{2.2}$$

where C_b is $9.5 \times 10^{-20}/4\pi$, and g_{ff} is the free-free Gaunt factor. The Gaunt factor used in the integrated analysis of JET data [40] is

$$g_{\text{ff}} = 1.456\left(\frac{2.368}{T_e}\right)^{-0.149}. \tag{2.3}$$

The expression then used to derive Z_{eff}, the effective ionic charge of the plasma, is

$$Z_{\text{eff}} = \frac{4\pi\lambda E_{\text{brem}}}{9.5 \times 10^{-35}} \left(\int_{-Zv}^{Zv} n_e^2\, g_{\text{ff}} T_e^{-1/2} dZ\right)^{-1}. \tag{2.4}$$

Determinations of Z_{eff} are made using this expression for both a vertically and a horizontally measured chord of bremsstrahlung using the measured electron temperature and density profiles.

Hydrogenic particle fluxes from the wall and limiter are also determined from the D_α measurements by assuming that the emitting shell in the plasma extends into 0.9 of the minor radius. The fluxes are then given by

$$\Phi_w = 2\pi B_w A_w F \qquad (\text{particles/s})$$

$$\Phi_L = 4\pi B_L A_L F \qquad (\text{particles/s}), \tag{2.5}$$

where A_w is the wall surface area calculated with an effective minor radius of $\sim 0.9\langle a\rangle$, A_L is the surface area of the belt limiters, B_w and B_L are the brightness in photons/s $\cdot$ m^2 $\cdot$ s $-$ r as measured from the D_α array from the wall and limiter, respectively, and F is the ratio of total number of ionizations to the number of photons emitted from $3 \rightarrow 2$ transitions taken from the Johnson-Hinnov factor [39] with corrections for molecular dissociation.

The particle confinement time as defined by Eq. (1.1) is calculated from the particle fluxes by the expression [40]

$$\tau_p = \frac{N_e}{\Phi_L + \Phi_W + \Phi_i + \Phi_{NB} - dN_e/dt}, \tag{2.6}$$

where N_e is the total number of electrons, Φ_{NB} is the flux from neutral beam injection, and Φ_i is the impurity flux. The impurity flux is assumed to be equal to the product of the concentration of a given impurity in the plasma and the hydrogenic particle flux from the wall and limiter and can be written as

$$\Phi_j = Z_j f_j \left(\Phi_L + \Phi_W - dN_e/dt\right), \tag{2.7}$$

where f_j is the concentration of the jth impurity. The relative impurity concentrations f_j are taken from an average of spectroscopic measurements over a large number of discharges.

CHAPTER 3

EXPERIMENTAL OBSERVATIONS

In this chapter we describe several general experimental observations made from several of the measurements taken during the multi-pellet fueling experiments. The large number of pellet injection events and generally high-quality data have made possible a comparison of several observations for a variety of conditions. We concentrate on observations of relevance to pellet fueling and particle deposition and transport.

3.1 Pellet Penetration and Deposition

One of the important parameters measured in these experiments is the penetration of the pellets into the plasma. We define penetration as the distance into the plasma that the pellet reaches when all of the pellet mass has been ablated away and deposited into the plasma. The pellet penetration was measured by the duration of the D_α light signal and also from soft X-ray measurements as described in Sect. 2.4. Neither measurement was available for every pellet injection event, but in the cases where both measurements were available, good agreement was obtained. Figure 3.1 is a plot of the soft X-ray determined penetration versus the D_α determined penetration. The data lie on a straight line within the experimental errors.

The measured pellet penetration has been compared with the theoretically predicted penetration using the neutral and plasma shielding (NPS) ablation model [24] and was found to agree well in most cases. Figure 3.2 is a plot of the measured penetration versus the predicted penetration for 2.7 mm and 4 mm

ORNL-DWG 89-3038 FED

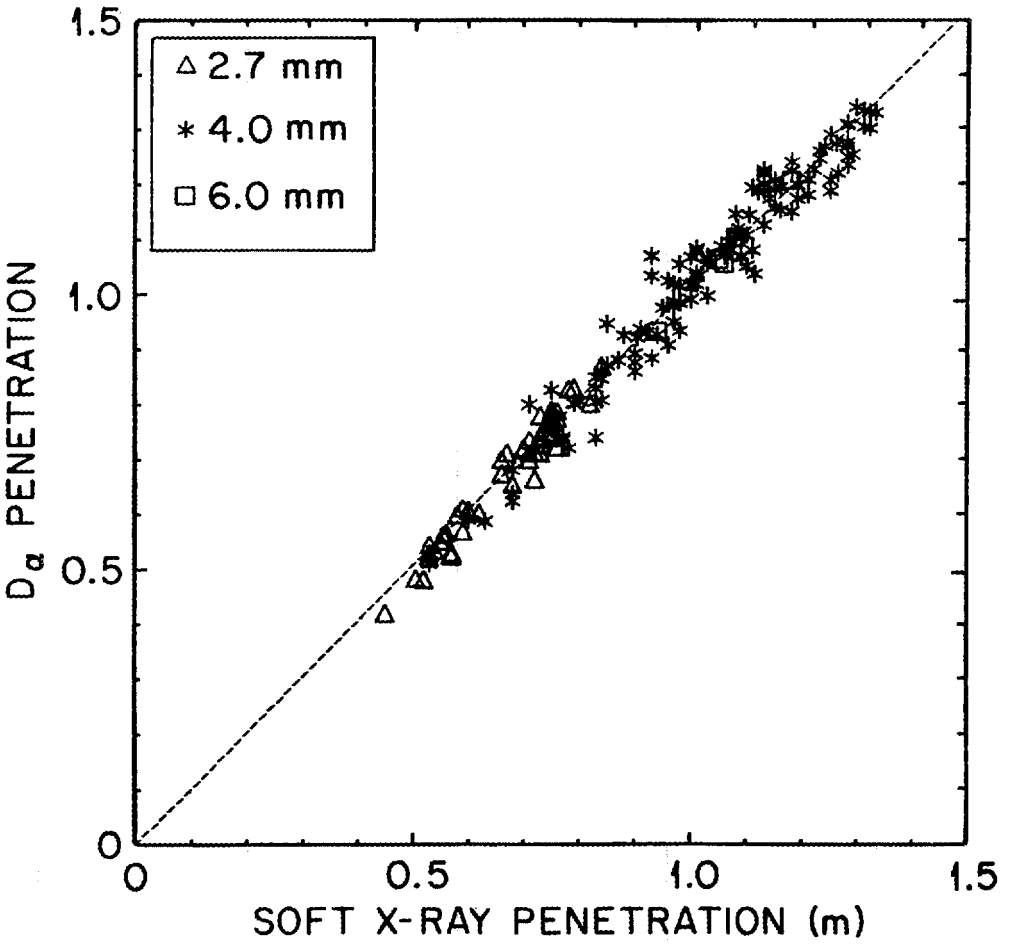

Fig. 3.1 Comparison of pellet penetration determination from soft X-ray measurement and D_α measurement.

ORNL-DWG 89-3037 FED

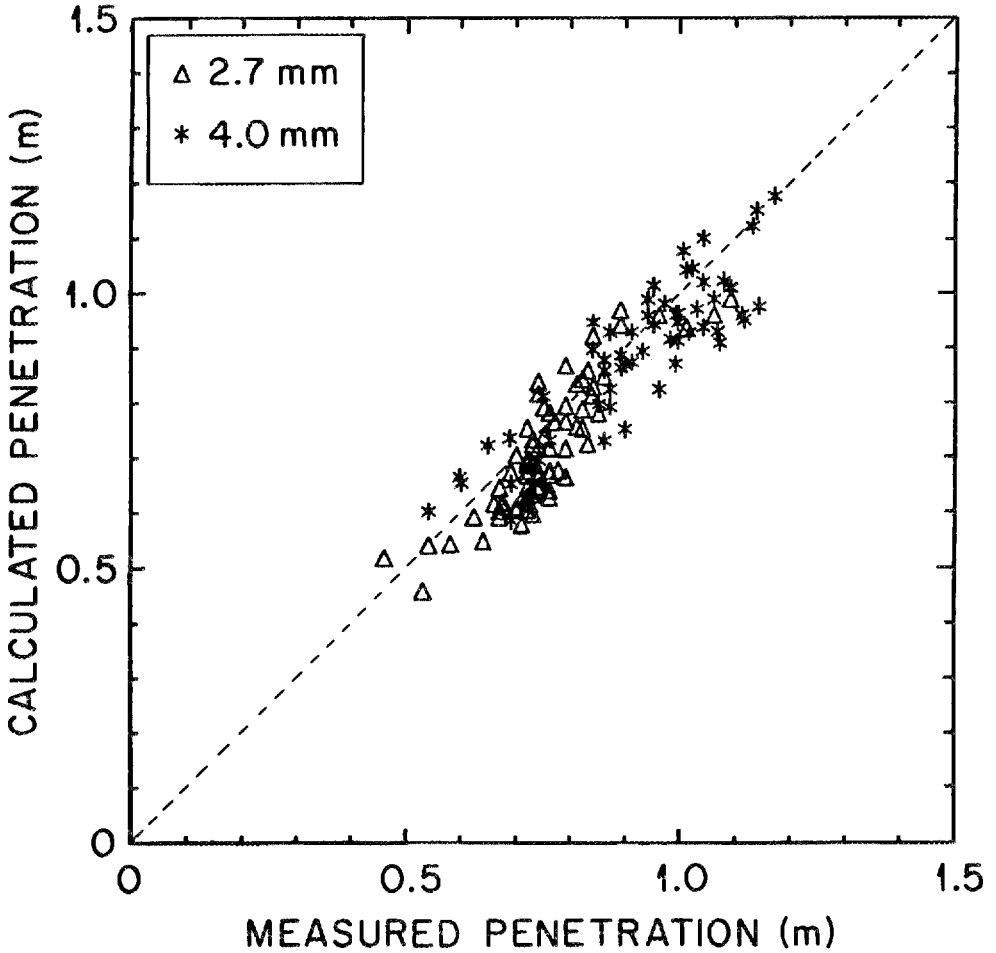

Fig. 3.2 Pellet penetration calculation by the neutral and plasma shielding model compared with measured penetration. All of the pellets analyzed were injected with velocities near 1300 m/s.

pellets in both ohmic and auxiliary heated plasmas and shows generally good agreement. The penetration calculation uses electron temperature profiles generated from second harmonic ECE data and electron density profiles determined from the FIR interferometer chordal data. The pellet mass is compensated for in the calculation by using the measurement from the microwave bridge pellet mass diagnostic to determine the equivalent spherical radius for the pellet. A free parameter exists in the ablation model, namely, the neutral cloud radius surrounding the ablating pellet. This radius was fixed in the calculation to 1.0 mm, which was found to give good agreement with earlier ablation modeling [25]. Although the calculated penetration in these cases agrees with the measurement, the calculated ablation rate does not agree as well with D_α measurements. Strong striations are seen in the ablation light emission, as can be seen in Fig. 2.8, which may be due to hydrodynamic instabilities or rational magnetic flux surfaces in the plasma. The pellet velocity dependence predicted by the NPS model is negligible and was tested by injecting pellets at velocities of 500 m/s and 1400 m/s into similar ohmic plasma conditions. The results of this experiment, shown in Fig. 3.3, indicate that the slower pellet penetration is consistently overpredicted by the model. This indicates a deficiency in the NPS model that needs to be rectified for accurate prediction of higher speed pellet penetration. The neutral shielding ablation model [21] used to derive Eq. (1.4) does not provide enough shielding from the plasma electrons and consistently underestimates the pellet penetration.

The particle deposition from the ablating pellet has been determined for a number of pellet injection events and in general agrees reasonably well with ablation calculations of the particle source. The deposition is determined by the LIDAR Thomson scattering diagnostic, which was triggered 20 ms after the

ORNL-DWG 89M-2998 FED

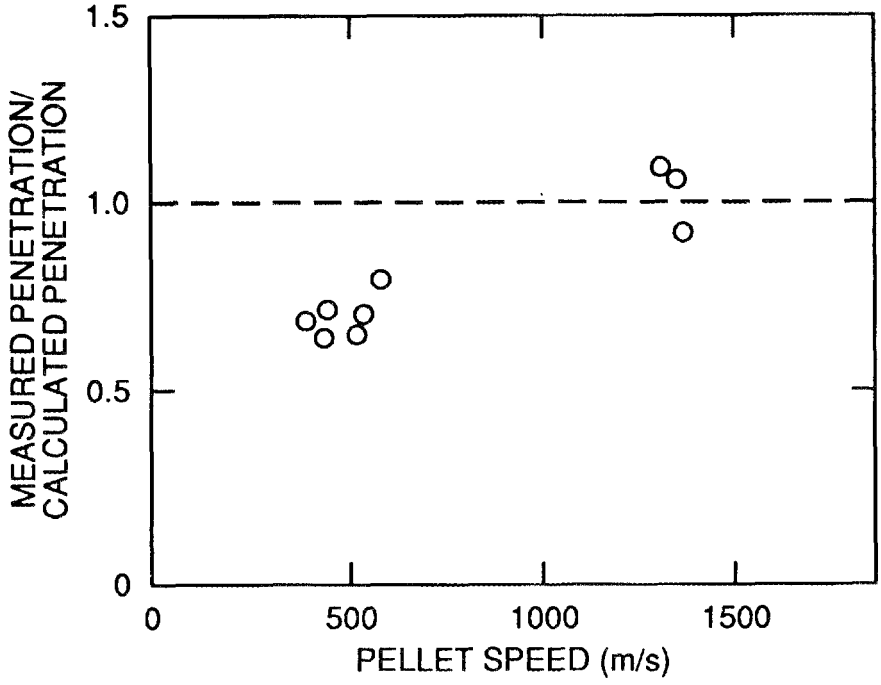

Fig. 3.3 The ratio of measured to calculated pellet penetration as a function of pellet speed. The measured pellet mass and speed as well as plasma parameters are used in the calculation. The slower pellets' penetration is consistently overestimated by the NPS model [24].

pellet was injected. The electron density profile before the pellet injection event was taken from the inversion of the 6-channel FIR interferometer data. The difference of the density profiles at these two times gives a reasonable measurement of the particle deposition from the ablating pellet. An interesting difference in pellet depositions has been found to exist in cases where pellets reach near or beyond the magnetic axis between discharges that have a $q = 1$ rational magnetic surface (as determined by sawtoothing in soft X-ray signals) and discharges without a $q = 1$ surface. The pellet D_α emission and particle deposition near the $q = 1$ surface are greatly reduced from the case with no $q = 1$ surface, as shown in Fig. 3.4. This reduced emission seems to indicate that there is strong mixing of the cold ablated pellet mass near the $q = 1$ surface that reduces the pellet ablation and hence the particle deposition. Measurements of D_α emission from the ablating pellet typically show a strong reduction in emission as the pellet crosses the $q = 1$ surface; however, no similar strong reduction is seen at other rational surfaces. Fluctuations in the D_α emission are seen during the pellet ablation, as can be seen in Fig. 3.4. These fluctuations are similar to those seen in previous pellet injection experiments [10, 19] and are thought to be due to instabilities related to plasma shielding of the ablating pellet.

Another observation of the pellets that are injected beyond the $q = 1$ surface is a measured drop in the soft X-ray emission in vertical soft X-ray channels looking within the $q = 1$ surface. An example of this observation is shown in Fig. 3.5 for a 6 mm pellet injected in an ohmic discharge. This drop in soft X-ray emission occurs before the pellet reaches inside the $q = 1$ surface, possibly indicating a rapid collapse in electron temperature within the $q = 1$ surface on a time scale of $\sim 10\,\mu$s. Such a temperature perturbation will affect the pellet by reducing the ablation rate as it continues traveling within the $q = 1$ surface.

ORNL-DWG 89M-2997 FED

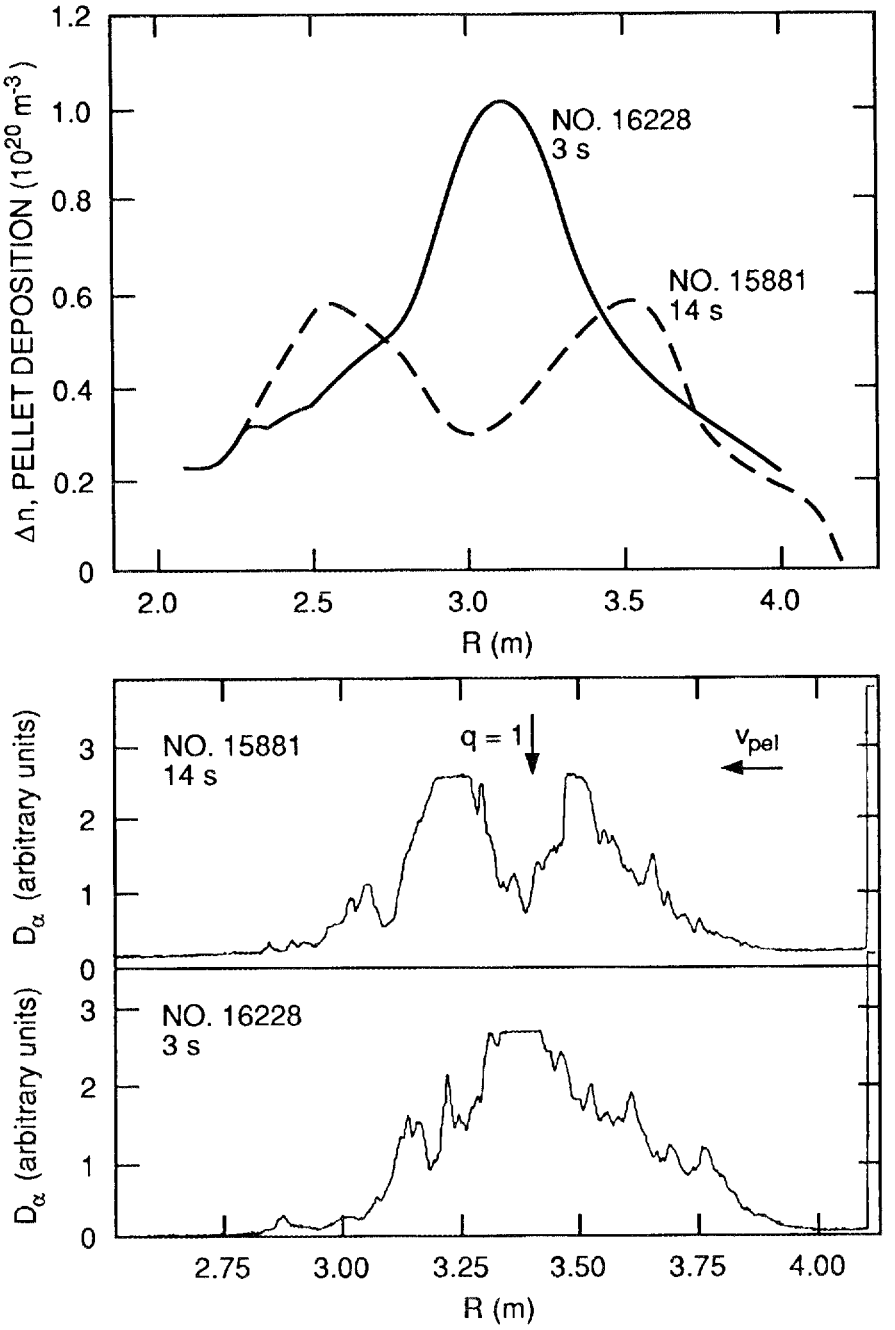

Fig. 3.4 Pellet particle deposition and D_α emission for pellets with penetration to 2.85 m. The discharge with the $q = 1$ surface as determined by soft X-ray inversion radius shows a large drop in D_α emission, which affects the central particle deposition.

ORNL-DWG 89-2994 FED

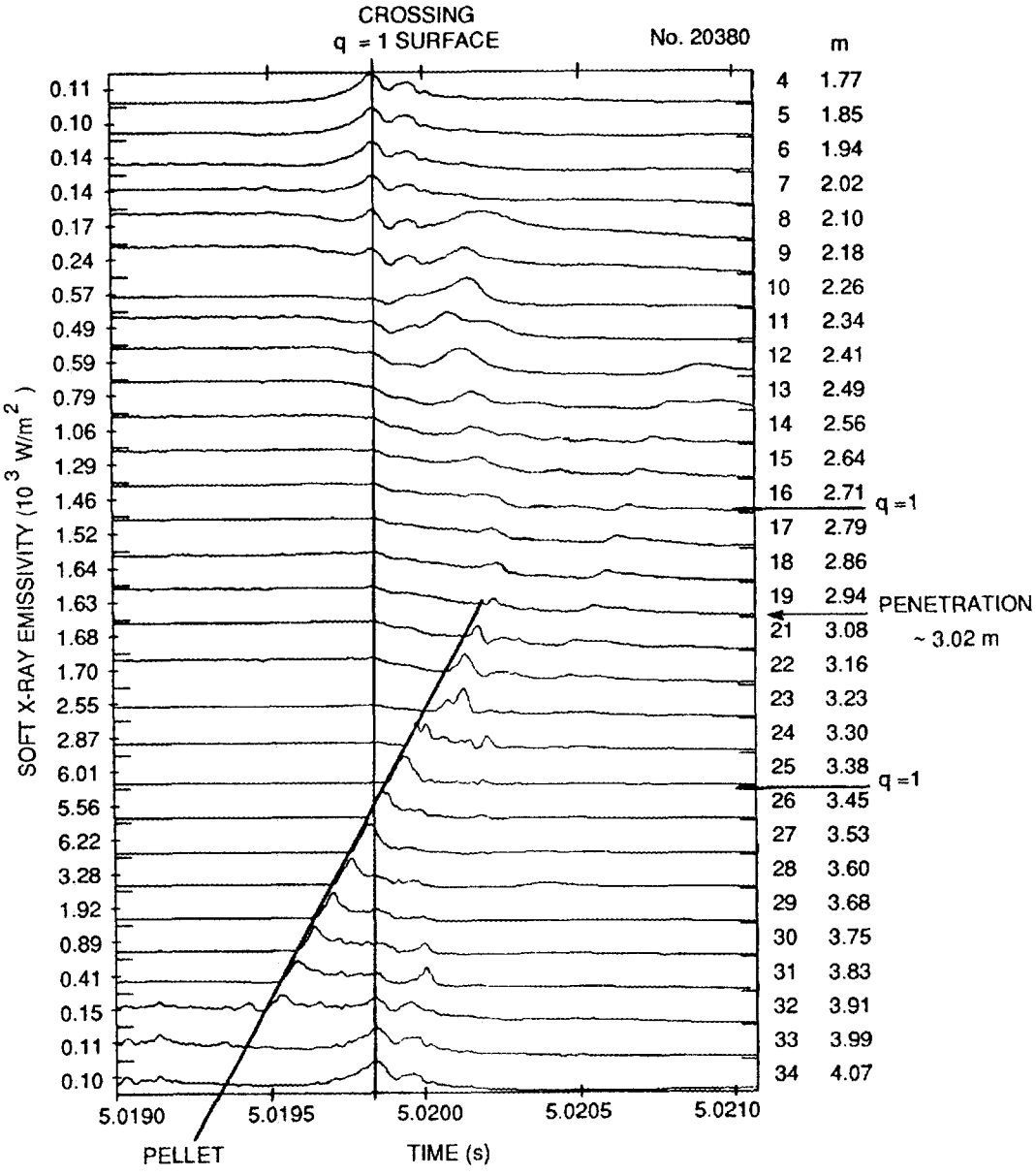

Fig. 3.5 Vertical soft X-ray channel emission during a 6 mm pellet injection event. Each channel's signal is autoscaled for maximum resolution. The pellet is seen to penetrate to ~ 3.02 m by the diagonal line. The approximate time the pellet crosses the $q = 1$ surface is marked with the vertical line.

3.2 Pellet Fueling Efficiency

The pellet fueling efficiency is defined as the ratio of the number of pellet deuterium atoms that are deposited in the plasma and the number of deuterium atoms originally in the pellet. It is a measure of the percentage of pellet particles that are deposited in the plasma. The mass of each pellet is measured as it is injected into the plasma by the microwave cavity system described in Sect. 2.3. The number of electrons in the plasma, N_e, is determined by Simpson integration of the line integral densities and multiplication by the plasma volume [40]:

$$N_e = 2\pi R_0 \mathrm{A_p} \frac{\int n_e(x)\Omega(x)dx}{\int \Omega(x)dx}, \tag{3.1}$$

where $\Omega(x)$ is the area Jacobian and $\mathrm{A_p}$ is the cross sectional area. The incremental number of electrons has been determined for a large number of pellets and the associated pellet fueling efficiency determined. Figure 3.6 shows the pellet fueling efficiency plotted as a function of pellet penetration for a variety of pellet sizes and plasma conditions. From this plot we can see that pellets injected in ohmically heated plasmas show a very high fueling efficiency ($>$ 75 % and in some cases virtually 100 %) independent of pellet penetration. However, pellets that are injected during neutral beam heating and ICRF heating show an expected drop in penetration due to the higher temperatures and also show a reduced fueling efficiency of below 60 %. This means that more of the pellet is being eroded in the plasma edge and scrape-off layer and pumped away before being deposited in the plasma. Some of the additional ablation at the plasma edge is possibly due to energetic ions and electrons from the neutral beam and ICRF heating. The implications of this result for fueling a high-temperature fusion reactor plasma are that pellet sizes will have to take into account the fueling efficiency to adequately fuel a reactor plasma. A reactor may also need to be able to

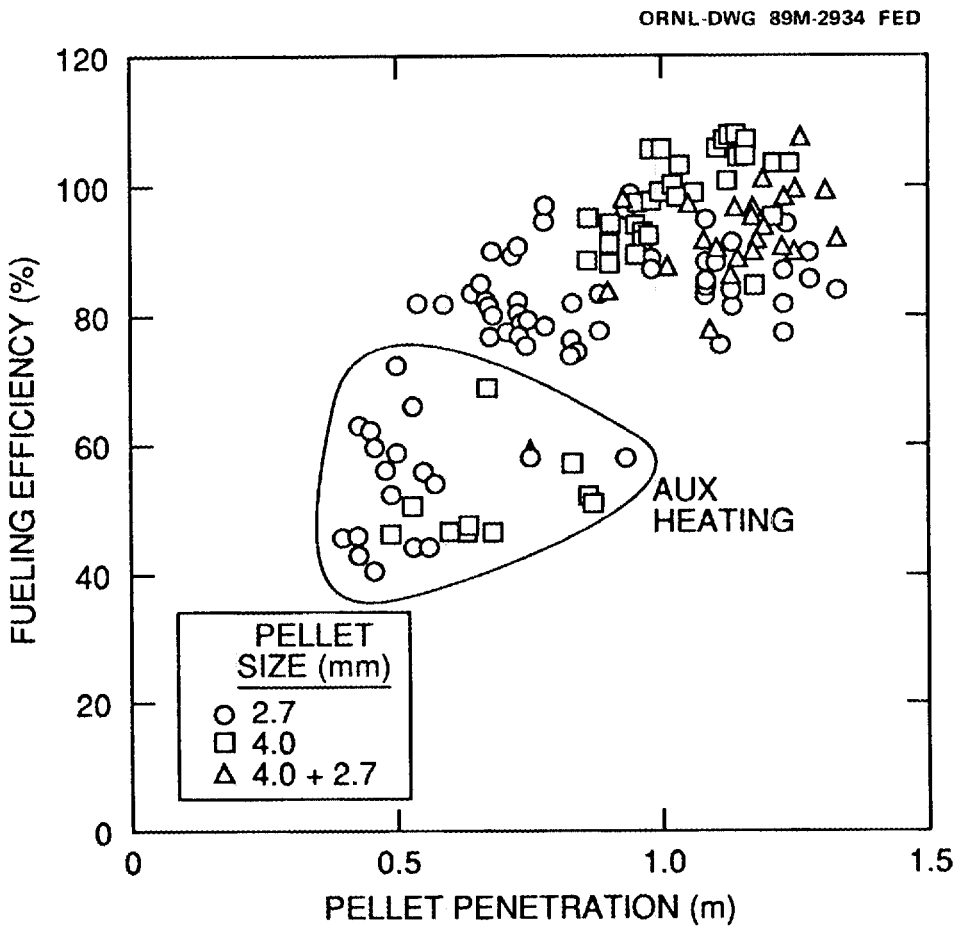

Fig. 3.6 Fueling efficiency as a function of pellet penetration. The data points within the circled region were injected during auxiliary heating.

pump a moderate fraction of the pellet particles that are not confined in the plasma volume.

3.3 Electron Density Profile Evolution

A temporal evolution of the electron density profile is obtained by inversion of the FIR interferometer data as described in Sect. 2.4.1. The electron density profile has been found to change dramatically in pellet fueled plasmas with deep pellet penetration. An example of the density profile evolution for an ohmic plasma with two pellets is shown in Fig. 3.7.

The penetration depth of the pellet has a dramatic effect on the peaking of the density profile, as one would intuitively expect. The central to volume average ratio $[n_e(0)/\langle n_e \rangle]$ 200 ms after pellet injection normalized to the pre-pellet value is found to have a strong dependence on pellet penetration. Figure 3.8 shows that penetration of the pellet to within 20 cm of the axis is required to achieve a significant increase in the density peaking. In cases when there is partial pellet penetration it takes more than 100 ms for the maximum density peakedness to occur as the density perturbation diffuses into the core of the plasma. In experiments where pellets were injected into plasmas that already had peaked density profiles from previous pellets, no significant increase in peaking was observed despite penetration of the pellets to the magnetic axis. The limit in central to average ratio of ~ 3.5 was found in these multiple pellet fueled cases.

It is possible for the small 2.7 mm pellets to penetrate to the axis if they are injected early in the discharge when the electron temperature is still relatively low. In discharges where a number of 2.7 mm pellets were injected into the current rise, the electron density was found to peak dramatically and continue to stay peaked following the injection of subsequent pellets. In these cases, the temperature is

ORNL-DWG 89-2996 FED

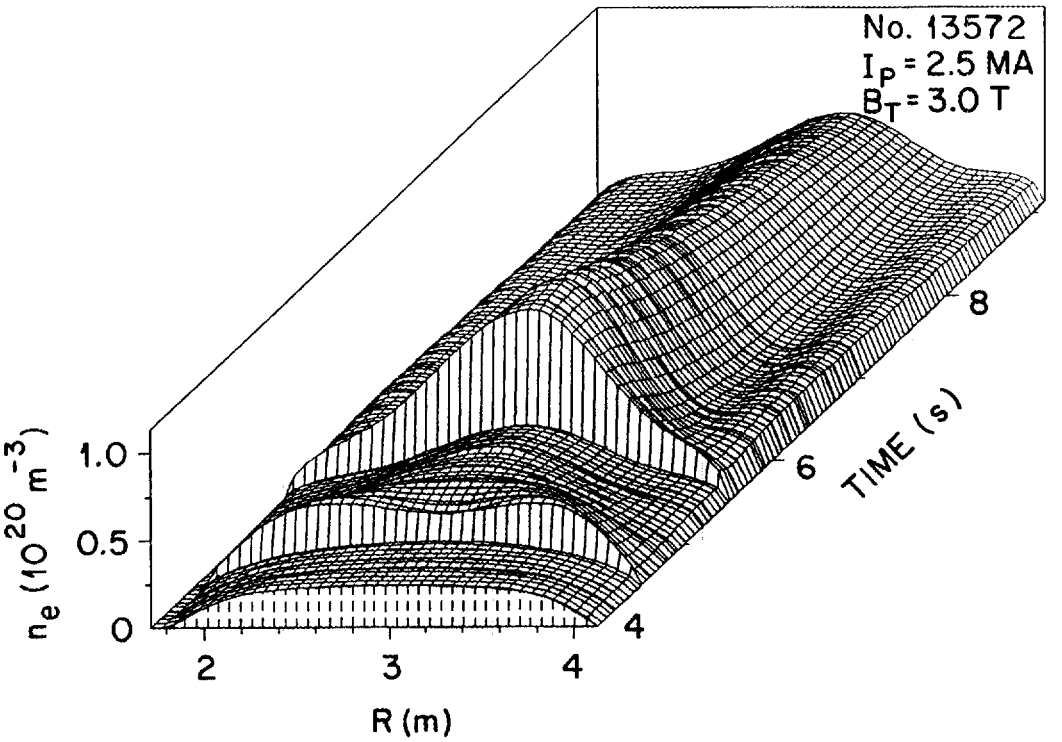

Fig. 3.7 Electron density evolution in a pellet fueled discharge. A 4 mm pellet is injected at 4.5 s and both a 4 mm and a 2.7 mm pellet are injected at 5.5 s. The first pellet penetrates to 3.4 m, while the second 4 mm pellet penetrates to 3.1 m.

ORNL-DWG 89M-2935 FED

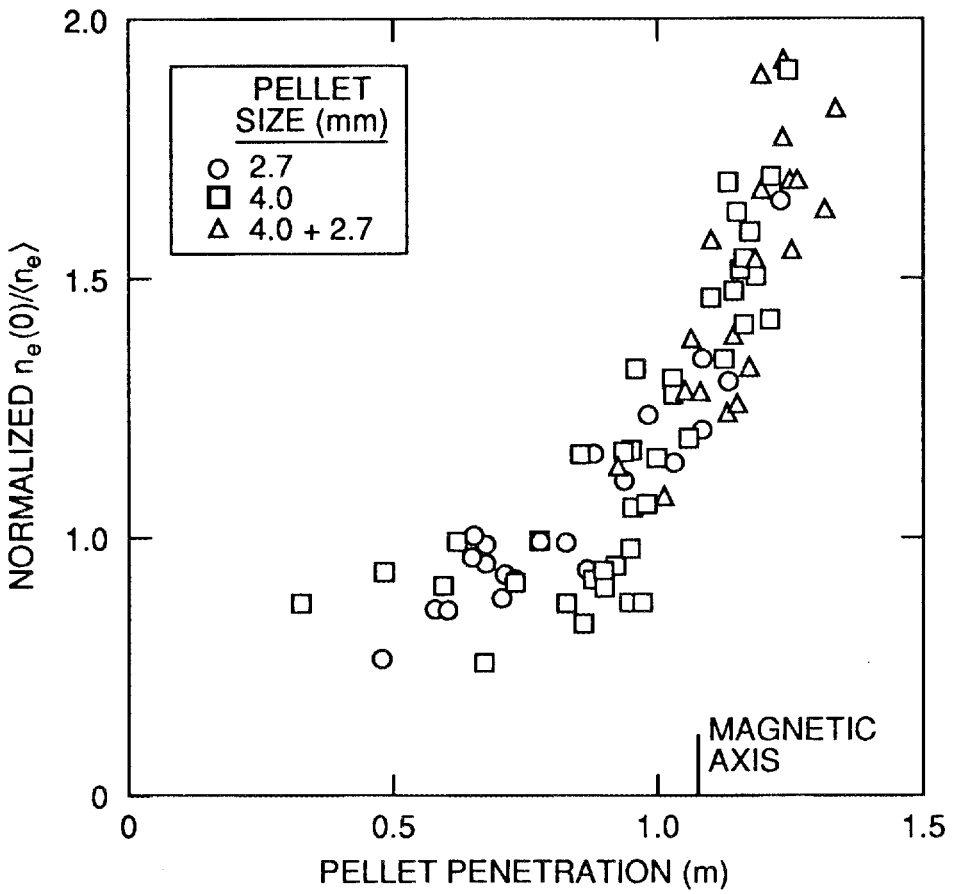

Fig. 3.8 Electron density peaking factor as a function of pellet penetration 200 ms after injection. Normalized peaking factor is $n_e(0)/\langle n_e \rangle$ at 200 ms divided by $n_e(0)/\langle n_e \rangle$ before injection.

maintained fairly low (~1–2 keV), and the subsequent pellets all penetrate to the axis or beyond. Figure 3.9 shows an example of the electron density evolution for a multi-pellet fueled case compared to a gas-puff only fueled case. It can be seen that the peaked density profile persists for over 2 s after the last pellet and ends as auxiliary heating is applied.

In discharges that lead to a peaked density profile from pellet fueling, a pedestal in the density profile is seen to form on the outer half of the minor radius, as is shown in Figs. 3.7 and 3.9. This pedestal, which is seen in both the FIR profile inversion and the LIDAR measured density profile, forms soon after pellet injection and remains in auxiliary heated discharges with peaked density profiles as shown in Fig. 3.10. This pedestal may be related to the q profile as shown in Fig. 3.10, where the $q = 2$ rational surface (as determined by equilibrium calculation) is in the region where the pedestal forms. One possible explanation for this local flattening of the density profile is the formation of magnetic islands at the $q = 2$ surface, which leads to enhanced diffusion of particles.

In discharges with peaked density profiles from pellet injection that persist until the onset of sawteeth oscillations [$q(0)$ reaches 1], the density profile is observed to undergo a reduction in the peakedness in the center of the discharge within the sawtooth inversion radius and remain less peaked through the remaining sawteeth. It is hypothesized that the initial sawtooth crash expels particles from the plasma core and that there is not sufficient inward convection of particles in the plasma core to repeak the discharge before the next sawtooth crash, which typically occurs in 100 ms.

3.4 Heating of Pellet Fueled Plasmas

One of the principal goals of the multi-pellet fueling experiments on JET was to determine the effect of high-power auxiliary heating of pellet fueled plasmas.

ORNL-DWG 89-2933 FED

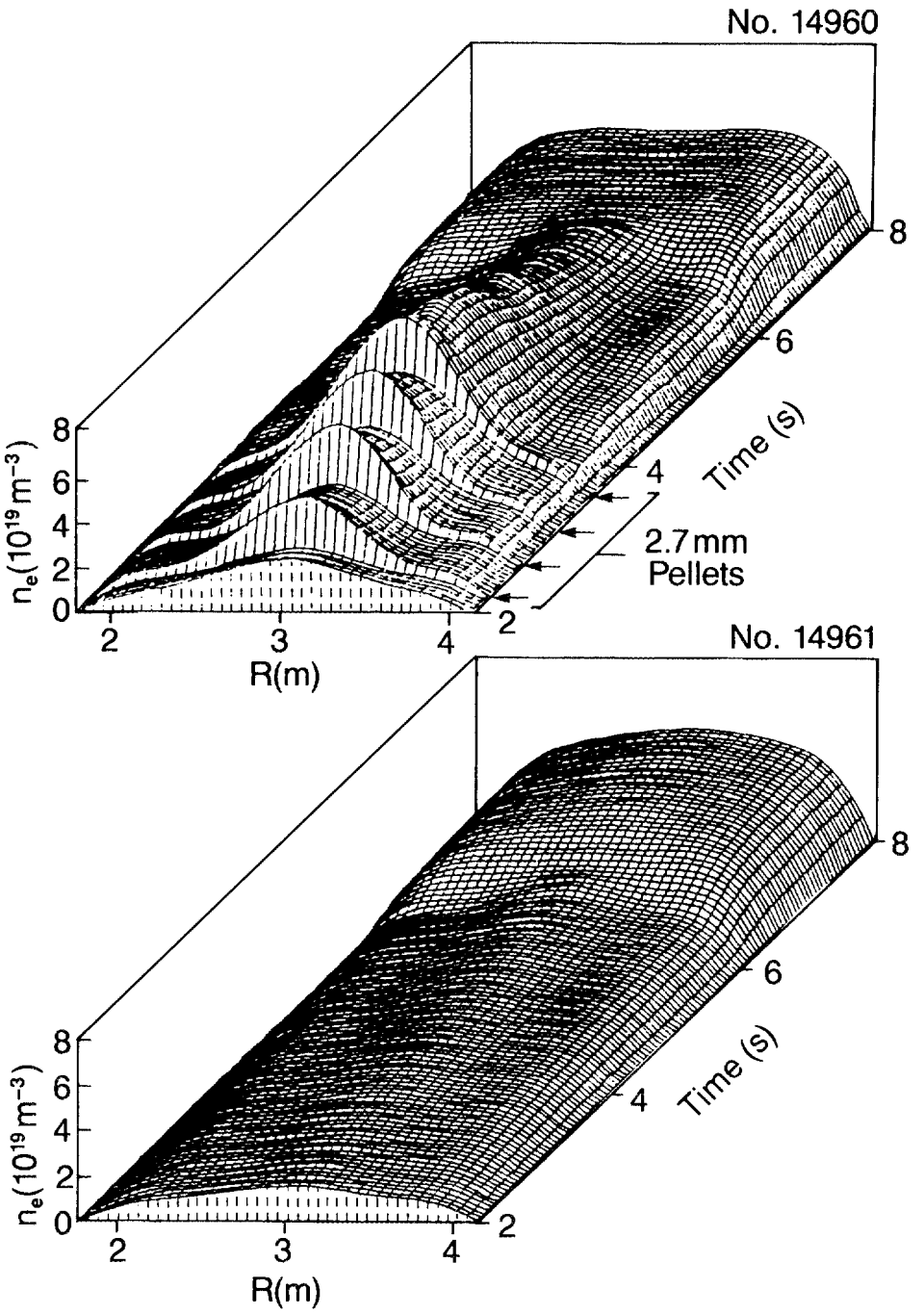

Fig. 3.9 Electron density evolution of a multi-pellet fueled 4 MA discharge (14960) and a similar gas fueled discharge (14961). Auxiliary heating power of 5 MW ICRF and 5 MW NBI is applied at 6 s.

ORNL-DWG 90-5584

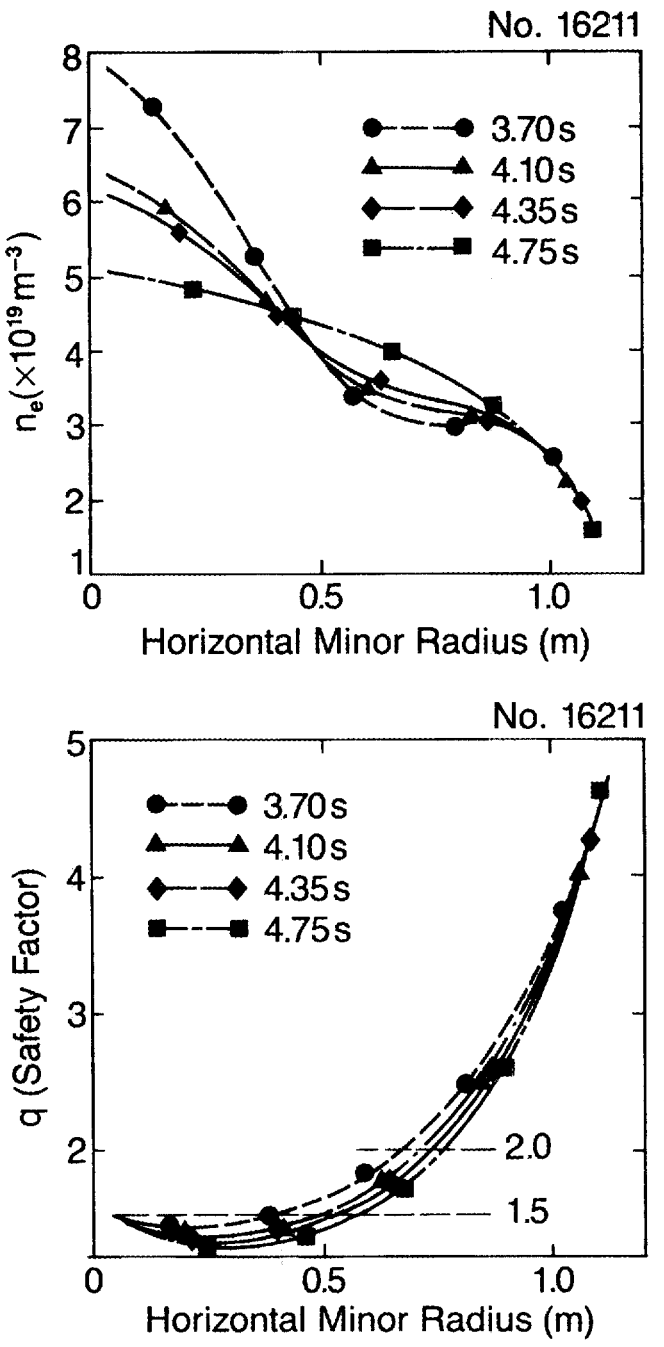

Fig. 3.10 Electron density profile and q profile (from TRANSP) in an ICRF heated pellet fueled discharge. The pedestal in the density profile is in the region of $q = 2$ and q on axis is near 1.5 at the time of the temperature collapse (4.4 s).

The very high ICRF and NBI power available on JET was used to heat pellet fueled plasmas with peaked density profiles and reduced impurity concentrations. Experiments were carried out to determine the parameters under which the highest fusion yield in deuterium plasmas could be obtained.

The optimization of plasma heating performance is aimed at maximizing Q_{DT}, the ratio of total fusion power production to total input heating power for a deuterium-tritium plasma:

$$Q_{DT} \equiv \frac{P_{DT}}{P_{in}} \propto \frac{\int dV n_D n_T \langle \sigma v \rangle Y}{\int dV nT/\tau_E} \propto n_i(0) T_i(0) \tau_E \,, \tag{3.2}$$

where P_{DT} is the thermal fusion power production of a deuterium-tritium plasma, P_{in} is the externally applied heating power, $\langle \sigma v \rangle$ is the reaction rate coefficient averaged over a Maxwellian ion distribution at temperature $T_i(0)$, τ_E is the energy confinement time, and Y is the 17.6 MeV energy yield per reaction, which consists of a 14.1 MeV neutron and a 3.5 MeV alpha particle. Clearly, to maximize Q_{DT}, the central ion density, central ion temperature, and energy confinement time must be maximized.

The pellet fueling experiments on JET have attempted to optimize the heating profile by using central ICRF heating on dense peaked profile plasmas. The results been improvements in $n_i(0)T_i(0)\tau_E$ over the non-pellet case up to a value of 2×10^{20} $\mathrm{keV \cdot m^{-3} \cdot s}$ [41], which extrapolates to an equivalent Q_{DT} of ~ 0.1. ICRF heating has been applied at power levels up to 16 MW in combination with NBI and has produced D-D reaction rates in excess of $1 \times 10^{16}\,\mathrm{s}^{-1}$. The temporal evolution of the key plasma parameters in a heating experiment are shown in Fig. 3.11. Two types of heated discharge have been observed in these heating experiments. One type, as shown in Fig. 3.11, maintains a peaked density profile over 1.5 s into

ORNL-DWG 89-2995 FED

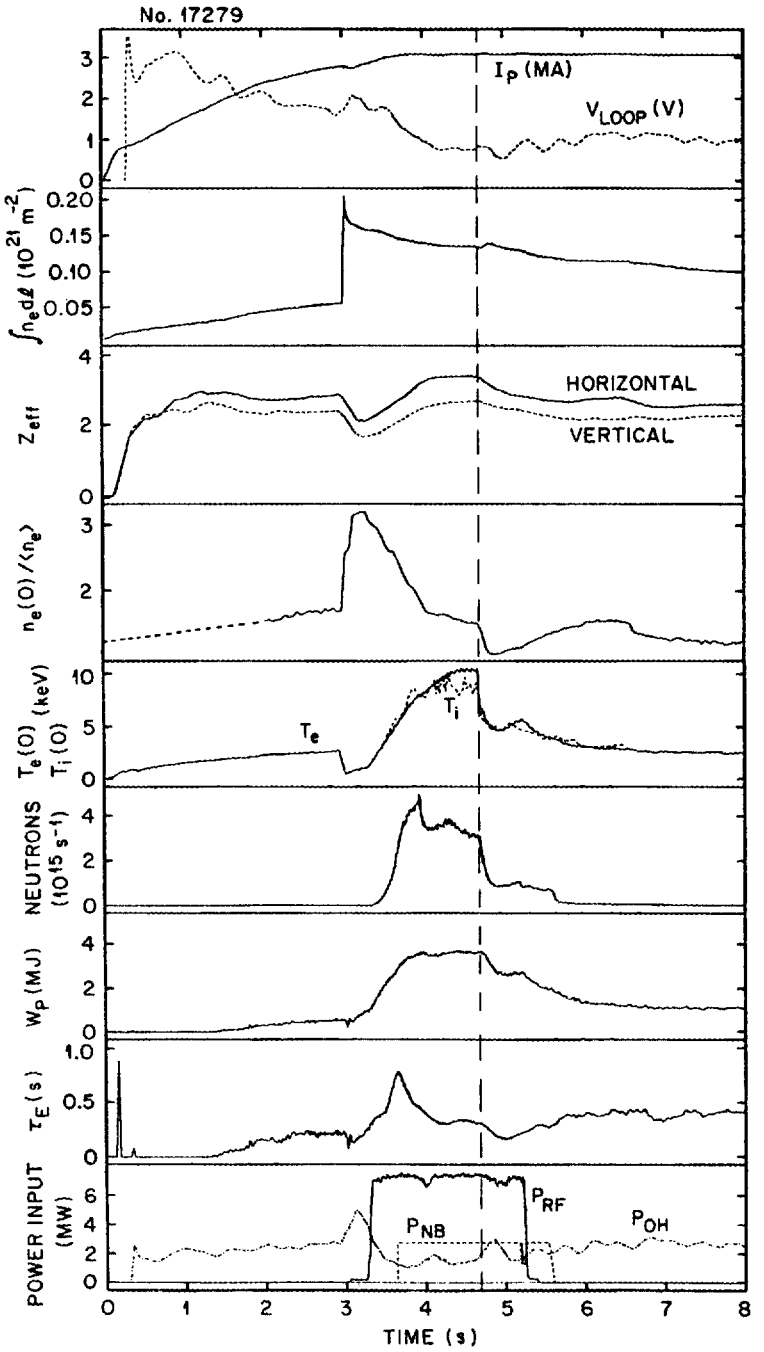

Fig. 3.11 Temporal evolution of plasma parameters with ICRF and NBI heating after pellet injection. A 4 mm and a 2.7 mm pellet were injected at 3 s. A collapse in central temperature and density is observed at 4.7 s.

the heating pulse. The peaked density profile and high temperatures are then abruptly terminated when an internal collapse of the temperature and density is observed (at 4.7 s in Fig. 3.11). The other type of heated discharge shows a rapid decay of the electron density, does not reach as high a central temperature, and has no abrupt collapse of central temperature and density. The mechanisms behind these two types of heated discharge are not yet fully understood.

A distinctive characteristic of the two types of heated peaked density profile shots is the MHD activity that is measured during the heating pulse by the array of magnetic loops used to measure magnetic activity in JET [39]. A common characteristic of the discharges that show a rapid decay of the central density is a small but measurable increase in the signal of the $n = 1$ and higher n mode $\tilde{B}_\theta$ coils. An example of this signal is shown in Fig. 3.12, where the $n = 1$ and $n = 3$ $\tilde{B}_\theta$ signals show an increase during the time the density profile becomes very flat. The amplitude of the $\tilde{B}_\theta$ signals shows good correlation with the increase in central electron temperature and not with the magnitude of input power. This characteristic MHD activity is seen in discharges both with and without NBI heating. In cases where the peaked profiles persist longer in both auxiliary heated and ohmic discharges, the MHD signals remain very low and do not show an increase until the collapse in temperature and density occurs in the high power ICRF heated cases. In Fig. 3.13, we show the $\tilde{B}_\theta$ ($n = 1$) signals overlaid for four discharges with similar pellet deposition from a 4 mm pellet injected at 3 s. The discharges that show rapid density decay (No. 16235 with 10 MW ICRF and 6.5 MW NBI heating, and No. 16228 with 10 MW ICRF heating) have a larger MHD signal than either the ICRF heated discharge (No. 16211 with 8 MW ICRF) or the ohmic discharge (No. 16226), which both retained a peaked central density (until the collapse in No. 16211 and until sawtooth oscillations begin in

ORNL-DWG 90-5585

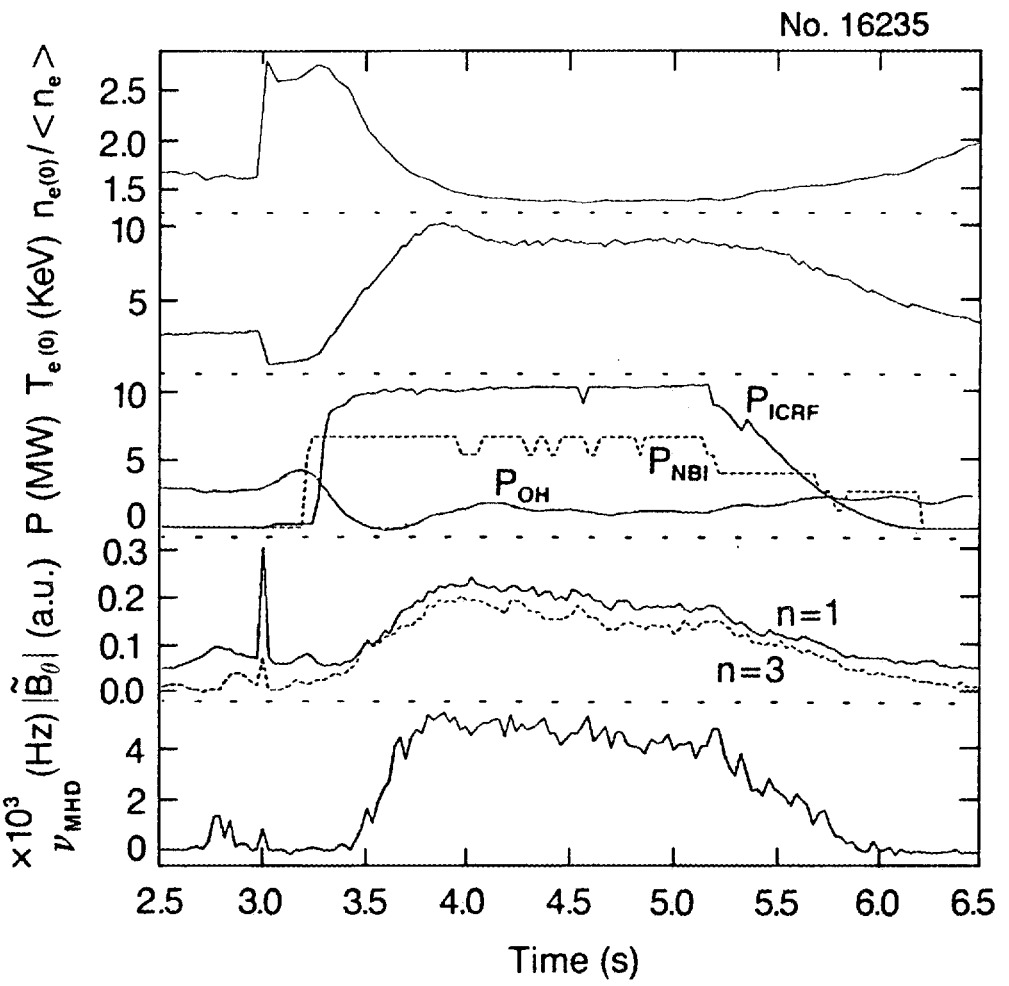

Fig. 3.12 Plasma parameters and MHD activity of a pellet fueled discharge with ICRF and NBI heating. A 4 mm pellet was injected at 3 s. The magnitude and frequency of $|\tilde{B}_\theta|$ are shown for $n = 1$ and $n = 3$.

ORNL-DWG 90-5586

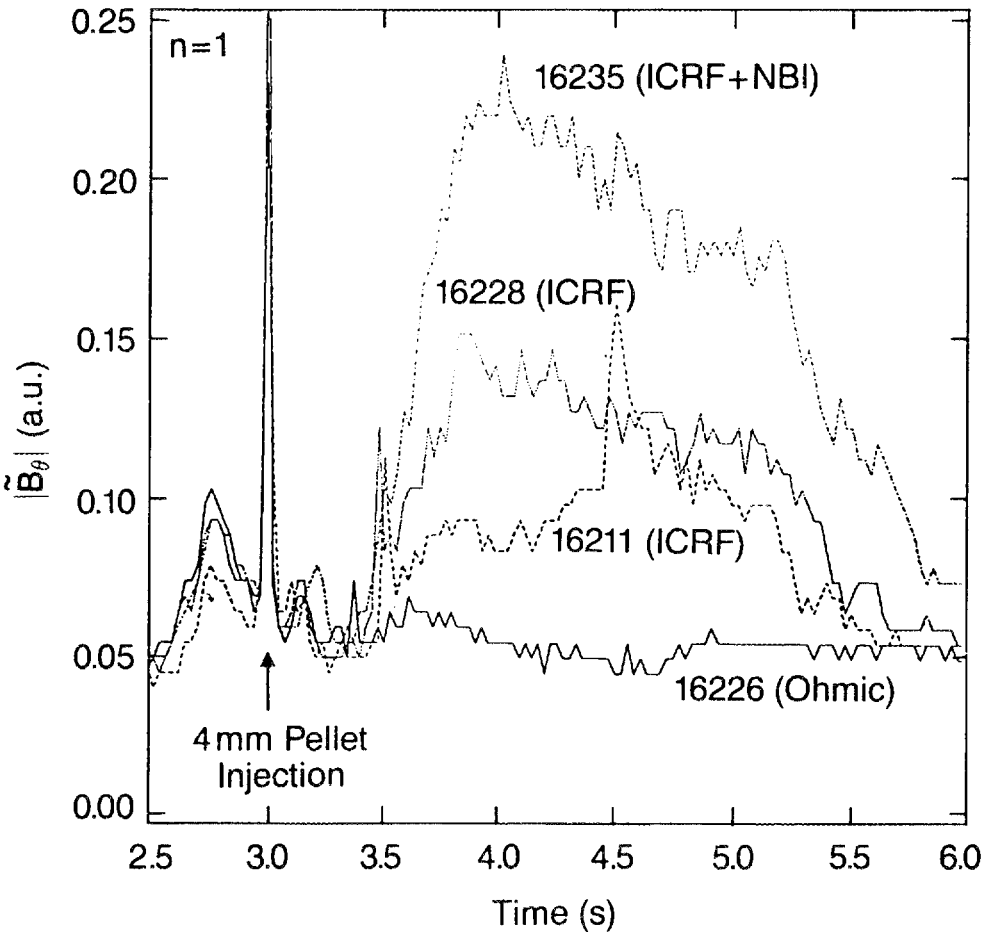

Fig. 3.13 The poloidal magnetic field fluctuation level $|\tilde{B}_\theta|$ for $n = 1$ in four 3 MA discharges after 4 mm pellet injection. Both discharges No. 16235 and No. 16228 show strong decay of central density. Discharge No. 16211 shows rapid flattening of the density profile at the collapse at 4.5 s and discharge No. 16226 with no auxiliary heating shows weak central density decay.

No. 16226). It is interesting to note that internal disruptions (sawteeth) are detected by this external magnetic loop measurement and typically have a signal 2–3 times larger than the signal from the rapidly decaying discharges or the collapse in the ICRF heated cases (as in No. 16211). If this $\tilde{B}_\theta$ signal is representative of an internal disturbance, then it would be expected to have a less dramatic effect on transport in the plasma core than sawteeth. It should be pointed out that these collapses seen in the high power ICRF heated discharges are not sawteeth (q is > 1 on axis), but rather show a characteristic $m = 3, n = 2$ behavior and are thought to be caused by a ballooning mode (either ideal or infernal) instability.

3.5 Energy and Particle Confinement

The effect of particle fueling on global plasma confinement is an issue that has been carefully studied in past experiments and is of particular interest in the current tokamak devices with parameters reaching reactor relevant levels. Determination of the energy confinement, τ_E, is made from the diamagnetic measurement of total stored energy and the total input power by the relation

$$\tau_E \equiv \frac{W_p}{P - dW_p/dt}. \tag{3.3}$$

In the ICRF heated peaked density profile discharges described in the previous section, the energy confinement is seen to be improved over similar non-pellet fueled discharges. This improvement is due to the central power deposition and improved confinement and lasts up to the period of the temperature collapse. The energy confinement can be seen in Fig. 3.11 to decrease after the collapse at 4.7 s.

The diamagnetic stored energy as a function of the denominator in Eq. (3.3) is shown in Fig. 3.14 for similar pellet and non-pellet fueled discharges. An

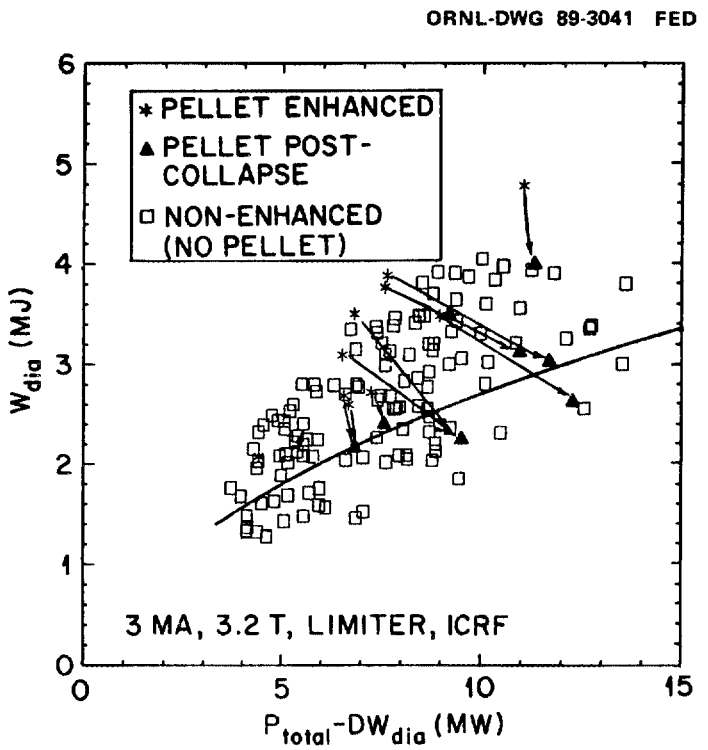

Fig. 3.14 Plasma stored energy as a function of input power for 3 MA, 3.2 T limiter discharges with ICRF heating. The discharges with enhanced central temperature before and after collapse are identified. The solid line represents Goldston [42] scaling for these nominal plasma conditions.

improvement in global confinement is seen for a few of the pellet discharges with peaked density profile. Most of the discharges show better confinement than the empirical scaling law used to describe a number of tokamak experiments [42]. The confinement after the collapse is seen to be significantly worse and can be as bad as in the worst non-pellet fueled discharges.

The particle confinement in JET is determined as part of the integrated analysis of the D_α visible bremsstrahlung data as described in Sect. 2.4.4. The particle confinement time as defined by Eq. (2.6) is calculated and has been compared for pellet fueled and non-pellet fueled discharges. An example of this comparison for ohmically heated discharges with multiple 2.7 mm pellet injection with central penetration is shown in Fig. 3.15. We see from this comparison that immediately after pellet injection, τ_p shows a sharp increase, due to the increase in N_e, which decays back to the pre-pellet value within a confinement time. The edge particle flux shows an increase shortly after the pellet injection and thus tends to reduce any improvement in τ_p. The total number of electrons is increased in the pellet fueled case, but the limiter particle flux is also increased. The average particle confinement time $\langle\tau_p\rangle$ is increased by about 20% over the non-pellet fueled discharge for only a $\sim$ 10% increase in the total particle source. In auxiliary heated discharges, a substantial increase in the edge particle flux is seen during both NBI and ICRF heating, which tends to reflect a reduction in τ_p below 500 ms. The pellet fueled discharges with auxiliary heating show no substantial increase in τ_p, even in the heated peaked density profile discharges discussed in the previous section.

3.6 Impurity Effects

One of the important advantages that pellet fueling provides over gas puff fueling is the deposition of fuel particles into the plasma without the introduction

ORNL-DWG 89-3040 FED

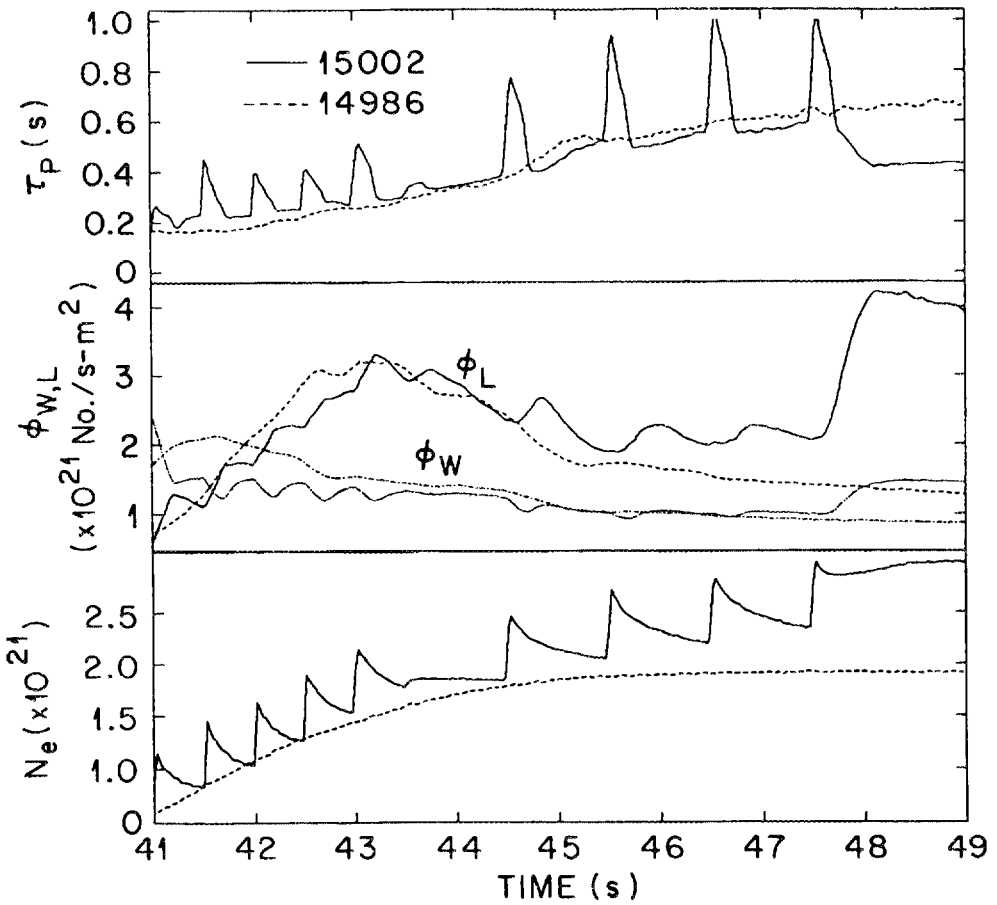

Fig. 3.15 Particle confinement comparison between pellet fueled and non-pellet fueled discharges. Both discharges are 3MA, 3.4T limiter configurations.

of any non-fuel impurity particles. This can be seen by observing the global impurity content of the plasma in the Z effective measurement which is defined as

$$Z_{\text{eff}} \equiv \frac{\Sigma n_{\text{i}} Z_{\text{i}}^2}{\Sigma n_{\text{i}} Z_{\text{i}}} \approx \frac{\Sigma n_{\text{i}} Z_{\text{i}}^2}{n_{\text{e}}}, \tag{3.4}$$

where the summations are over all species of charge Z_{i}. Z_{eff} is then the average ionic charge, weighted by a Z_{i} factor.

The measured global Z_{eff} from visible bremsstrahlung measurements shows a sudden decrease after pellet injection followed by a slow gradual rise back to the pre-pellet value as shown in the discharge in Fig. 3.11. In some of the pellet fueled JET discharges, determination of Z_{eff} profiles has been carried out using a poloidal array of visible bremsstrahlung detectors [43]. Immediately after pellet injection with central deposition, the central $Z_{\text{eff}}(0)$ can reach values less than 1.5 and the $Z_{\text{eff}}(r)$ profile is initially very hollow. As the electron density decays, the $Z_{\text{eff}}(r)$ profile has been seen to build up in the center to values of $\sim$ 3, showing an accumulation of impurities. After the density has decayed, the peaked $Z_{\text{eff}}(r)$ profile can be seen to return to the pre-pellet slightly hollow profile.

Despite the reduction of Z_{eff} seen immediately following pellet injection due to dilution effects, an accumulation of impurities has been seen in the core of the discharge when the electron density is peaked on axis. This accumulation can be seen from soft X-ray and bolometry measurements, which show an increase in central radiated power due to increased line radiation and bremsstrahlung. An example of this impurity accumulation is shown in Fig. 3.16 for the same discharge as is shown in Fig. 3.11, where the soft X-ray profiles in a 4 mm pellet fueled discharge with peaked central electron density are shown before the pellet injection and after the pellet injection when the density profile is peaked. By

ORNL-DWG 89-3039 FED

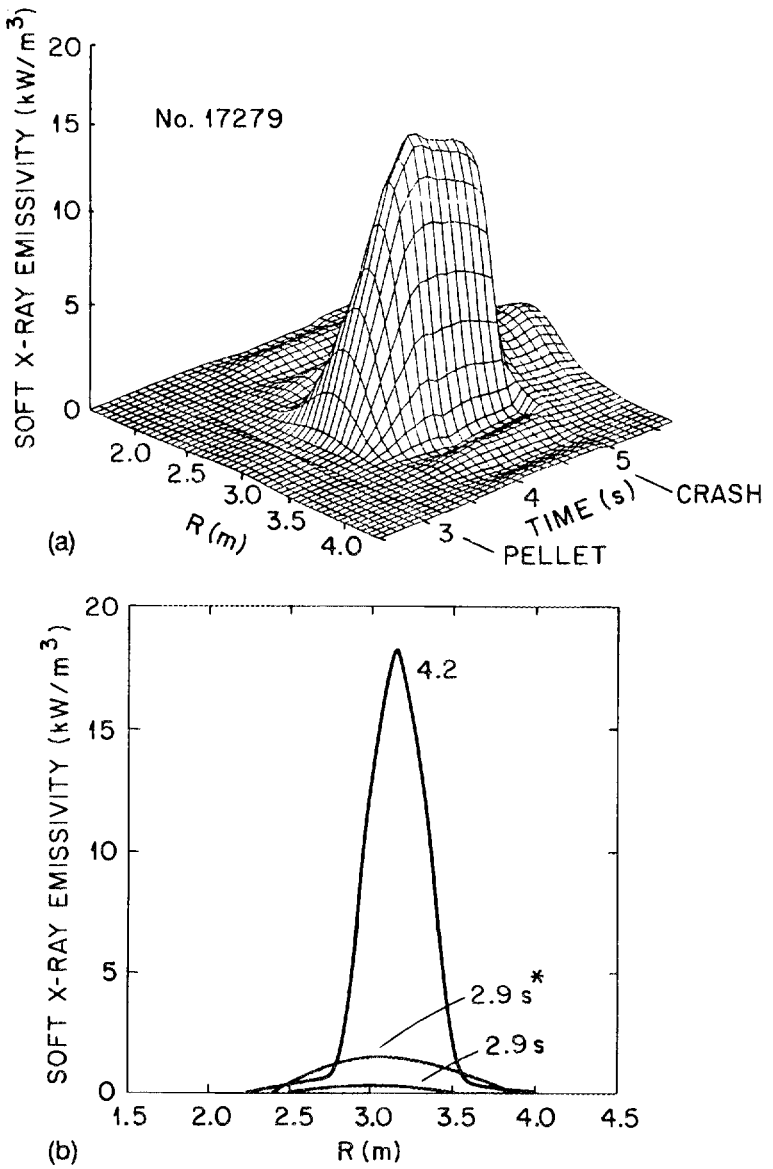

Fig. 3.16 Soft X-ray emissivity in a pellet fueled peaked density profile discharge. (a) Evolution of the tomographic inversion profiles. (b) Tomographic inversion profiles before and after pellet injection. *Pre-pellet profile scaled to $n_e^2 Z_{\mathrm{eff}}/T_e^{1/2}$ of the post-pellet time, showing strong impurity accumulation which ends at the collapse at 4.7 s.

scaling the pre-pellet soft X-ray profile to the electron density and temperature values [using the bremsstrahlung formula Eq. (2.2)] after pellet injection in Fig. 3.16b, we see that the post pellet profile is much more peaked and with $\sim$ 10 times the magnitude, indicating strong central accumulation of low-Z impurities.

Spectroscopic measurements from a VUV spectrometer [39] show radiation from high-Z impurities such as nickel, with much stronger line intensities in the innermost shells, which are predominantly due to centrally located ions where the temperature is highest. An example of the spectroscopic data is shown in Fig. 3.17, where the temporal evolution of intensity from Ni XXV and Ni XVIII line radiation is plotted with the electron density and soft X-ray intensity. The peak in Ni XXV radiation is seen when the central soft X-ray signal is at its maximum and the electron density profile is peaked on axis. The amount of power radiated from this impurity accumulation can reach as much as $45\,\mathrm{kW/m^3}$ but is usually not significant enough to cause a problem with the power balance and lead to a radiative collapse. This accumulation does, however, mask the high value of the fusion product that would otherwise be achieved in ICRF heated peaked density profile discharges if the impurities were not there.

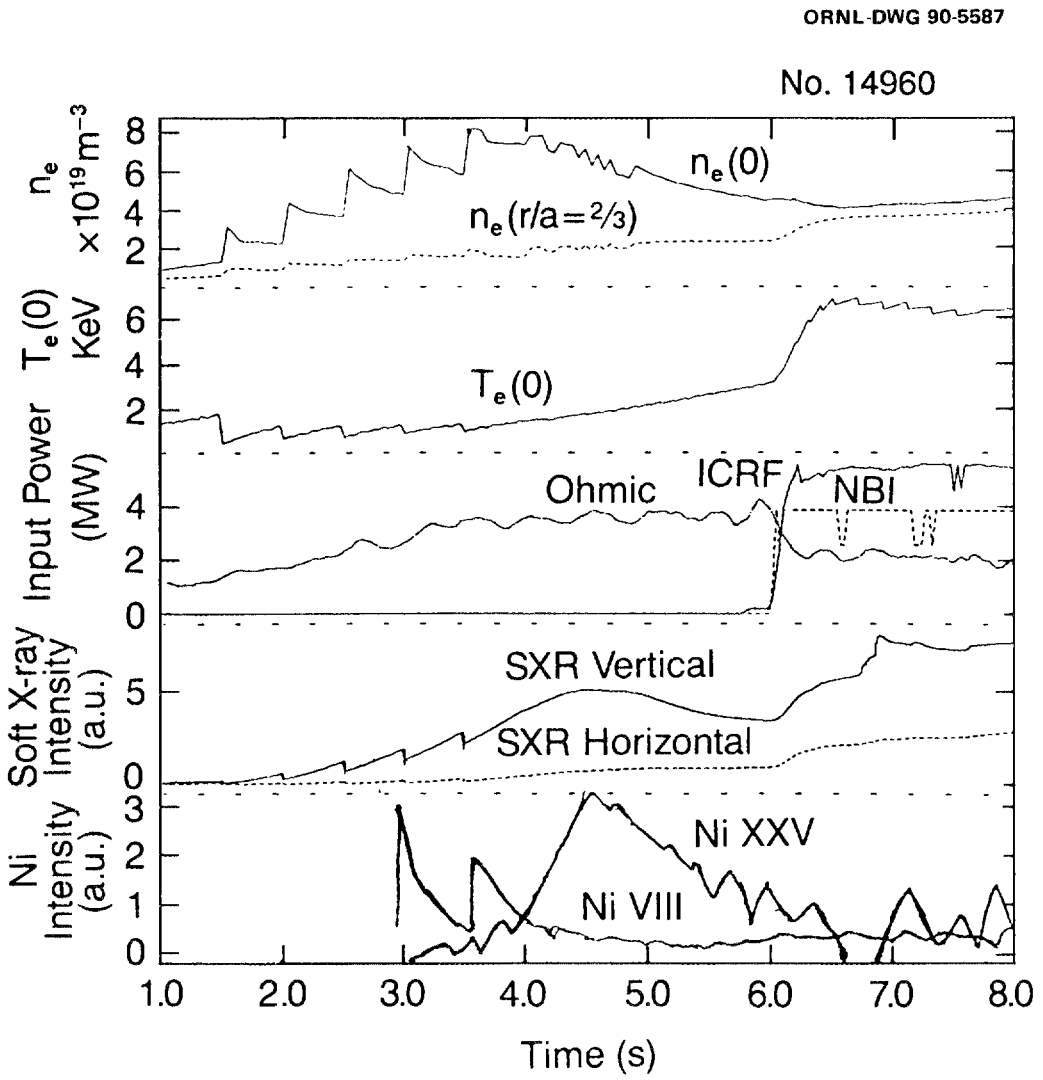

Fig. 3.17 Plasma parameters and impurity radiation after multi-pellet fueling with peaked density profile. 2.7 mm pellets are injected at 1.5, 2, 2.5, 3, and 3.5 s with central penetration.

CHAPTER 4

PARTICLE TRANSPORT IN TOKAMAKS

In this chapter we examine the theoretical models for particle transport in tokamaks. We start with the classical transport, which predicts the diffusion in a cylindrical plasma. When corrections to the classical transport due to toroidal geometry and applied electric fields are incorporated, we arrive at neoclassical transport theory. The transport of particles and energy in tokamaks has been found to be highly anomalous, especially for electrons. This anomalous transport behavior is presumed to be caused by fluctuation driven turbulence in the plasma; therefore, we examine the effect of fluctuations on particle transport. Both neoclassical transport theory and fluctuation induced transport theory of tokamaks are thoroughly discussed in the literature, and we present here only enough of the framework of these subjects to assist in the understanding of the present investigation.

4.1 Classical Transport

Classical transport is the transport in cylindrical geometry that arises from the scattering of electrons and ions in their gyro-orbits by Coulomb collisions. This diffusive process is a random walk where the step size is the particle gyroradius, given by

$$r_L = \omega_{ce} v_{th} \,, \tag{4.1}$$

where ω_{ce} is the electron cyclotron frequency and v_{th} is the thermal velocity. This diffusion, which is driven by its own density gradient, follows Fick's law of diffusion [44], for species a,

$$\Gamma_a = -\mathrm{D}\nabla n_a, \tag{4.2}$$

where the parameter D is the diffusion coefficient and is given by

$$\mathrm{D} = \frac{\langle \triangle r^2 \rangle}{2\tau_s}, \tag{4.3}$$

where $\triangle r$ is the radial excursion between scattering times τ_s. The classical diffusion coefficient for electrons is therefore

$$\mathrm{D} = \frac{r_L^2}{2\tau_c} = \frac{v_{th}^2}{2\,\omega_{\mathrm{ce}}^2}. \tag{4.4}$$

A rigorous derivation of classical transport can be obtained from the Boltzmann equation for species a

$$\frac{\partial f_a}{\partial t} + \vec{v}_a \cdot \frac{\partial f_a}{\partial r} + \frac{\mathrm{F}}{m_a}\frac{\partial f_a}{\partial v} = \left(\frac{\partial f_a}{\partial t}\right)_{\mathrm{coll}} + S_a, \tag{4.5}$$

where $f_a(r, v)$ is the N particle distribution function, $(\partial f_a/\partial t)_{\mathrm{coll}}$ represents change in the distribution function due to collisions, and S_a is a term due to sources and sinks of particles. It is the collisional term that determines the transport properties of the plasma. The velocity $\vec{v}$ of a particle of species a can be decomposed into the average velocity, $\vec{v}_a$, and the random thermal velocity about the average, $\vec{v}_{th}$,

$$\vec{v} = \vec{v}_a + \vec{v}_{th}. \tag{4.6}$$

To derive the transport properties from the Boltzmann equation, it is necessary to take the velocity moments of this equation. The even moments ($v^0 = 1$

and $\frac{1}{2}mv^2$) express the conservation of particles and energy and may be written as

$$\frac{\partial n_a}{\partial t} + \nabla \cdot (n_a \vec{v}_a) = S_a^0 , \tag{4.7}$$

$$\frac{1}{2}\frac{\partial}{\partial t}(Tr\, M_a) + \nabla \cdot Q_a = n_a e_a \vec{v}_a \cdot \vec{E} + R_a^2 + S_a^2 , \tag{4.8}$$

where $Tr\, M_a = n_a m_a \langle \vec{v} \cdot \vec{v} \rangle_a$ is the trace of the momentum stress tensor, $Q_a = \frac{1}{2} m_a n_a \langle (\vec{v} \cdot \vec{v}) v \rangle_a$ is the energy flux, R_a^2 is the second moment of the collision term, and S_a^2 is the second moment of the source term. The odd first moment ($m\vec{v}$) expresses the conservation of momentum, which can be written as

$$m_a \frac{\partial}{\partial t} n_a \vec{v}_a + \nabla \cdot M_a - n_a e_a (\vec{E} + \vec{v}_a \times \vec{B}) = R_a^1 + S_a^1 . \tag{4.9}$$

Similar expressions arise for the higher order moments. Closure of these moment equations can only be made for a specific form for $(\partial f_a / \partial t)_{\text{coll}}$. These equations can be transformed by using the velocity decomposition to decompose the terms into parts with the net flow of plasma (v_a) and parts associated with the random thermal motion of the particles (v_{th}). For example, the momentum balance equation becomes

$$m_a n_a \frac{\partial \vec{v}_a}{\partial t} + m_a n_a (\vec{v}_a \cdot \nabla) \vec{v}_a + \nabla p_a + \nabla \cdot \vec{\pi}_a = n_a e_a (\vec{E} + \vec{v}_a \times \vec{B})$$
$$+ R_a^1 + (S_a^1 - m_a \vec{v}_a S_a^0), \tag{4.10}$$

where the momentum stress tensor $M = n_a m_a \vec{v}_a \cdot \vec{v}_a + P_a$, and $\vec{\pi}_a$ represents the off-diagonal components of the pressure tensor P_a.

If we consider a source-free plasma with isotropic pressure, the momentum balance for species a becomes

$$\nabla p_a = n_a e_a(\vec{E} + \vec{v}_a \times \vec{B}) + \vec{R}_a^1. \tag{4.11}$$

In a simple cylinder of plasma, the radial component of Eq. (4.11) becomes, in (r, θ, z) coordinates,

$$\frac{\partial p_a}{\partial r} = n_a e_a(E_r + v_{a\theta} B_z - v_{az} B_\theta) + R_{ar}^1, \tag{4.12}$$

and the poloidal component is

$$\frac{1}{r}\frac{\partial p_a}{\partial \theta} = n_a e_a(E_\theta - v_{ar} B_z) + R_{a\theta}^1 . \tag{4.13}$$

By assuming poloidal symmetry in p_a and Φ, the poloidal component equation can be written as

$$\frac{1}{r}\frac{\partial p_a}{\partial \theta} - n_a e_a E_\theta = 0 = -n_a e_a v_{ar} B_z + R_{a\theta}^1 , \tag{4.14}$$

from which the radial flux can be seen to be driven by the poloidal collision operator

$$n v_{ar} = \frac{R_{a\theta}^1}{e_a B_z}. \tag{4.15}$$

Hence it is necessary to evaluate this collisional friction operator, given by

$$\vec{R}_a^1 = m_a \sum_{a \neq b} \int C_{ab}(f_a, f_b) \vec{v}\, d^3 v . \tag{4.16}$$

In this evaluation, the Lorentz form of the collision operator can be used; it models energetic electrons scattering off cold infinite-mass ions, $m_a \ll m_b$ and $v_a \gg v_b$. This gives for the collisional friction operator [45]

$$\vec{R}_a^1 = \sum_{a \neq b} n_a m_a \nu_{ab} (\vec{v}_a - \vec{v}_b). \tag{4.17}$$

Substitution of this expression into Eq. (4.15) gives the expression for the radial particle flux,

$$n v_{ar} = -\sum_{a \neq b} \frac{n_a m_a \nu_{ab}}{e_a^2 B_z^2} \left[\frac{1}{n_a Z_a} \frac{\partial p_a}{\partial r} - \frac{1}{n_b Z_b} \frac{\partial p_b}{\partial r} + (v_a - v_b) \frac{B_\theta}{B_z} \right], \tag{4.18}$$

where the last term is small for tokamaks. The radial flux can be seen to be driven by differences in radial pressure gradients among the particle species present. In the absense of sources, a steady-state solution requires the radial particle flux to vanish. This implies that for $T_a = T_b$ and $B_\theta \ll B_z$

$$\frac{n_a(r)}{n_a(0)} = \left[\frac{n_b(r)}{n_b(0)} \right]^{Z_a/Z_b} \tag{4.19}$$

From this equation one can see that in an electron-ion-impurity plasma with ion density peaked toward the center, impurities will tend to accumulate on axis; however, temperature gradients and particle sources that are always present in the system may tend to reduce this effect.

4.2 Neoclassical Transport in Tokamaks

In a tokamak plasma with nested toroidal magnetic surfaces, there is an additional loss rate of particles resulting from Coulomb collisions that is known as neoclassical transport and is due to the toroidal geometry and subsequent non-uniformity of the magnetic field as described in Sect. 1.2. An analogy is that the

gyromotion collisions lead to classical transport and the guiding center motion gives rise to neoclassical transport.

The toroidal magnetic field in a tokamak is proportional to $1/R$ and can be approximated by

$$B = \frac{B_0}{1 + (r/R)\cos\theta}. \tag{4.20}$$

This leads to two classes of particles in tokamaks: those that are free to follow the helical field lines around the torus (passing particles) and those that are trapped in the magnetic well formed by the poloidal variation of the magnetic field (trapped particles), as shown in Fig. 4.1.

ORNL-DWG 89M-2652 FED

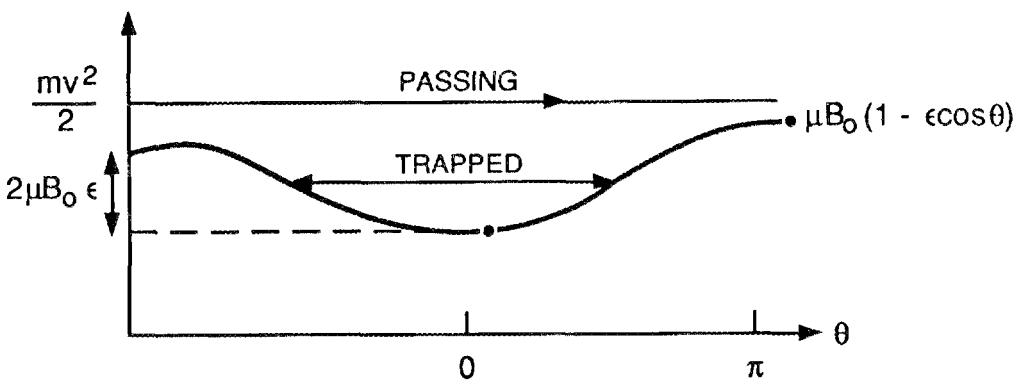

Fig. 4.1 Magnetic well caused by nonuniform magnetic field.

4.2.1 Electron and ion transport

Neoclassical transport takes on different forms, depending on the collision frequency between the species in the plasma. Three collisional regimes have been identified to describe neoclassical transport. The collisional, *Pfirsch-Schlüter*, regime is where a particle suffers a collision before it moves along a field line from the inside to the outside of the torus. The *banana* regime is sufficiently collisionless that a trapped particle completes a bounce orbit in less than a collision time. The *plateau* regime is where the collision frequency lies between the limits of the other two regimes. In all regimes, the particle flux is limited by the electron transport.

In the calculation of the neoclassical fluxes, a more elaborate collisional friction term is used:

$$R_{a\|} = -R_{b\|} = -C_1 m_a N_a \nu_{ab} u_\| - c_2 n_a \nabla_\| T_a, \tag{4.21}$$

where a and b are unlike species and

$$u_\| = u_{a\|} - u_{b\|}. \tag{4.22}$$

The first term is essentially the friction term derived for the classical case. A flux surface average of the radial flux is evaluated, where the flux surface average for a parameter A is defined by:

$$\langle A \rangle = \frac{1}{2\pi} \int_0^{2\pi} h(r,\theta) A(r,\theta) d\theta, \tag{4.23}$$

where $h(r,\theta) \equiv 1 + \frac{r}{R} \cos\theta \equiv 1 + \epsilon \cos\theta$. It can be shown [45,46] that the flux-surface-averaged *Pfirsch-Schlüter* flux is given by

$$\Gamma_a^{PS} = \langle n_a v_{ar}^{PS} \rangle$$

$$\approx \frac{-2\epsilon^2 n_a m_a \nu_{ab}}{(Z_a e B_\theta)^2}\left[\left(C_1 + \frac{C_2}{C_3}\right)\left(\frac{1}{n_a}\frac{\partial p_a}{\partial r} - \frac{Z_a}{Z_b}\frac{\partial p_b}{\partial r}\right) - \frac{5}{2}\frac{C_2}{C_3}\frac{\partial T_b}{\partial r}\right], \tag{4.24}$$

where C_1, C_2, and C_3 are constants of order unity, which were introduced through the collision operator. This expression has a form similar to the classical expression and can be written as

$$\Gamma_a^{PS} = 2\left(\frac{\epsilon B_\phi}{B_\theta}\right)^2 \Gamma_a^{CL} = 2\,q^2 \Gamma^{CL}. \tag{4.25}$$

Although *Pfirsch-Schlüter* transport is present in all collisionality regimes, the low-collisionality regime is dominated by banana transport arising from the scattering of guiding centers between trapped orbits. The velocity of a particle parallel to the nonuniform magnetic field is given by

$$v_\parallel(\theta) = \left[v^2 - \frac{2\mu_0 B}{m}\frac{1}{h(r,\theta)}\right]^{1/2}. \tag{4.26}$$

It can be shown that for a particle to be trapped in the well it must satisfy the condition

$$v_\parallel^2(\theta_t) < \frac{4\mu_0 B\epsilon}{m} \approx 2\epsilon\, v_{th}^2. \tag{4.27}$$

While the particle is trapped, it experiences a ∇B drift velocity given by

$$v_{\nabla B} = \frac{1}{2}\left(\frac{mv^2}{eB}\right)\frac{B \times \nabla B}{B^2}, \tag{4.28}$$

which spreads the orbit in radius giving the characteristic "banana" orbit as shown in Fig. 4.2. The bounce time between end points of the orbit is given by the length of the closed orbit for a marginally trapped particle, $2\,qR_0$, divided by the parallel velocity from Eq. (4.27),

ORNL-DWG 89M-2653 FED

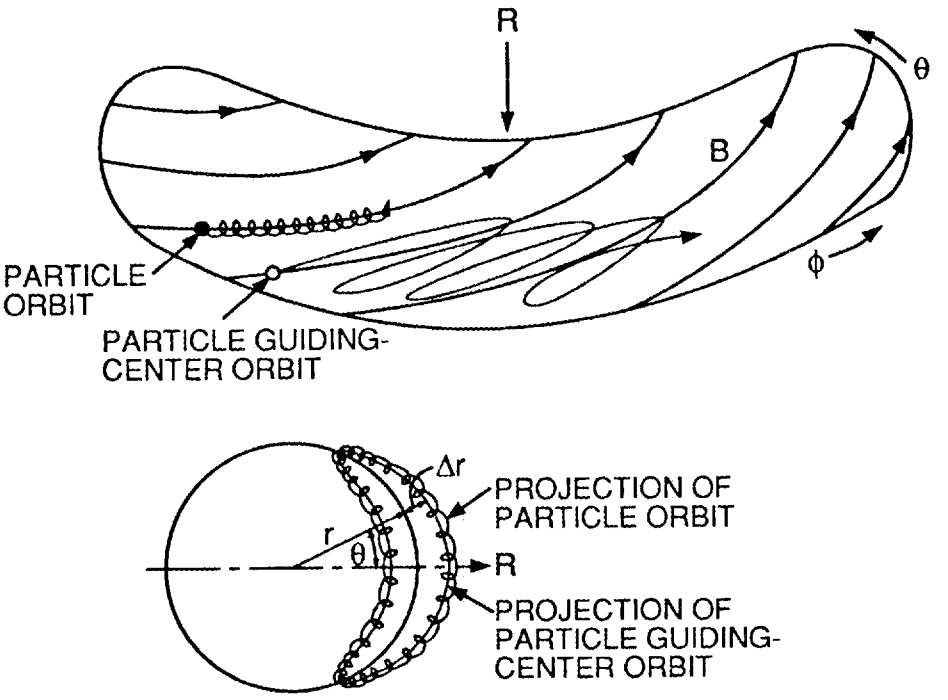

Fig. 4.2 Schematic of trapped-particle orbits in a tokamak. The banana width is given by $r_B = 2\Delta r$.

$$\tau_b \simeq \frac{2Rq}{v_{\|}} = \sqrt{2}\frac{Rq}{\epsilon^{1/2}\, v_{th}}. \tag{4.29}$$

Hence the radial excursion, $\triangle_b$, when a particle is scattered between adjacent banana orbits is:

$$\triangle_b = v_D \tau_b \approx \frac{mv^2}{eBR} \cdot \frac{Rq}{\epsilon^{1/2} v} \approx \frac{r_L q}{\epsilon^{1/2}}, \tag{4.30}$$

where r_L is the Larmor radius. The transport arising from scattering between orbits can be estimated using the random walk expression:

$$\mathrm{D} = \frac{\langle \Delta_b \rangle^2}{\tau}, \tag{4.31}$$

where $1/\tau$ is the effective collision frequency $1/\epsilon\,\tau_{\mathrm{coll}}$. The factor ϵ is included to take account of particles that are scattered into a trapping well. This gives:

$$\mathrm{D} = \epsilon^{1/2}\left(\frac{r_L q}{\epsilon^{1/2}}\right)^2 \frac{1}{\epsilon\,\tau}, \tag{4.32}$$

where $\epsilon^{1/2}$ is the fraction of particles which lie in trapped orbits. Comparison between *Pfirsch-Schlüter* and classical diffusion shows an enhancement due to this process:

$$\mathrm{D}^B \approx \epsilon^{-3/2}\mathrm{D}^{PS} \approx \epsilon^{-3/2} q^2 \mathrm{D}^{CL}. \tag{4.33}$$

A formal derivation of banana transport follows the analysis of the *Pfirsch-Schlüter* case with a different form of the collision operator and transformation of the Boltzmann equation to guiding center coordinates [45].

All regimes of collisionality may be relevant in a given plasma at different minor radii, since the collisionality is a function of minor radius, density, and temperature. Furthermore, given any Maxwellian distribution at a given temperature, some particles in the distribution are in each regime. The results of the neoclassical theory [46,47] have been expressed as continuous functions of collisionality through least-squares fits to the results for the different regimes. The transport calculations yield a resulting expression for the flux-surface-averaged radial electron particle flux

$$\Gamma_{er} = -\frac{2\epsilon^{1/2} n_e m_e T_e}{(eB_\theta)^2}\nu_e\left(K_{11}A_{1e} + K_{12}\frac{1}{T_e}\frac{\partial T_e}{\partial r}\right)$$

$$- K_{13} \frac{n_e \epsilon^{1/2}}{B_\theta} \langle E_\parallel / h \rangle. \tag{4.34}$$

The term A_{1e} in Eq. (4.34) is given by

$$A_{1e} = \frac{\partial}{\partial r} \ln p_e - \frac{5}{2} \frac{\partial \ln T_e}{\partial r} + (T_i / Z_i T_e) \left[\frac{\partial}{\partial r} \ln p_i - \frac{(\beta_1, g_{2i})}{1 + \nu_e^{*2} \epsilon^2} \frac{\partial \ln T_i}{\partial r} \right], \tag{4.35}$$

where (β_1, g_{2i}) is a dimensionless coefficient dependent on the ion collisionality and where the collisionality parameter ν_e^*, is the ratio of effective electron collision frequency to electron bounce frequency. This parameter is defined as

$$\nu_e^* = \sqrt{2}\, r B_\phi / \left(B_\theta v_{the} \tau_e \epsilon^{3/2} \right), \tag{4.36}$$

where $v_{the} \equiv (2T_e/m_e)^{1/2}$ and τ_e is the electron-ion momentum exchange time or electron collision time and is defined as

$$\tau_e = 6\pi (2\pi m_e)^{1/2} \epsilon_0^2\, T_e^{3/2} / n_i Z_i^2 e^4 \ln \Lambda\,. \tag{4.37}$$

The resulting ion particle heat flux is given by ambipolarity constraints to be

$$\Gamma_{ir} = -Z_i\, \Gamma_{er}\,. \tag{4.38}$$

The coefficients, K_{mn}, for n or $m = 1, 2$ are fit by

$$K_{mn} = K_{mn}^0 \left[\frac{1}{1 + a_{mn} \sqrt{\nu_e^*} + b_{mn} \nu_e^*} + \frac{\epsilon^3 (c_{mn}^2 / b_{mn}) \nu_e^*}{1 + c_{mn} \nu_e^* \epsilon^{3/2}} \right], \tag{4.39}$$

and by

$$K_{m3} = K_{m3}^0 \left(1 + a_{m3} \sqrt{\nu_e^*} + b_{m3} \nu_e^* \right)^{-1} \left(1 + c_{m3} \nu_e^* \epsilon^{3/2} \right)^{-1}, \tag{4.40}$$

for $n = 3$. The numerical coefficients a_{mn}, b_{mn}, and c_{mn} are given in Ref. [46]. The last term of the particle transport equation, $-K_{13} n_e \epsilon^{1/2} \langle E_\parallel / h \rangle / B_\theta$, arises from the trapped particles, which spend unequal amounts of time in the upper and lower halves of the torus when a toroidal electric field is present. The drifts do not exactly cancel, which leads to a net radial inward particle drift known as the "Ware-pinch" effect [48]. This can be seen in the *banana* regime from the conservation of toroidal canonical momentum for trapped particles, given by

$$\frac{d}{dt}(mv_\phi + eA_\phi) = 0\,, \tag{4.41}$$

where A_ϕ is the vector potential. Averaging over the bounce motion of the trapped particles leads to

$$\frac{\partial}{\partial t} A_\phi + v_r \frac{\partial A_\phi}{\partial r} = 0\,. \tag{4.42}$$

Therefore, the trapped particles have an inward radial drift $v_r \sim -E_\phi / B_\theta$ and, since the trapped fraction is $\epsilon^{1/2}$, the Ware pinch flux is given by

$$\Gamma = -\epsilon^{1/2} n E_\parallel / B_\theta \tag{4.43}$$

in the *banana* regime. The term K_{13} in Eq. (4.34), which is expanded in detail in Eq. (4.40), then takes into account the change in trapped-particle effects, which diminish as $\nu_e^{*\,-1}$ in the *plateau* regime.

Similarly, the neoclassical electron heat flux has been derived using the moments method and has the form

$$q_{er} + \frac{5}{2} T_e \Gamma_{er} = - \frac{2\,\epsilon^{1/2} n_e m_e T_e^2}{(eB_\theta)^2} \nu_e \left(K_{12} A_{1e} + K_{22} \frac{1}{T_e} \frac{\partial T_e}{\partial r} \right)$$
$$- K_{23}\, \epsilon^{1/2} \frac{n_e T_e}{B_\theta} \langle E_\parallel / h \rangle \,. \tag{4.44}$$

The terms of Eqs. (4.34) and (4.44) can be written in the form of a diffusivity (D) or heat conductivity (χ) times a density or temperature gradient. The dependence of the these transport coefficients on collision frequency is illustrated qualitatively in Fig. 4.3. In both the *banana* (collisionless) and *Pfirsch-Schlüter* (collisional) regimes, the transport coefficients are proportional to ν_e^*, but they are independent of ν_e^* in the *plateau* regime. The classical transport coefficients are shown in the figure to be much smaller than the neoclassical terms.

The neoclassical fluxes (moments of the distribution) can then be written in matrix notation [49] with the forces in Onsager symmetry as

$$\begin{pmatrix} \Gamma_e \\ q_e \\ J_\parallel - \sigma_\parallel E_\parallel^A \end{pmatrix} = - \begin{pmatrix} D_e & L_{12} & W \\ L_{21} & \chi_e & L_{23} \\ J_b & L_{32} & \sqrt{\epsilon}\sigma_\parallel \end{pmatrix} \begin{pmatrix} \frac{dn}{dr} \\ \frac{dT_e}{dr} \\ E_\parallel^A \end{pmatrix}, q_i = n\chi_i \frac{dT_i}{dr}, \tag{4.45}$$

where Γ_e is the particle flux, q is the heat flux, D_e is the electron particle diffusivity, χ_e is the electron heat diffusivity, W is the Ware pinch effect, J_b is the bootstrap current, ϵ is the inverse aspect ratio r/R, $E_\parallel^A$ is the parallel inductive electric field, $\sigma_\parallel$ is the parallel conductivity, and L_{ij} are low-order cross terms. Both the bootstrap current and the electrical conductivity have been measured in tokamaks and have been found to agree reasonably well with neoclassical theory. The radial heat and particle transport, however, has been determined to be highly anomalous. Thus, the electron collisional processes parallel to the magnetic

ORNL-DWG 89M-2917 FED

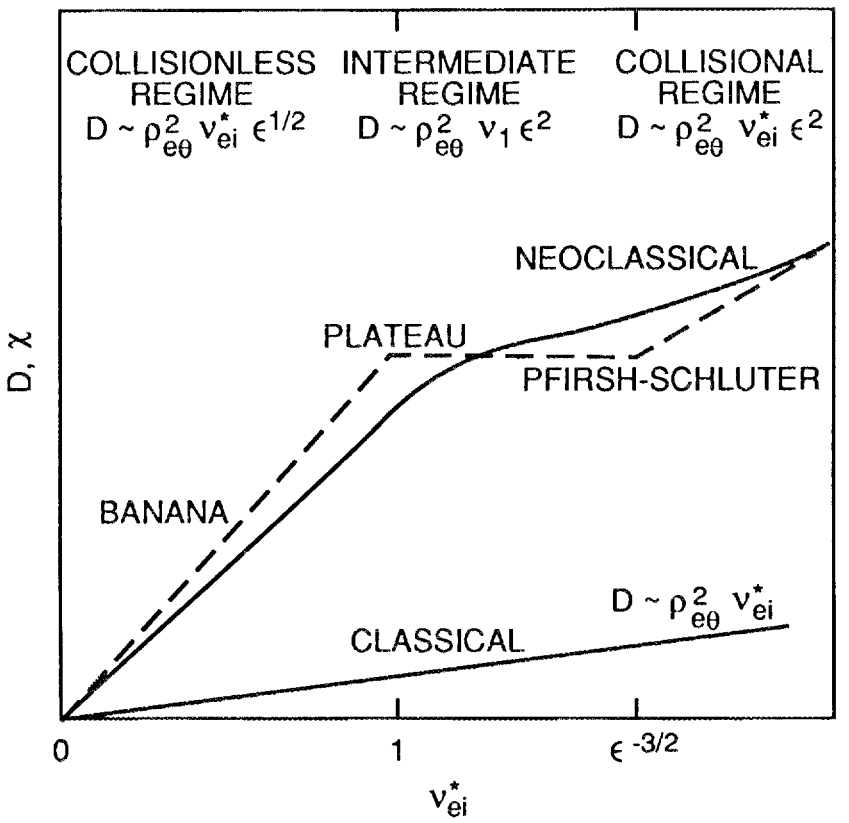

Fig. 4.3 Schematic representation of neoclassical particle and thermal diffusivity coefficients (D, χ) as a function of the electron-ion collision frequency ν_{ei}^*. The smoothed curve is a numerical approximation.

field agree well with neoclassical theory predictions, while the perpendicular transport is highly anomalous.

4.2.2 Impurity transport

The neoclassical theory of impurity transport is highly developed despite the complexity of dealing with an arbitrary number of species [50]. For simplicity, we discuss a single impurity species in one charge state in a background hydrogenic plasma. The impurity flux $\Gamma_{\rm I}$ can be written as the sum of three terms which exist in all collisionality regimes:

$$\Gamma_{\rm I} = \Gamma_{\rm I}^{CL} + \Gamma_{\rm I}^{PS} + \Gamma_{\rm I}^{BP}\,, \tag{4.46}$$

where $\Gamma_{\rm I}^{CL}$ is the classical flux driven by the perpendicular friction force, $\Gamma_{\rm I}^{PS}$ is the *Pfirsch-Schlüter* neoclassical flux driven by poloidal variation of the parallel friction force, and $\Gamma_{\rm I}^{BP}$ is the *banana-plateau* neoclassical flux driven by pressure anisotropy associated with viscous forces and is important in low collisionality of the impurity ions.

The frequency of ion collisions with impurities can greatly exceed that of collisions between ions and electrons, so the former induce a greater impurity flux and an oppositely directed ion flux. Impurities tend to lie in the *Pfirsch-Schlüter* (collisional) regime due to their mass and charge. The component of plasma ion transport due to collisions with impurities is also in the *Pfirsch-Schlüter* regime since the impurities experience only *Pfirsch-Schlüter* transport.

The full neoclassical treatment gives the following expression for the radial impurity flux in the *Pfirsch-Schlüter* regime, including the classical value [51]:

$$\Gamma_{\rm I}^{PS} = 0.5\frac{\rho_{\rm i}^2(1+2q^2)}{\tau_{\rm iI}Z_{\rm I}}\left[\frac{\partial n_{\rm i}}{\partial r} - \frac{n_{\rm i}}{n_{\rm i}Z_{\rm I}}\frac{\partial n_{\rm I}}{\partial r} - \left(\frac{1}{2}+\frac{1}{Z_{\rm I}}\right)\frac{n_{\rm i}}{T_{\rm i}}\frac{\partial T_{\rm i}}{\partial r}\right], \tag{4.47}$$

where the subscript i refers to the hydrogenic ions and the subscript I refers to the impurity ions. The impurity temperature is assumed to be equal to the hydrogenic ion temperature $T_I = T_i$. The steady-state ($\Gamma_I = 0$) solutions of the equation for the *Pfirsch-Schlüter* impurity flux give:

$$\frac{n_I(r)}{n_I(0)} = \left[\frac{n_i(r)}{n_i(0)}\right]^{Z_I/Z_i} \left[\frac{T_i(0)}{T_i(r)}\right]^{Z_I/2+1}. \tag{4.48}$$

The ion temperature gradient in the usual direction will then act to drive impurities out of the central region.

Similarly the full neoclassical treatment gives the following expression for the radial impurity flux in the *banana-plateau* regime [51]:

$$\Gamma_I^{BP} = 1.25\frac{q}{R}{m_I}^{1/2}\frac{T_i^{3/2}c^2 n_I}{B_T^2 {Z_I}^2 e^2}\left[\frac{Z_I}{n_i}\frac{\partial n_i}{\partial r} - \frac{1}{n_I}\frac{\partial n_I}{\partial r} + 1.5\left(\frac{Z_I}{T_i}\frac{\partial T_i}{\partial r}\right)\right]. \tag{4.49}$$

The steady state ($\Gamma_I = 0$) solutions of the equation for the *banana-plateau* impurity flux give

$$\frac{n_I(r)}{n_I(0)} = \left[\frac{n_i(r)}{n_i(0)}\right]^{Z_I/Z_i} \left[\frac{T_i(r)}{T_i(0)}\right]^{3Z/2}. \tag{4.50}$$

In the *banana-plateau* regime, then, with density and temperature gradients in the usual direction (negative), the impurities will be strongly peaked on axis relative to the hydrogenic ions.

In the absence of temperature gradients, the neoclassical prediction is clear for all collisionality regimes: impurities are expected to peak strongly on axis as compared to the hydrogenic ion density. The total impurity flux is usually written as a sum of a diffusive component and a convective term proportional to the density:

$$\Gamma_{\mathrm{I}} = -D_{\mathrm{I}} \frac{\partial n_{\mathrm{i}}}{\partial r} - v_{\mathrm{I}} n_{\mathrm{I}} \,, \tag{4.51}$$

where v_{I} is radially inward if positive. Neoclassical values of D and v can be given for the above expressions of the fluxes. Note that gradients in the temperature in the usual direction give rise to outward convection in the *classical Pfirsch-Schlüter* regime; however, in the *banana-plateau* regime the convection from temperature gradients is inward.

4.3 Fluctuation Induced Transport in Tokamaks

Fluctuations in the density, $\tilde{n}$, electrostatic potential, $\tilde{\phi}$, and magnetic field, $\tilde{B}$, are known to exist in tokamak plasmas and are presumed to be caused by collective instabilities in the plasma. These fluctuations will have an effect on transport through enhanced collisions and will lead to anomalous transport. In this section we discuss the basic physics of fluctuation induced transport and show how it is applied to tokamaks.

The electron particle flux perpendicular to the magnetic surface can be expressed as

$$\Gamma_{\mathrm{e}} = \langle \tilde{n}_{\mathrm{e}} \cdot \tilde{v}_r \rangle \,, \tag{4.52}$$

where the angle brackets denote a flux surface average and time average over a time scale long compared to the frequency of the fluctuations. $\tilde{v}_r$ is the fluctuation of the fluid velocity perpendicular to the flux surface given by

$$\tilde{v}_r \cong \frac{\tilde{E}_\theta}{B} + \frac{v_\parallel \tilde{B}_r}{B} \,, \tag{4.53}$$

where $\tilde{B}_r$ is the radial perturbation to the magnetic field and $v_{\|}$ is the particle velocity along the unperturbed magnetic field B. The contribution of the fluctuation to the transport of particle and heat depends on the correlations of the fluctuating quantities,

$$\Gamma_e = \frac{\langle \tilde{n}_e \cdot \tilde{E}_\theta \rangle}{B} - \frac{\langle \tilde{j}_{\|} \cdot \tilde{B}_r \rangle}{eB}, \tag{4.54}$$

where $\tilde{j}_{\|}$ is the fluctuation in the parallel electron current. An anomalous effective particle diffusion coefficient can then be defined as $\mathrm{D} = -\Gamma/(dn/dr)$. The particle flux from the fluctuation driven turbulence is expected to be ambipolar irrespective of the radial electric field in quasi-neutral plasmas due to charge conservation and the quasi-neutrality constraint [52] given in the charge conservation equation:

$$\frac{\partial \rho(r,t)}{\partial t} + \nabla \cdot \vec{j} = 0\,. \tag{4.55}$$

With the quasi-neutrality condition, $\rho(r,t) \sim 0$, the divergence of the current density $\vec{j}$ in Eq. (4.55) is zero, which leads to

$$\int_\Psi \vec{j} \cdot d\sigma = \int_\Psi (n\vec{v}_i - n\vec{v}_e) \cdot d\sigma = 0\,. \tag{4.56}$$

The ion and electron fluxes are seen to cancel; therefore the turbulent particle fluxes under quasi-neutral conditions must be ambipolar.

The fluctuation induced contribution to the heat flux can be similarly derived. The total heat flux is given by

$$Q_r = \frac{5}{2} T\,\Gamma + q_r = \frac{5}{2}\frac{\langle \tilde{p} \cdot \tilde{\mathrm{E}}_\theta \rangle}{B} + q_r\,, \tag{4.57}$$

where the first term is a convective flux driven by the turbulent particle flux and the second term is the radial turbulent conductive heat flux. The conductive contribution to the radial heat flux can be approximated to second order as

$$q_r = -\kappa_{\|}\left\langle \left|\frac{\tilde{B}_r}{B}\right|^2 \right\rangle - \kappa_{\|}\left\langle \left|\frac{\tilde{B}_r}{B}\right| \frac{d\tilde{T}}{dr} \right\rangle, \tag{4.58}$$

where $\kappa_{\|}$ is the classical conductivity along the magnetic field. Very low levels of magnetic fluctuation, $\tilde{B}_r/B \sim 10^{-4}$, can lead to anomalous thermal conductivities on the order of those observed in tokamaks.

The implication of fluctuations in the plasma is that time-dependent fields can cause anomalous particle and thermal transport across mean magnetic surfaces in magnetic confinement devices such as tokamaks. There are two regimes of fluctuation induced transport as deduced from Eqs. (4.54) and (4.57): one where the $\tilde{\mathrm{E}}_\theta \times B$ transport dominates and one where the $\tilde{B}_r$ driven transport dominates. The difficulty lies in determining the source of the free energy that drives the fluctuations in the first place. A number of possible candidates have been identified. More experimental evidence is needed to determine which mechanisms are responsible and the magnitude of the anomalous transport they generate. To assess the transport due to the fluctuations, one needs to measure the quantities $\tilde{n}, \tilde{\phi}, \tilde{B}$ with their relative phases. Digital spectral analysis techniques have been developed [53] to quantify the statistical properties of fluctuations and have been used to determine particle and heat fluxes driven by electrostatic fluctuations near the plasma edge.

Up to now measurements of density fluctuations have been made in the core of tokamaks; however, density and potential fluctuations and their correlations in the core region have not been measured and therefore direct determination of the transport caused by the fluctuations remains unknown. Measurements

of magnetic fluctuations and resulting transport are even more difficult because there are no developed experimental techniques to carry out such measurements inside a hot plasma. Only pickup coils located at the plasma edge have been used to detect magnetic perturbations on rational surfaces inside the plasma.

CHAPTER 5

PARTICLE TRANSPORT IN JET PELLET FUELED DISCHARGES

The particle transport in pellet fueled JET limiter discharges is examined in this chapter. The methods used to analyze the transport are particle balance calculations and modeling of the electron density evolution with different empirical and theoretical transport coefficient models. In the first section the particle balance calculation method is discussed and typical results obtained from these analyses are shown. In the second section, the particle transport modeling code is discussed and the results from the modeling are compared with results from earlier tokamak experiments. In the last section, the scaling of the effective transport coefficients with various plasma parameters is shown and the implications are discussed.

The particle transport in a number of JET pellet fueled discharges has been studied to determine how the particles, particularly electrons, behave in pellet fueled plasmas under different conditions. Two types of pellet fueling experiments have been investigated extensively. These types of experiments are multiple 2.7 mm pellet injection during the current rise and single 4 mm pellet injection at the beginning of the current flattop. Both of these types of experiments are performed before sawteeth appear [$q(0) > 1$] with the plasma positioned against the two outer toroidal belt limiters and, with central pellet penetration, can lead to highly peaked electron density profiles as discussed in Sect. 3.3.

5.1 Particle Balance Analysis

The electron particle transport is analyzed by making a particle balance calculation of the electron particle flux to determine the magnitude of the different flux components. This calculation is done with a modified version of the time slice interpretive transport code QFLUX [54]. This code calculates the local particle flux for the electrons by taking the volume integral of the rate of change of the density plus any net volume-integrated particle sources and sinks divided by the flux surface area,

$$\Gamma_e(\rho) = \left\{ \int_0^\rho dV \left[-dn_e(\rho)/dt + s_e^{in}(\rho) - s_e^{out}(\rho) \right] \right\} / A(\rho), \tag{5.1}$$

where $A(\rho)$ is the flux surface area, $s_e^{in}(\rho)$ is the net local source of electrons due to neutral ionization, and $s_e^{out}(\rho)$ is the net local sink of electrons due to recombination with the main plasma species. This net source of electrons can be expressed as

$$s_e = s_e^{in} - s_e^{out} = n_e n_n \langle \sigma v \rangle_i - n_e n_i \langle \sigma v \rangle_r, \tag{5.2}$$

where n_e, n_i, and n_n are the electron, ion, and neutral density, respectively, and $\langle \sigma v \rangle_i$ and $\langle \sigma v \rangle_r$ are rate coefficients for electron impact ionization and recombination with the plasma ions. The net electron source is calculated within QFLUX using a neutral transport model to calculate the neutral density by applying the appropriate cross sections for the ionization and recombination reactions. The neutral transport model uses a slab geometry and assumes the neutral density is made up of a distribution of "cold" neutrals with a temperature in the range of 10 eV and a distribution of "hot" neutrals near the local ion temperature. The ionization and recombination rates are then calculated from these distributions.

The total ionization rate is then normalized to the measured ionization rate as described in Sect. 2.4.4. This electron source calculation has been compared to the results of a three-dimensional Monte Carlo neutral deposition code NIMBUS [55] and found to give reasonable agreement. Both codes show that the source is highly localized at the edge. In general, the edge source is found to fuel only the outer quarter of the minor radius of the plasma due to the relatively large size and high plasma temperatures of JET.

The source of electrons from neutral beam heating deposition is calculated by the neutral beam deposition code PENCIL [54] and is included in the electron source profile. The neutral beam source component in these experiments is not generally a very significant fraction of the total source due to the high density and relatively poor penetration of the beams. A plot of the local electron source profile for an auxiliary heated discharge is shown in Fig. 5.1. As can be seen in this plot, the neutral beam source (for 7 MW NBI) is small compared to the edge neutral source as calculated by QFLUX. The neutral beam fueling is much stronger in the center than the edge fueling, but the central fueling source is more than an order of magnitude smaller than the edge source.

The magnetic surface geometry in QFLUX is represented in the moments representation given in Ref. [56]. The equations for a flux surface are given by

$$R = R_0(\rho) + a\rho\,\cos(\theta) + R_2(\rho)\,\cos(2\theta) \tag{5.3}$$

and

$$z = E(\rho)\big[a\rho\,\sin(\theta) - R_2\,\sin(2\theta)\big]\,, \tag{5.4}$$

where a is the minor radius at $z = 0$, such that $0 \leq \rho \leq 1$, and the functions

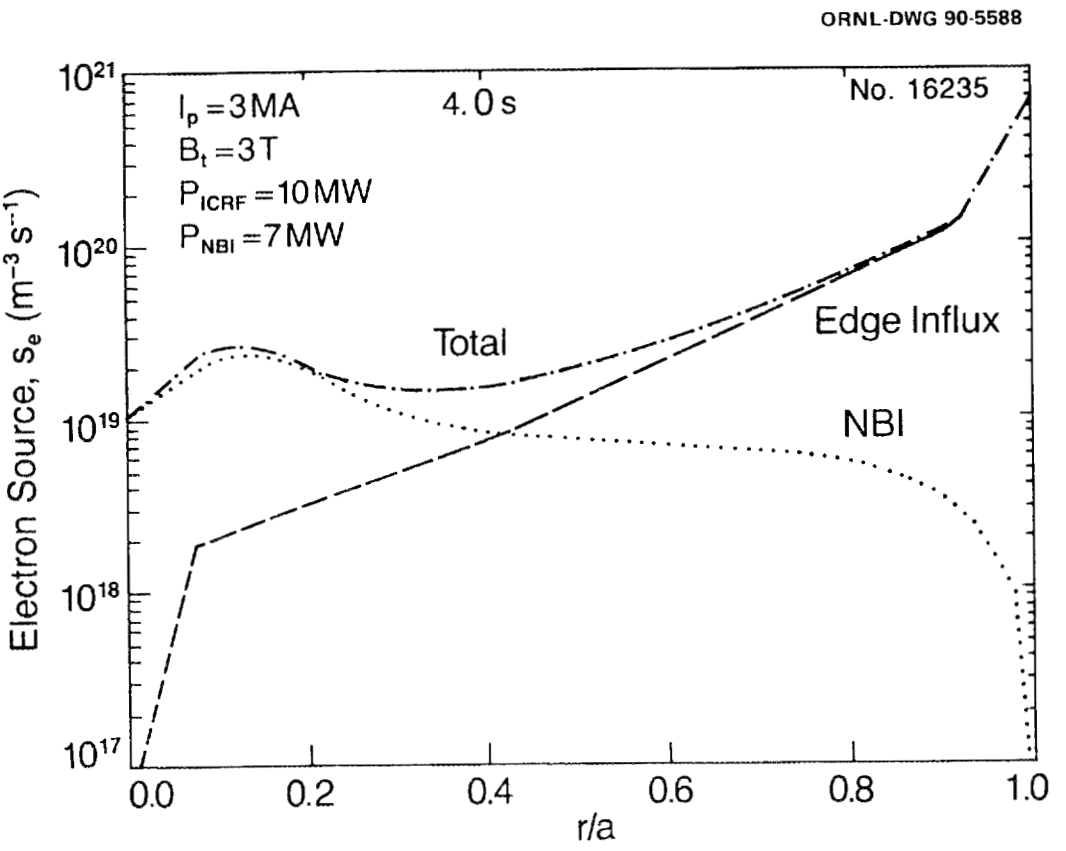

Fig. 5.1 The local electron source profile for an NBI and ICRF heated discharge. The edge influx is calculated by QFLUX and the neutral beam source by PENCIL. The edge source is normalized to the measured D_α source.

$R_0(\rho)$, $R_2(\rho)$, and $E(\rho)$ are determined using a cubic spline interpolation to fit the experimentally derived shift of the magnetic axis, triangularity, and elongation, respectively. The flux surface area, volume, and associated derivatives are then determined from the equations for the magnetic flux surfaces. In particular, $\nabla\rho$ is determined from the relation $|\nabla\rho| = \left[(\frac{\partial\rho}{\partial R})^2 + (\frac{\partial\rho}{\partial z})^2\right]^{1/2}$ and from the Jacobian given by $\tau = \frac{\partial R}{\partial\rho}\frac{\partial z}{\partial\theta} - \frac{\partial R}{\partial\theta}\frac{\partial z}{\partial\rho}$. We are then able to calculate the terms of $\nabla\rho$ from the relations $\partial\rho/\partial R = \frac{1}{\tau}\partial z/\partial\theta$ and $\partial\rho/\partial z = \frac{-1}{\tau}\partial R/\partial\theta$. The derivative of the flux surface volume with respect to ρ, $dV(\rho)/d\rho$, is given by

$$d\,V(\rho)/d\rho = 2\,\pi \int_0^{2\pi} d\theta\, R\,\tau\,. \tag{5.5}$$

For the calculations presented here, the magnetic surface geometry has been represented by 21 such magnetic surfaces.

The neoclassical particle transport coefficients are calculated in QFLUX and are used to determine the fluxes due to the neoclassical collisional transport. By far the dominant neoclassical term for the electrons is the Ware pinch described in Sect. 4.2. The total electron flux and the neoclassical particle flux are shown for a typical pellet fueled discharge in Fig. 5.2. We see in this figure that the Ware flux is much larger than the neoclassical diffusive flux. Clearly, if the only transport processes were collisional, the electron profiles would be very peaked due to the dominant inward Ware pinch flux.

As part of the neoclassical coefficient calculation, the collisionality parameter ν_e^* [as defined in Eq. (4.41)] is calculated across the profile of the discharge. In Fig. 5.3 we show the calculated value of ν_e^* for both an ohmically heated and an ICRF heated pellet fueled discharge. In both cases ν_e^* is well below 1 before the pellet is injected, and only in the ohmic case does ν_e^* go above 1 during the

ORNL-DWG 89M-2992 FED

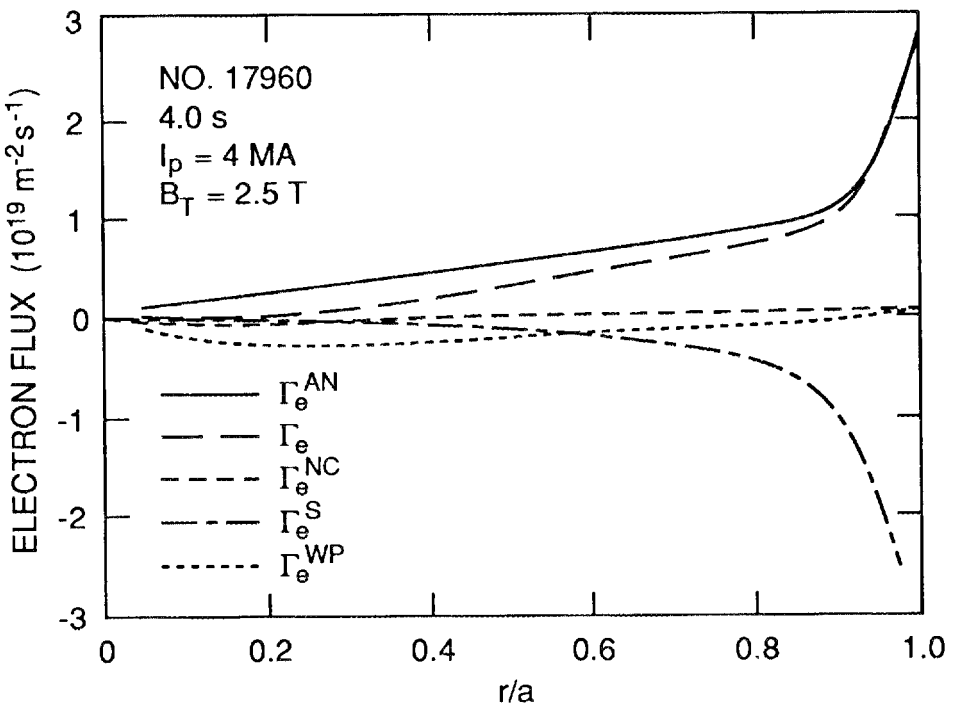

Fig. 5.2 Results of a particle balance calculation of electron particle fluxes. The calculation is done during the ohmic heating decay of a peaked density profile. Negative fluxes represent inward directed particle flux. Γ_e is the measured net total flux, Γ_e^{WP} is the calculated Ware pinch flux, Γ_e^S is the edge source flux (calculated), and Γ_e^{AN} is the calculated anomalous flux ($\Gamma_e^{AN} = \Gamma_e - \Gamma_e^{WP} - \Gamma_e^{NC}$).

ORNL-DWG 90-5589

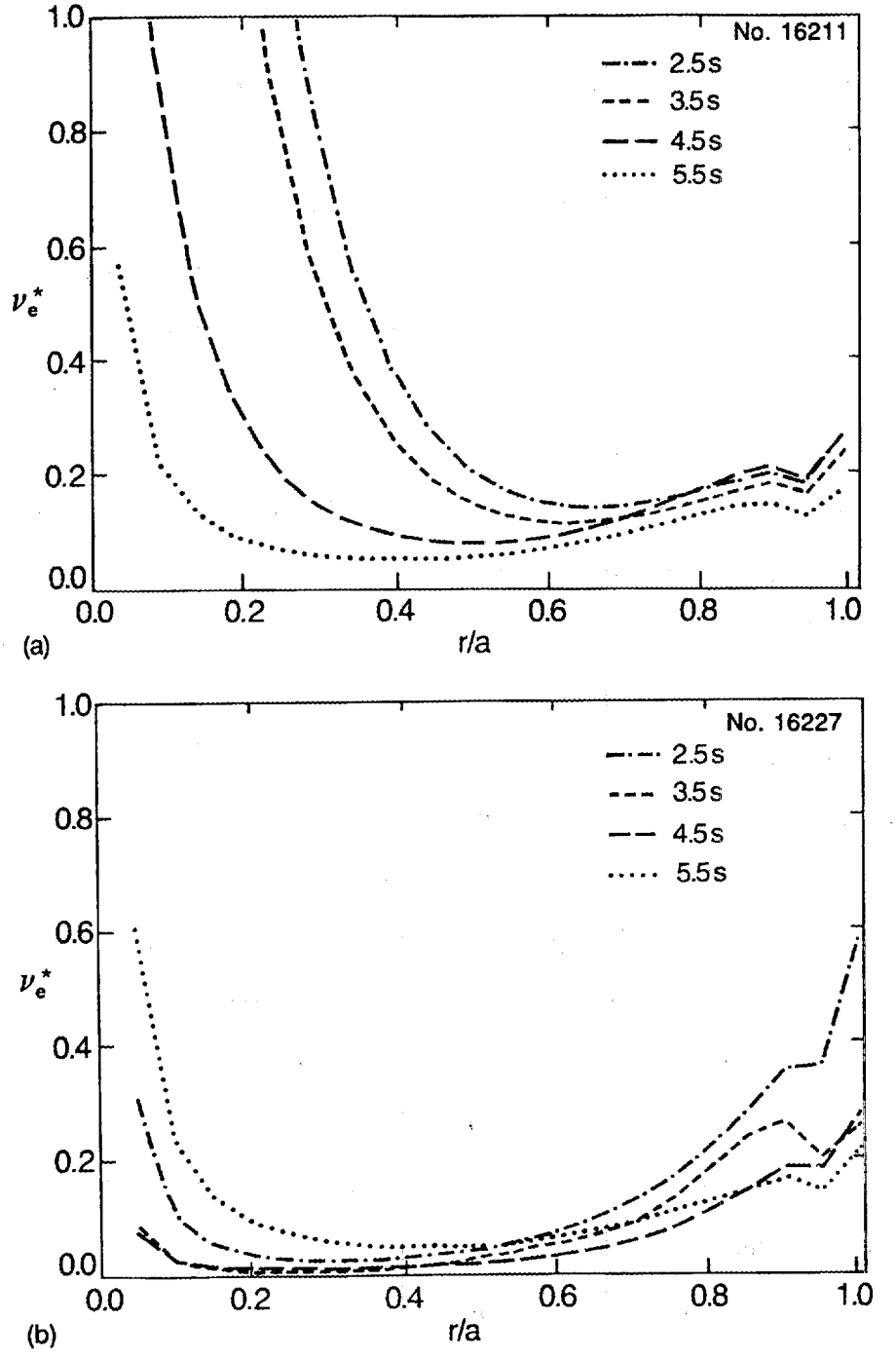

Fig. 5.3 Electron collisionality parameter ν_e^* in pellet fueled JET discharges. (a) Ohmically heated discharge and (b) ICRF heated discharge with a 4 mm pellet injected at 3 s.

reheat period. The discharges are thus in the *banana* (collisionless) regime except when the temperature drops after pellet injection before heating is applied, in which case the center of the discharge is in the *plateau* regime. The parameter $\epsilon^{-3/2}$ in these discharges is generally $\gg 10$ in the central region of the plasma, and thus the plasma is well out of the *Pfirsch-Schlüter* (collisional) regime.

The Ware pinch is driven by the parallel electric field supplied by the transformer action of the poloidal field coil. This electric field is larger during the current ramp-up phase and, since the resistivity is a function of electron temperature, this electric field is found to vary as $\sim T_e^{-3/2}$. Roughly speaking, then, the Ware pinch velocity would be expected to decrease throughout the current rise and also to decrease whenever strong auxiliary heating is applied. This is in fact what calculations of the Ware pinch velocity exhibit, as shown in Fig. 5.4. In these calculations the current is determined from the magnetic equilibrium calculation, and the parallel electric field is determined by applying corrections to neoclassical resistivity. The poloidal magnetic field is determined from the current density, which in turn is taken from the equilibrium calculation. These calculations of the Ware pinch have been compared to the more detailed calculations done with the transport code TRANSP [57], which actually solves for time-dependent magnetic field diffusion. The agreement between the two Ware pinch velocity calculations is in general good and only differs at most on the order of 10% over the entire plasma minor radius.

The particle balance calculation enables a profile of the effective electron particle diffusivity to be determined from the particle flux. In our calculations we have assumed that the inward particle convection is solely due to the neoclassical (Ware) pinch. By taking the measured net particle flux and subtracting the inward convective flux from the Ware pinch, we are able to then derive the

ORNL-DWG 89-3036 FED

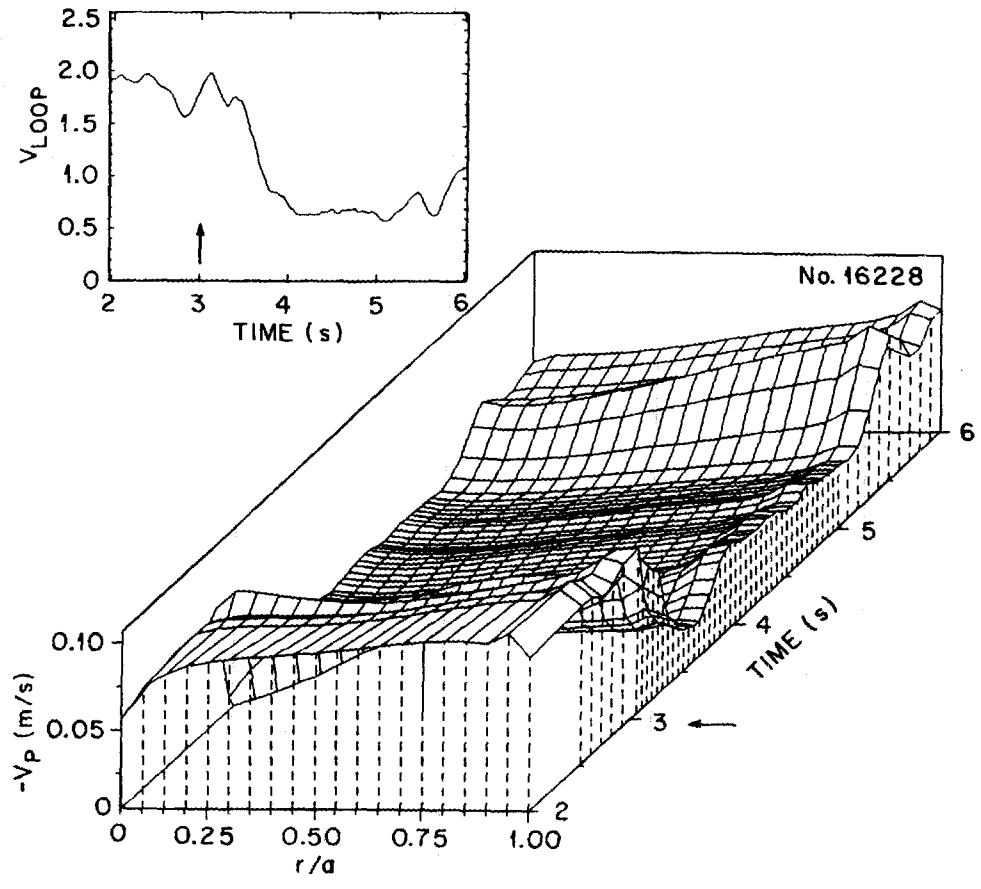

Fig. 5.4 Electron neoclassical (Ware) pinch velocity profile evolution in an ICRF heated, pellet fueled discharge. A 4 mm pellet is injected and ICRF heating started at 3 s. The insert shows the surface loop voltage as a function of time.

remaining diffusive flux. We then divide this flux by the local density gradient and arrive at the effective local particle diffusivity,

$$\mathrm{D}^{\mathrm{PB}}(\rho) = -\left[\Gamma_e(\rho) - v_p^{\mathrm{NC}}(\rho)\, n_e(\rho)\right] / \nabla n_e(\rho)\,, \tag{5.6}$$

where the pinch velocity is inward, $v_p^{\mathrm{NC}} < 0$. The particle balance calculation of the electron diffusivity is incorporated into the modified version of the QFLUX transport code. A typical calculation for the effective diffusivity in a multiple-pellet fueled discharge that develops a peaked density profile is shown in Fig. 5.5. (The density evolution of this discharge is shown in Fig. 3.7). We see in this discharge that before the auxiliary heating is applied, the effective diffusivity remains relatively constant and shows a distinct drop in the central core ($r/a < 0.5$) of the plasma. After the heating is turned on, we see a rise in the central diffusivity to over $0.4\,\mathrm{m}^2/\mathrm{s}$. This increase in effective diffusivity follows the rise in electron temperature and not the applied power.

By plotting the effective diffusive particle flux $[\Gamma_e(\rho) - v^{\mathrm{NC}}(\rho)\, n_e(\rho)]$ as a function of density gradient $[\nabla n_e(\rho)]$ at a specific radius (ρ), we can see if the diffusivity at that radius is a constant and what the magnitude is. In Fig. 5.6 we show an example of a plot of Γ vs ∇n_e for a discharge that has a peaked density profile decaying in an ohmically heated plasma. We see that the diffusivity at $r/a = 0.33$ in this case is relatively constant and has a magnitude of $0.086\,\mathrm{m}^2/\mathrm{s}$. The y-intercept of the plot is virtually zero, indicating that there is no large anomalous convective flux and that the net flux is diffusive during the time shown at this radius in the discharge. This technique of plotting the flux as a function of the density gradient is a useful way of quickly determining the effective particle transport diffusivity.

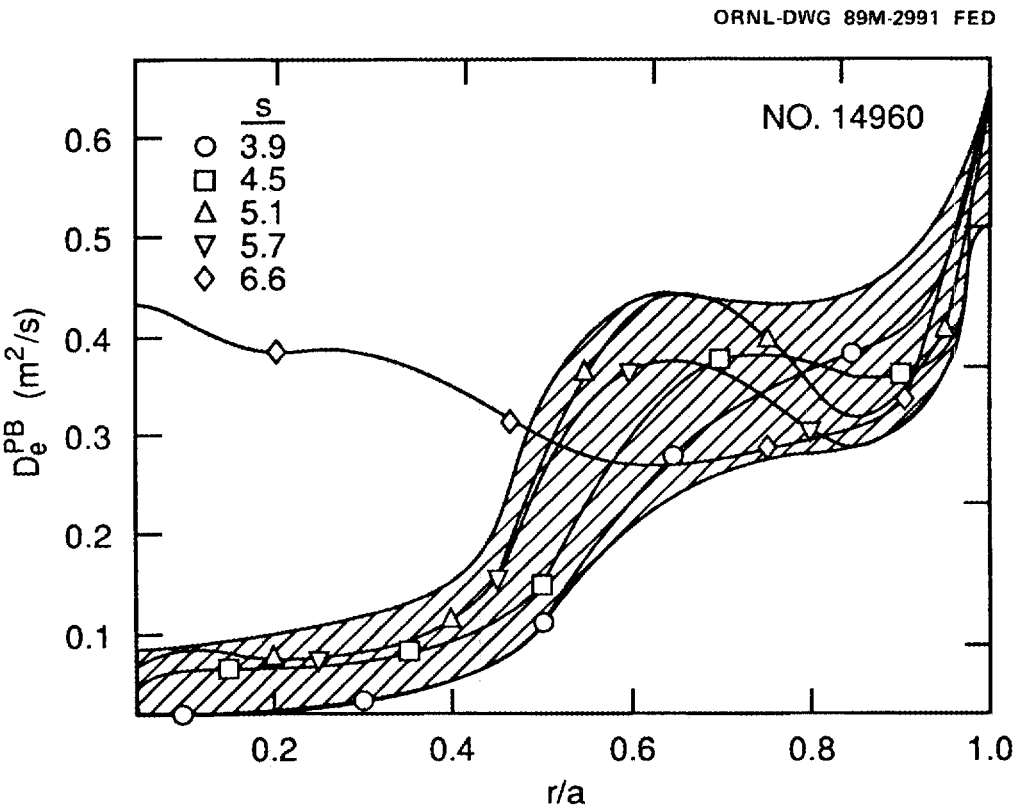

Fig. 5.5 Results of a particle balance calculation of the effective particle diffusivity in a multi-pellet fueled peaked density profile discharge. ICRF heating (5.5 MW) and NBI heating (4 MW) start at 6.0 s.

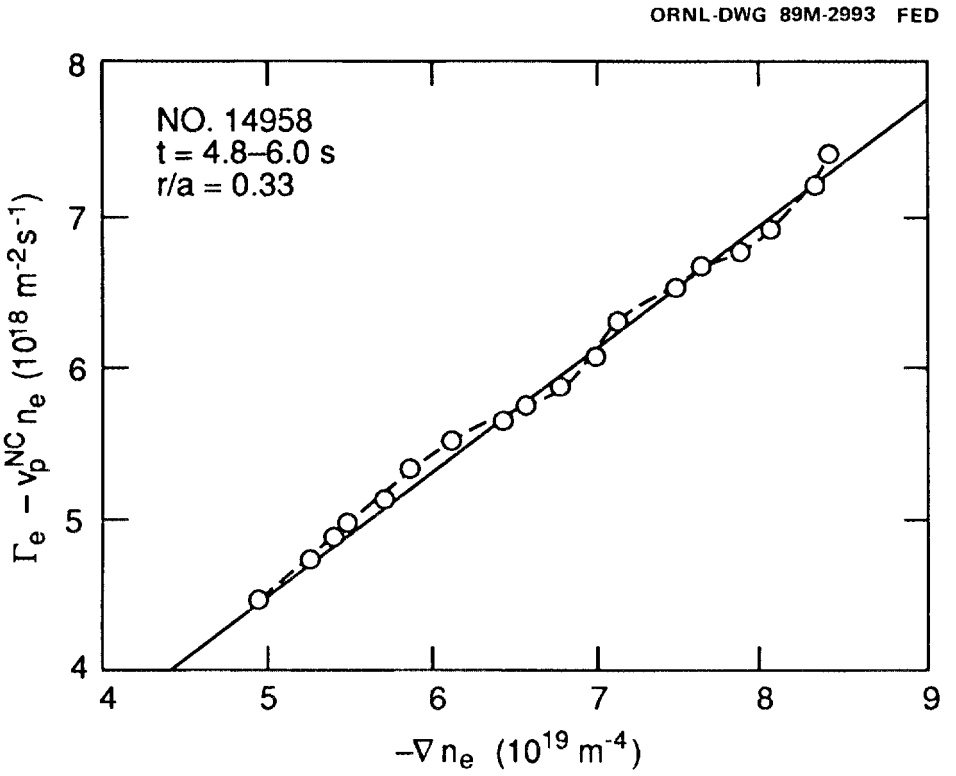

Fig. 5.6 Plot of diffusive particle flux as a function of density gradient during ohmic heating decay of a peaked density profile. A best fit slope gives $D^{eff}(r/a = 0.3) = 0.08$. The density peaking factor $[n_e(0)/\langle n_e \rangle]$ varies from 2.7 to 2.3 during this period of the density decay. The neoclassical flux ($v_p^{NC} n_e$) is approximately 25% of the total flux at this radius during this period.

The energy balance calculation of the electron heat flux is also performed in QFLUX. The heat flux is calculated from the energy balance equation,

$$\frac{3}{2}\frac{\partial}{\partial t}(n_e T_e) = P_e^{OH} + P_e^{ICRF} + P_e^{NBI} - P_e^{e-i} - P_e^{RAD} - \nabla \cdot q_e \,, \tag{5.7}$$

where the total heat flux is split into a conductive part and a convective part,

$$q_e = q_e^{cd} + q_e^{cv}. \tag{5.8}$$

The convective part is simply the kinetic energy carried by the net particle flux, given by $\frac{5}{2}\, T_e\, \Gamma_e$. The conductive heat flux is generally written as

$$q_e^{cd} = -n_e \chi_e \nabla T_e - q_e^{pinch}. \tag{5.9}$$

In calculations presented here, the term for the heat pinch q_e^{pinch} in Eq. (5.9) is ignored, although it should be noted that heat pulse propagation studies have given evidence for an existing heat pinch. In actual practice, the heat flux is calculated from the energy balance by volume integrating the energy sources and sinks and dividing by the flux surface area as was done for the particle flux in Eq. (5.1). The electron heat diffusivity χ_e is then computed as the particle diffusivity is in Eq. (5.6). There is more uncertainty in calculating the heat diffusivity, χ_e, than the particle diffusivity, however, primarily because of the uncertainty in power deposition calculations.

5.2 Particle Transport Modeling

An interpretive particle transport analysis code (PTRANS) has been developed by the author at JET to model the particle transport in pellet fueled plasmas. The code is used to model the electron density evolution for different transport

coefficients in JET pellet fueled plasmas to determine which transport models duplicate the experimental results. The PTRANS code can be similarly used for any tokamak experiment. In this section we describe the code and discuss the results of its use in determining transport coefficients for different types of pellet fueled discharges.

The motivation for developing this code has been the multiple deuterium pellet injection experiments on JET [41]. These experiments have produced dense plasmas with a variety of density profiles under various machine conditions. Some of these density profiles are dramatically more peaked than before pellet injection, as shown in Fig. 3.8, and can persist for several seconds. These pellet fueled plasmas are particularly well suited to the study of particle transport because of the readily measured changing densities produced with relatively small dependence on external sources. These plasmas are of interest because of their high density, peaked profile, and long density decay times that change with auxiliary heating.

PTRANS is a $1\,^1/_2$–D (non-circular geometry) radial transport code that calculates the evolution of density by solving the continuity equation for up to 32 particle flux models independently and in parallel. The magnetic surface geometry used in PTRANS is the same as that used in QFLUX, as described in Sect. 5.1. The particle flux models in PTRANS have individually specified particle transport coefficients that may include neoclassical contributions as well as anomalous contributions. The particle sources are determined by an external neutral deposition calculation (QFLUX) and neutral beam deposition calculation (PENCIL). The magnitude of the edge particle source is adjusted based on the global $Z_{\rm eff}$ measurement to account for the influx of impurities. Specifically, a ratio of carbon to oxygen of 3:1 is assumed from spectroscopic measurements, and the impurity influx is assumed to be proportional to the the global $Z_{\rm eff}$ mea-

surement. The number of electrons from the impurity influx is then added to the neutral particle source. Optional source feedback is built into the code, and can adjust the magnitude of the edge source profile for each model to keep the total number of particles in the plasma the same as that determined from experimental density profiles. This is used in ICRF heated plasmas when the RF power is initially turned on since the D_α detectors used to measure the source magnitude are located away from the antennas (see Fig. 2.2) and do not see the particle source from the antennas until a particle confinement time later.

5.2.1 Theoretical foundation

In this section we describe the theoretical background behind the PTRANS code that is used to model the density evolution. We start with the full kinetic Fokker-Planck equation for species a given in terms of the distribution function $f_a(\vec{r}, \vec{v}, t)$,

$$\frac{\partial f_a}{\partial t} + \vec{v} \cdot \frac{\partial f_a}{\partial r} + \frac{e_a}{m_a}(\vec{\mathrm{E}} + \vec{v} \times \vec{\mathrm{B}}) \cdot \frac{\partial f}{\partial v} = c_{na} + s_{na}, \tag{5.10}$$

where c_{na} is the Coulomb collision operator and s_{na} is an external source term. Following Ref. [45], we take the zeroth velocity moment of the Fokker-Planck equation and obtain the law of particle conservation for species a,

$$\partial n_a / \partial t + \vec{\nabla} \cdot (n_a \vec{u}_a) = s_{na}, \tag{5.11}$$

where $n_a = \int d^3v\, f_a$ is the density, $\vec{u}_a$ is the flow velocity, and $s_{na} = \int d^3v\, s_a$ are particle sources (due to ionization, recombination, charge exchange, etc.). The collision term of the kinetic equation integrated over all velocity space is zero since the number of particles is conserved in collisions. Integrating this equation

over the region interior to a surface of constant magnetic flux ϕ (or ρ = const) and using the divergence theorem, we have

$$\int d^3x \frac{\partial n_a}{\partial t} + \oint \frac{dS}{|\nabla\phi|} \vec{\nabla}\phi \cdot (n_a \vec{u}_a) = \int d^3x \, s_{na}, \tag{5.12}$$

where dS is the area element on the flux surface ϕ. This can be rewritten by taking the time derivative at constant x as

$$\frac{\partial}{\partial t} \int d^3x \, n_a + \oint \frac{dS}{|\nabla\phi|} n_a (\vec{u}_a - \vec{u}_\rho) \cdot \vec{\nabla}\phi = \int d^3x \, s_{na}, \tag{5.13}$$

where $\vec{u}_\rho$ is the flux surface velocity. By using the definition of flux surface average,

$$\langle n_a \rangle \equiv \int_{\Delta V} d^3x \, n_a \Big/ \int_{\Delta V} d^3x = (d\phi/dV) \int \frac{dS}{|\nabla\phi|} n_a, \tag{5.14}$$

and differentiating with respect to ρ, we can rewrite Eq. (5.11) as

$$\frac{\partial}{\partial t}\Big[V'(\rho)\langle n_a \rangle\Big] + \frac{\partial}{\partial \rho} V'(\rho) \big\langle n_a (\vec{u}_a - \vec{u}_\rho) \cdot \vec{\nabla}\rho \big\rangle = V'(\rho) \langle s_{na} \rangle, \tag{5.15}$$

where $V'(\rho) \equiv \partial V/\partial\rho$ and $\int d^3x \, n_a = \int_0^\rho d\rho \, V'(\rho) \langle n_a \rangle$. Thus the surface-averaged particle density satisfies a continuity equation in which the effective particle flux, relative to the surface, is defined by

$$\frac{\big\langle n_a (\vec{u}_a - \vec{u}_\rho) \cdot \vec{\nabla}\rho \big\rangle}{\big\langle |\nabla\rho| \big\rangle} \equiv \Gamma_a. \tag{5.16}$$

The denominator in Eq. (5.16) ensures that the particle flux has dimensions of particles per area per second, independent of the definition of ρ. If we ignore

the motion of magnetic surfaces ($\vec{u}_\rho \simeq 0$) and assume that the density and particle source are approximately uniform on the surface ($\langle n \rangle \simeq n$), the continuity equation may be written as

$$\frac{\partial n_a(\rho,t)}{\partial t} + \frac{1}{V'(\rho,t)}\frac{\partial}{\partial \rho}\left[V'(\rho,t)\langle|\nabla\rho|\rangle\Gamma_a(\rho,t)\right] - s_{na}(\rho,t) = 0. \tag{5.17}$$

It is worth noting that in the large-aspect-ratio circular-cross-section case, where $V' \propto \rho \simeq r$, Eq. (5.17) takes the more familiar form in cylindrical coordinates

$$\frac{\partial n_a(r,t)}{\partial t} + \frac{1}{r}\frac{\partial}{\partial r} r\,\Gamma_a(r,t) - s_{na}(r,t) = 0. \tag{5.18}$$

The particle flux in the continuity equation is defined by

$$\Gamma = -\mathrm{D}(\rho,t)\frac{\partial n(\rho,t)}{\partial \rho}\langle|\nabla\rho|\rangle + n(\rho,t)v(\rho,t), \tag{5.19}$$

where the first term is the diffusive flux and the second is the convective flux. Both the diffusion coefficient $\mathrm{D}(\rho,t)$ and the convective velocity coefficient $v(\rho,t)$ may contain neoclassical and anomalous contributions:

$$\mathrm{D}(\rho,t) = \mathrm{D}^{\mathrm{NC}}(\rho,t) + \mathrm{D}^{\mathrm{AN}}(\rho,t) \qquad v(\rho,t) = v^{\mathrm{NC}}(\rho,t) + v^{\mathrm{AN}}(\rho,t)\,. \tag{5.20}$$

The neoclassical electron particle flux [46] is given by

$$\Gamma_{\mathrm{e}}^{\mathrm{NC}} = -\mathrm{D}_n^{\mathrm{NC}}\frac{\partial n_{\mathrm{e}}}{\partial \rho} - \mathrm{D}_T^{\mathrm{NC}}\frac{\partial T_{\mathrm{e}}}{\partial \rho} - W\,E_{\|}, \tag{5.21}$$

where the last term is the Ware pinch given in Eq. (4.39). The neoclassical contributions that we use here are:

$$\mathrm{D}^{\mathrm{NC}} = \mathrm{D}_n^{\mathrm{NC}} + \mathrm{D}_T^{\mathrm{NC}} \frac{\partial T_e}{\partial \rho} \Big/ \frac{\partial n_e}{\partial \rho},$$

$$v^{\mathrm{NC}} = W\, E_{\|}, \tag{5.22}$$

with the coefficients given in detail in Eq. (4.33).

5.2.2 Modeling results

The modeling of the electron density evolution has resulted in a better understanding of the possible transport coefficients needed to reproduce the anomalous particle transport behavior seen in JET. A general result that has come out of this analysis is that in both types of pellet fueled discharge studied, a large anomalous inward pinch velocity is not necessary in the inner half of the discharge to reproduce the density profile evolution. The modeling of the two types of pellet fueled discharge and comparison with existing transport models are discussed below.

In the multiple-pellet current-rise experiments it has been experimentally seen that pellet penetration to the magnetic axis or beyond has led to highly peaked profiles that are kept peaked by subsequent pellets that also reach the axis. By modeling the density evolution and using the measured pellet deposition (the density profile immediately after the pellet injection minus the pre-pellet density profile), we have been able to model the profile evolution by using the calculated Ware pinch velocity and an anomalous diffusivity of the form $\mathrm{D}^{\mathrm{AN}} = 0.08\,\mathrm{m}^2/\mathrm{s}$ inside $r/a = 0.4$, rising to $0.30\,\mathrm{m}^2/\mathrm{s}$ at $r/a = 0.6$ and increasing as $(r/a)^2$ at $r/a > 0.6$. This model, as shown in Fig. 5.7, reproduces the measured density evolution very well.

The same transport model can be used to effectively model the post-pellet decay after all the pellets are injected in the same experiment. This indicates

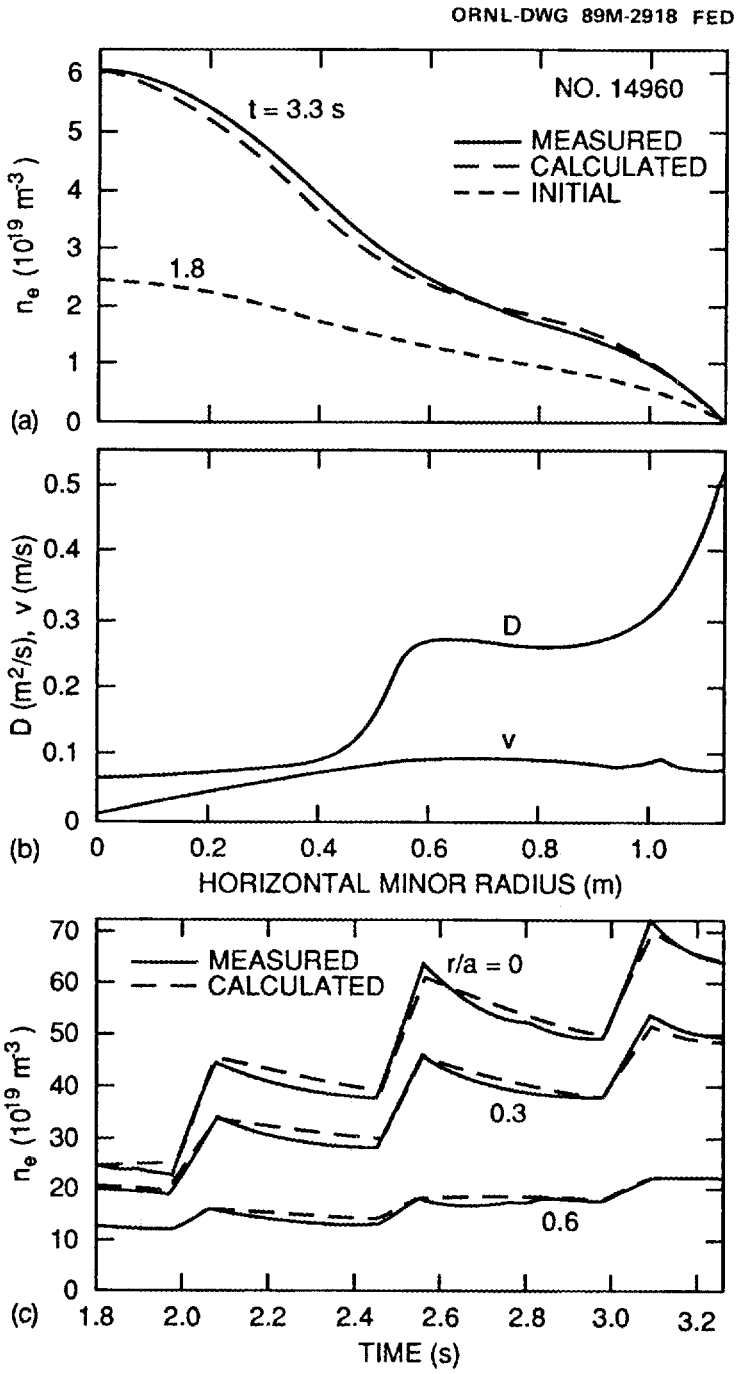

Fig. 5.7 Comparison of calculated and measured electron density evolution in a multi-pellet fueled discharge. The density profile (a), the transport coefficients (b), and temporal evolution of density (c) are shown during the ohmic heated current rise for a multiple 2.7 mm pellet fueled discharge.

that there is no dramatic change in particle transport in these discharges during pellet injection in the current rise and at the beginning of the flattop after the pellet injection has ceased. When strong auxiliary heating is applied to these discharges, there is seen an increase in MHD activity as measured by the magnetic loops and a subsequent flattening and broadening of the electron density profile. The source of electrons is increased both from direct neutral beam deposition and from increased influx from the wall, limiter, and ICRF antennas.

As a comparison, we have also modeled a non-pellet fueled discharge with the same conditions as the multi-pellet fueled case. In Fig. 5.8 we plot the output from the modeling code, which shows a diffusivity that is a factor of 2 higher in the core region of the plasma than the peaked profile case and has a similar rise in diffusivity at $r/a \simeq 0.5$ although not as pronounced. This calculation also does not use an anomalous inward pinch velocity as has been suggested by others [58]. It should be noted that it is possible to find a suitable diffusive model that yields a suitable density evolution with an anomalous inward pinch of the form $v_p^{\mathrm{AN}} \simeq (r/a)^2$, and therefore these empirical models for v_p cannot be excluded. The experimental uncertainty in the density profile, especially in the flat non-pellet or shallow pellet penetration cases, does not make it possible to say for sure whether or not an anomalous inward pinch is required to explain the data.

The period of the peaked density profile in sawtooth-free limiter discharges has been analyzed and the electron profile evolution modeled by the use of a neoclassical pinch velocity and a time-independent diffusion coefficient with a strong increase at the radial position of the density pedestal formation, as shown in Fig. 5.9. The diffusion model used is more than an order of magnitude larger than the neoclassical value, as shown in Fig. 5.10. This same transport model is found to be applicable in both ohmic and ICRF heated discharges, although the

ORNL-DWG 89M-2919 FED

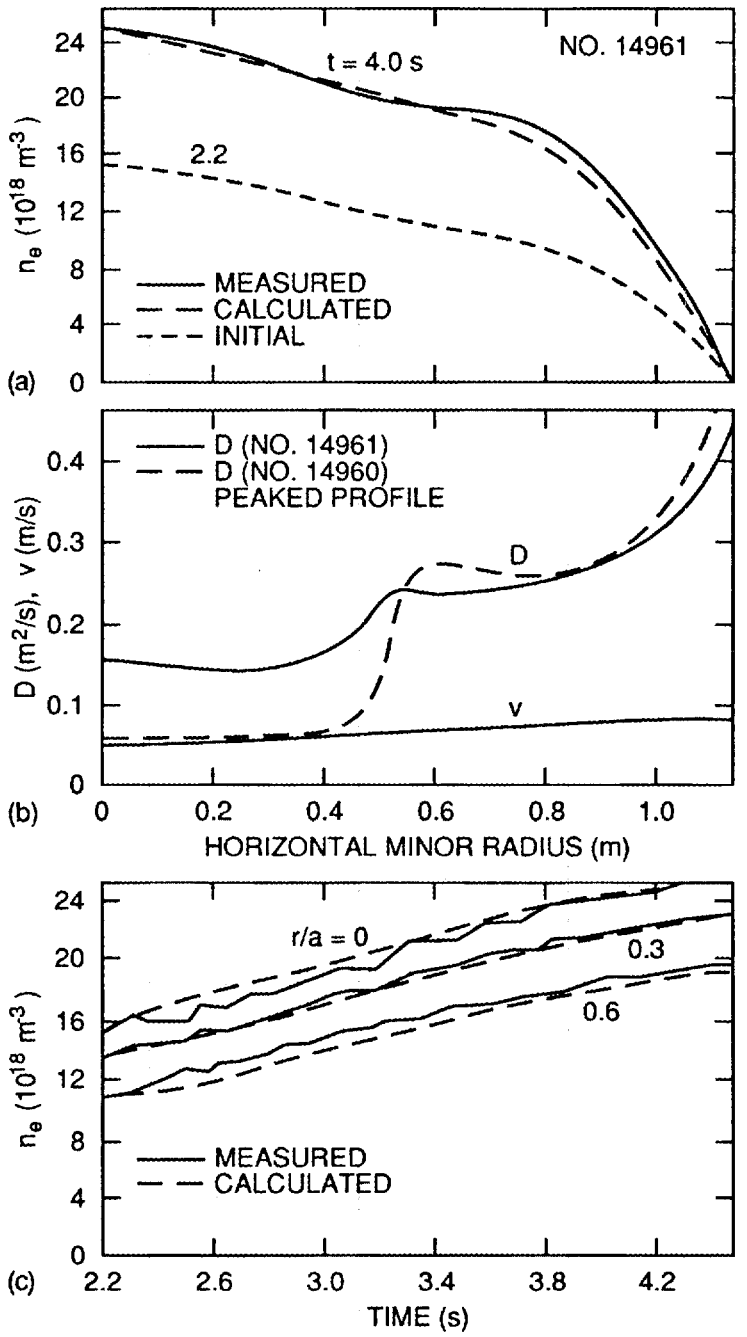

Fig. 5.8 Comparison of calculated and measured electron density evolution in a non-pellet fueled discharge. (a) Density profile both initial and final. (b) Transport coefficients with comparison of D for peaked density discharge. (c) Density evolution at three radii.

ORNL-DWG 89M-2920 FED

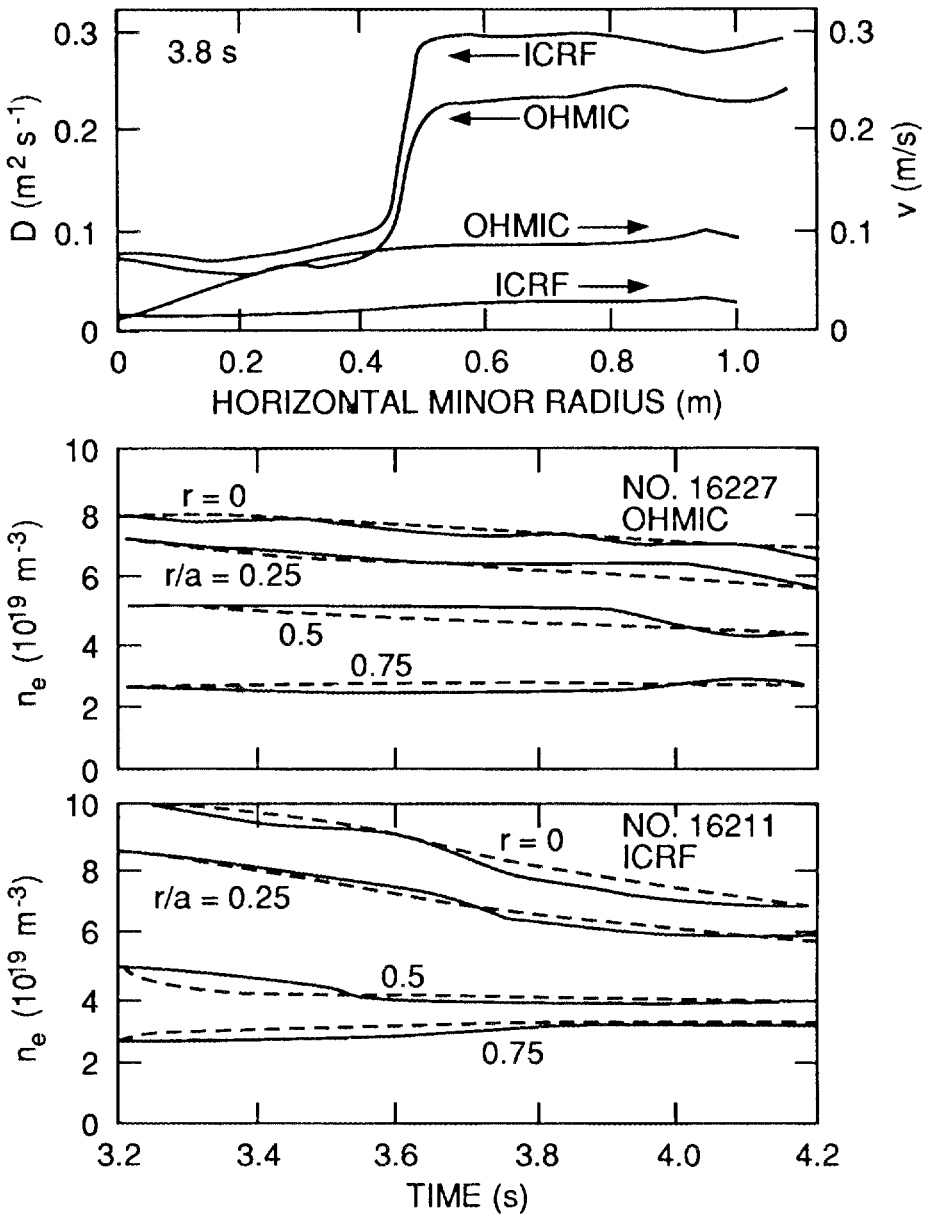

Fig. 5.9 Particle diffusion coefficient for ohmic and ICRF heated discharges. Evolution of density profile, measured (solid curves), at four radii during the density decay following pellet injection.

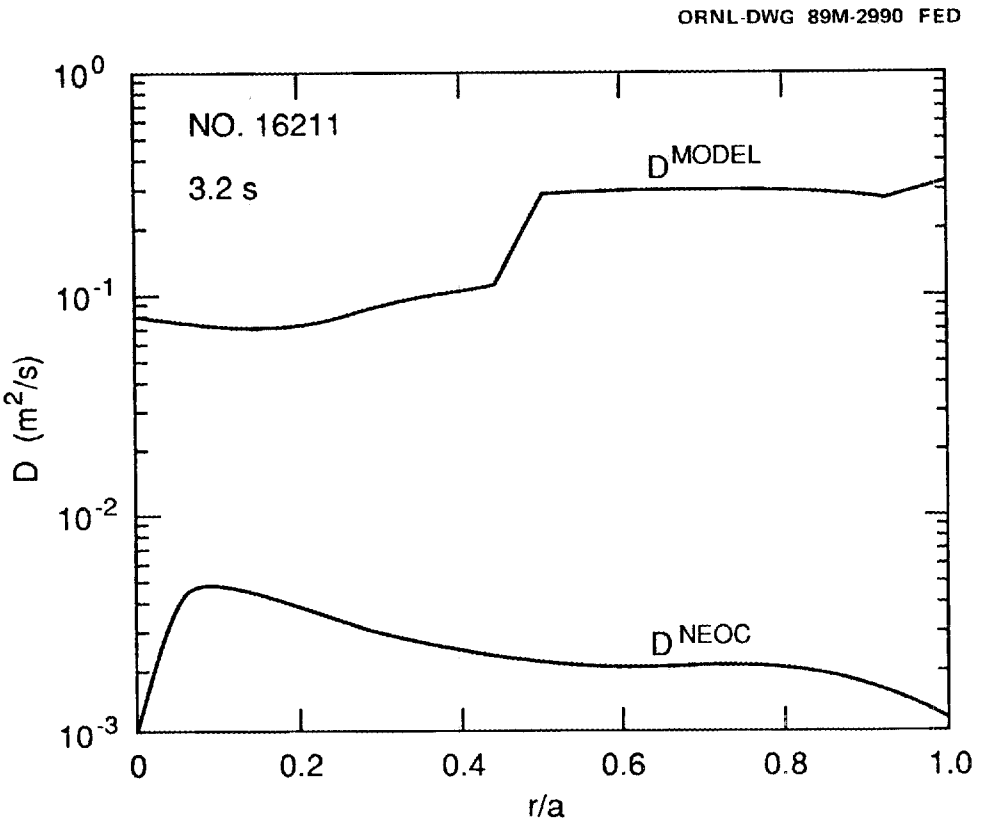

Fig. 5.10 Comparison of the determined effective diffusion coefficient with the calculated neoclassical diffusion coefficient.

heated case shows slightly higher central diffusivity. Calculations of the density evolution using the $(r/a)^2$-dependent diffusion coefficient suggested by Hulse [59] for TFTR ohmic pellet fueled discharges do not yield the observed density pedestal on the outer portion of the minor radius.

In discharges where a strongly peaked electron density profile rapidly redistributes to a flat profile and low levels of low wavenumber spectrum MHD activity are present (as described in Sect. 3.4), the diffusion coefficient can be modeled as a function of local electron temperature. In these cases, the central diffusivity rapidly evolves from the ohmic post-pellet case [$D(0) \sim 0.1\,m^2/s$] to a diffusion coefficient profile which is more nearly flat as shown in Fig. 5.11 [$D(0) \sim 0.3\,m^2/s$]. This temperature-dependent modeling of the diffusivity gives an increase in central diffusivity of a factor of $\sim$ 3 in going from a central temperature of $\sim$ 2 keV to $\sim$ 8 keV which is a much stronger temperature dependence than suggested in previous work at JET [60]. This rapid change in diffusivity suggests the presence of another mechanism in these discharges that further accelerates the central electron density decay. In a discharge where a clear transition from the ohmic-like transport to one in which central MHD activity is seen from soft X-rays, the profile evolution can be modeled by a transition from the ohmic-like diffusion to the temperature-dependent diffusion. The diffusion coefficients determined from particle balance calculations of the electron flux agree well with the best-case diffusive models used in the discharges that have been modeled. The discharges that can be modeled with temperature-dependent diffusivity also show similar increases in diffusion coefficient from particle balance calculations.

A comparison of measured profile evolutions and calculations using the two types of diffusivity model for the two different types of discharge is shown in

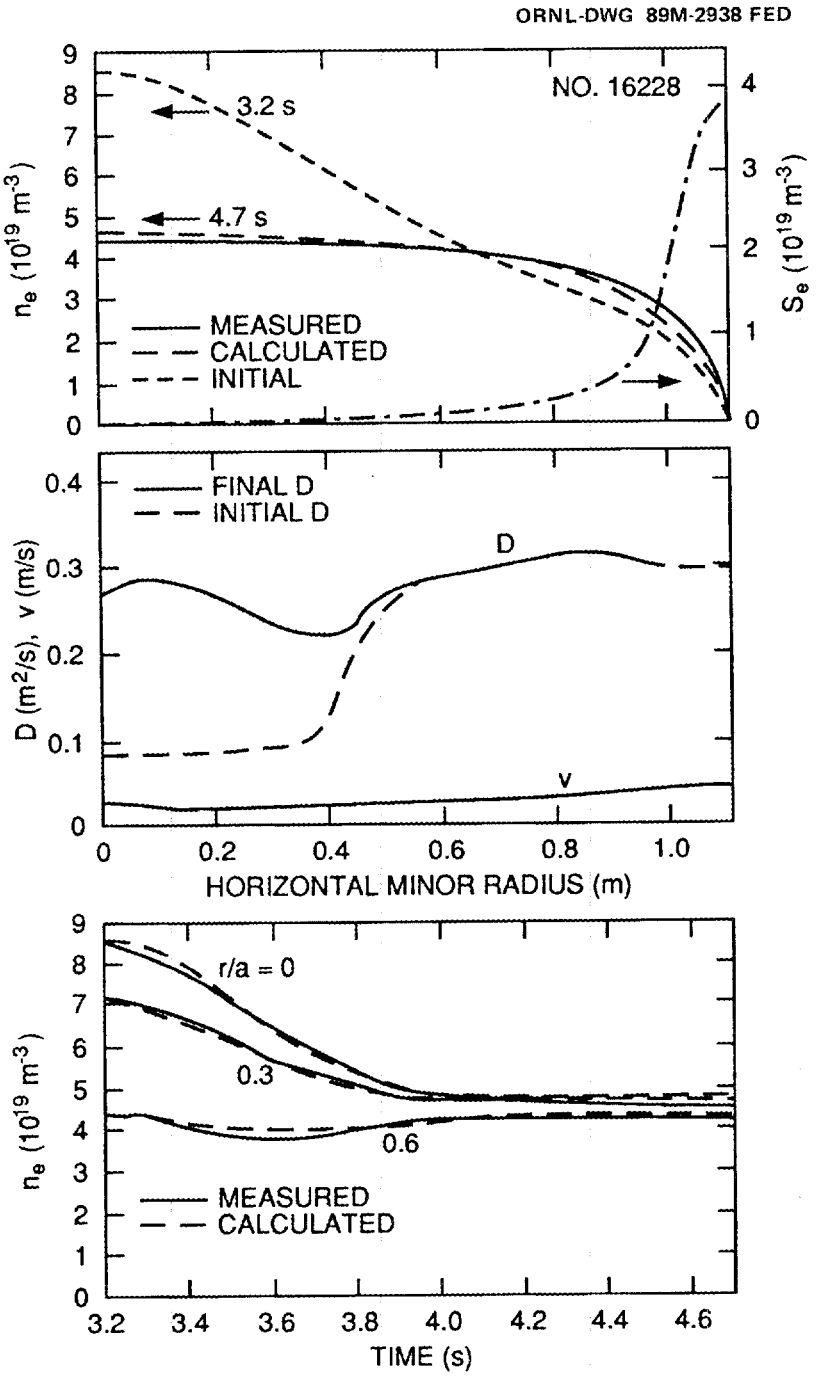

Fig. 5.11 Comparison of measured and calculated density evolution using a temperature-dependent diffusion coefficient and neoclassical pinch. This discharge No. 16228 exhibited enhanced levels of MHD activity as shown in Fig. 3.13. The diffusivity is given by D=D(ohmic case) $\left[1 + T_e(\mathrm{eV})^{1.3}/40000\right]$.

three-dimensional plots of the density evolution in Fig. 5.12. We see that there is good qualitative agreement between the measured and calculated density profile evolutions in both the slow ohmic density decay (No. 14960) and in the rapid density decay with a temperature-dependent diffusivity that characteristically shows enhanced MHD activity (No. 16228).

The PTRANS code, with its simultaneous calculation of up to 32 transport models, makes it possible to carry out a sensitivity study of the transport coefficients used in the models. This has been done for a number of discharges and has led to results typical of those shown in Fig. 5.13 for a peaked density profile decay. We see that the core region of the discharge is sensitive to variations of the diffusivity of the order of $\pm 20\%$. The outer region of the discharge is not as sensitive due to the strong edge source. This leads to generally larger error bars ($\pm 30\%$) on the outer half of the diffusivity profile than on the inner half ($\pm 15\%$), even taking into account the uncertainty in the measured density profile.

A large number of empirical particle transport models developed from other tokamak experiments have been used to calculate the electron density profile evolution in a variety of JET pellet fueled discharges. Among these models are three which assume an inward-directed anomalous pinch velocity. A model used by the TFR group [19] to model pellet injection data uses a diffusivity and an inward velocity that are given, respectively, by

$$\mathrm{D} = \mathrm{D}^{\mathrm{NC}} + \frac{5\,\mathrm{D}_A\,\mathrm{D}_B}{\mathrm{D}_A + 5\,\mathrm{D}_B}, \qquad v = 0.24\,\frac{r}{a} \quad (\mathrm{m/s}), \tag{5.23}$$

where

$$\mathrm{D}_A = \frac{6 \times 10^{20}}{n_e(r)\,q(r)\,T_e(r)^{3/4}}, \tag{5.24}$$

ORNL-DWG 89-2989 FED

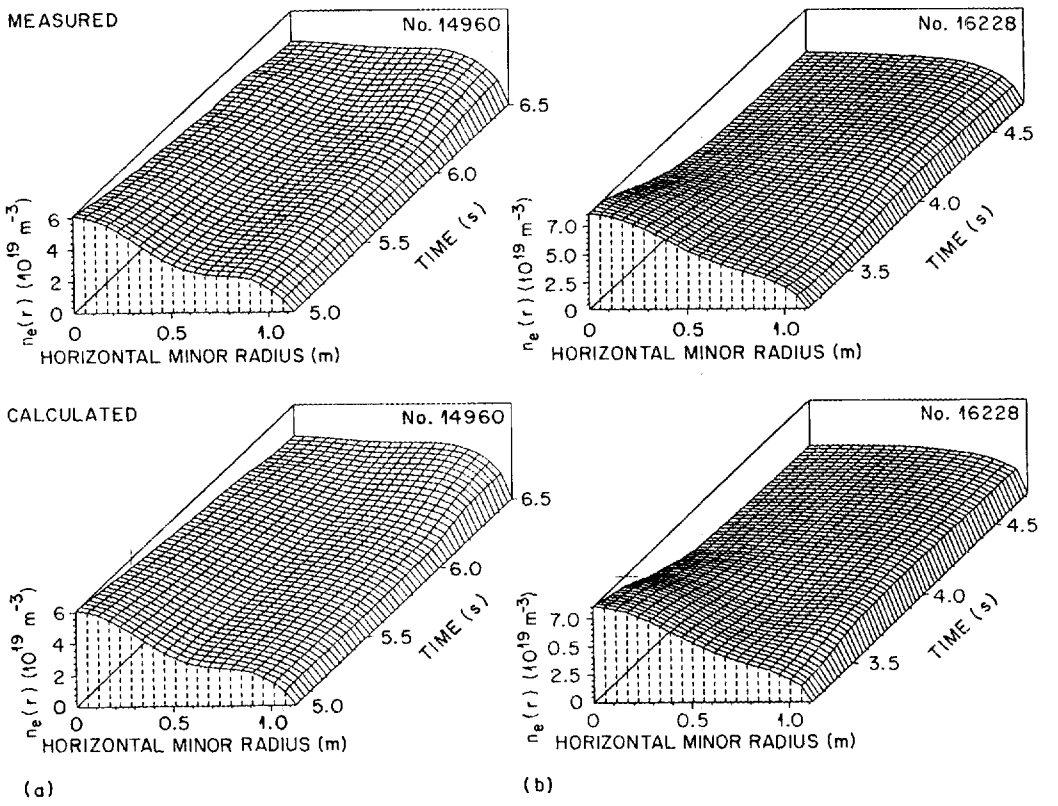

Fig. 5.12 Comparison of measured and calculated density profile evolutions for ohmic and ICRF heated discharges. The diffusion coefficient is modeled as an increasing function of temperature in the heated discharge (No. 16228).

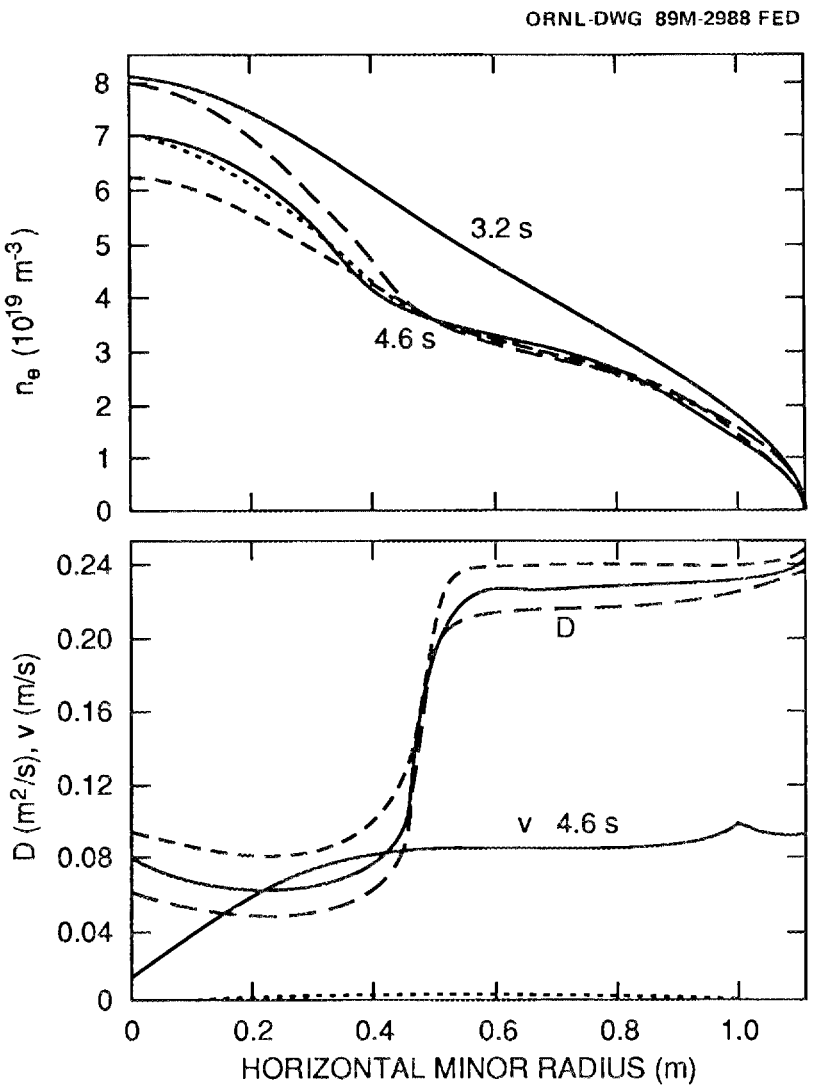

Fig. 5.13 Density profile evolution calculation sensitivity to variations in diffusivity magnitude. The variation shown for a peaked density profile with ohmic decay is ±20% in the core region. Large variations are seen in the core density but not in the density in the outer half of the minor radius.

and

$$\mathrm{D}_B = \frac{T_e}{16\, e\, B}\,, \tag{5.25}$$

which is the Bohm diffusivity with n_e in m^{-3}, T_e in eV, and B in T. q is the safety factor and D^{NC} is the neoclassical diffusion coefficient. Another model that is commonly used in predictive studies that has been developed from Alcator-C results [61] gives an inverse density dependence to $\mathrm{D}(r)$. This model uses $\mathrm{D} = [n_e(\mathrm{m}^{-3})/10^{19}]^{-1}$ and $\mathrm{v} = -2\,\mathrm{D}\,r/a^2$. A third model developed by Coppi and Sharky [62] to explain high-density discharges in Alcator-C and FT uses a model in which the diffusivity and inward velocity are given, respectively, by

$$\mathrm{D} = \epsilon_p \frac{c^2}{\omega_{\mathrm{pe}}^2} \Omega_{\theta e} \frac{a\, 3\, q_0}{r\, 4\, q_s} \frac{\epsilon_d \Upsilon_c}{8\pi\, \alpha_{\mathrm{D}}},$$

$$\mathrm{v} = 2\,\mathrm{D}\,\frac{r}{a^2}\,\alpha_p, \tag{5.26}$$

where $\Upsilon_c \cong 3.6(n_e Z_{\mathrm{eff}}^2/A_i)^{1/5}$, $\alpha_p = 4\left(\nu_e^{**}\right)^{0.5}$, where ν_e^{**} is the collisionality parameter for untrapped particles, ω_{pe} is the electron plasma frequency, $\Omega_{\theta e}$ is the poloidal electron gyrofrequency, and α_D is a weak function of r/a which is close to unity. ϵ_p and ϵ_d are constants with values of 1 and 0.4.

The results of calculations using these three models applied to JET data are shown in Fig. 5.14 for a typical pellet fueled discharge with partial pellet penetration followed by 4 MW of ICRF heating. These models typically yield peaked density profiles when the measured profile is seen to remain essentially flat in the center. This density peaking calculated from these transport models comes from the strong anomalous inward velocity and the large edge and low central diffusivities. The diffusivity in the Coppi-Sharky model was even lowered by a factor of 5 to give closer agreement to the measured profiles. The poor

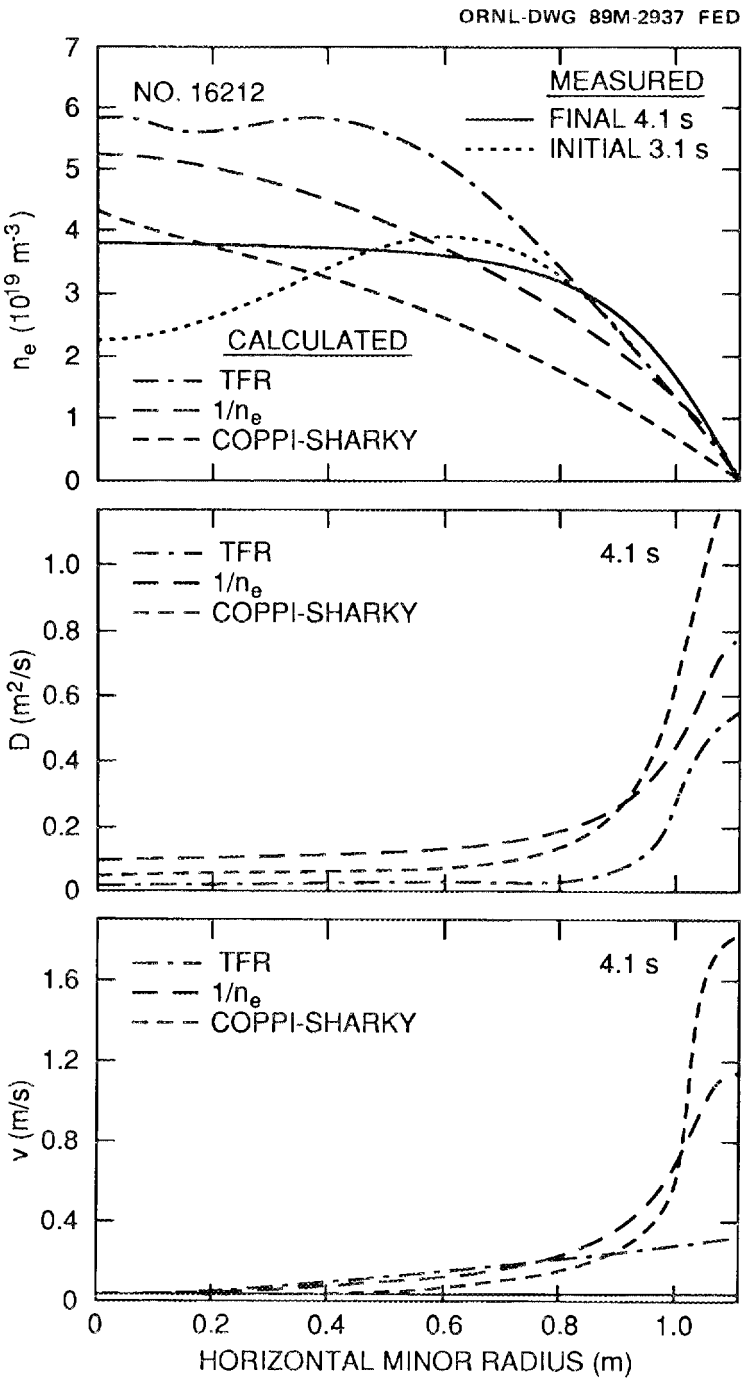

Fig. 5.14 Comparison of density profile evolution for three empirical particle transport models. A 4 mm pellet is injected at 3 s with penetration to 0.3 m minor radius. The models used are (1) TFR [19], (2) $1/n_e$ dependence [61], and (3) from Coppi-Sharky [62] lowered by a factor of 5.

agreement of the density evolution from these models with the actual density evolution suggests that these and similar models with strong edge diffusivity and anomalous inward velocities are not appropriate for high temperature tokamak plasmas in large machines like JET. The higher temperature (and hence lower collisionality) plasmas in JET, as compared with earlier smaller tokamaks, may be responsible for the different particle transport seen in these JET pellet fueling experiments. Predictive modeling of particle transport in future tokamaks using these transport models may not yield very accurate results if the plasma behavior in JET scales to future devices.

The hypothesis that there exists an inward thermal pinch effect has been used to explain particle transport in various tokamaks such as Alcator-C [63]. Using the phenomenological transport relations proposed by O'Rourke [63], we have attempted to model the density evolution assuming that there is an inward-directed pinch velocity proportional to $\nabla T_e/T_e = L_{T_e}^{-1}$ and a temperature-dependent diffusion coefficient such that the particle flux is given by

$$\Gamma_e = \alpha \frac{\nabla T_e}{T_e} - \mathrm{D}(T_e)\,\nabla n_e + v^{\mathrm{NC}}\, n_e. \tag{5.27}$$

The results of modeling the density profile evolution of discharges with peaked density profiles during high-power auxiliary heating has shown that a strong inward thermal pinch does not reproduce the measured density evolution even with a temperature-dependent diffusion coefficient such that $\mathrm{D}(r = 0)$ evolves from $\sim 0.1\,\mathrm{m}^2/\mathrm{s}$ to $\sim 0.4\,\mathrm{m}^2/\mathrm{s}$. The resultant profiles from these calculations do not lead to as much central density peaking as measured due to an off-axis maximum in $\nabla T_e/T_e$ at $r/a \sim 0.3$. Only with an inward thermal pinch with a magnitude on the order of the neoclassical inward pinch is the density evolution modeled well for the discharges which show strong central density decay.

In analysis of Alcator-C pellet injection results, Foord [64] proposed using the spatial and temporal forms for D and v of

$$\mathrm{D}(r,t) = \mathrm{D}_0 \qquad\qquad v(r,t) = v_0 \frac{r}{a}. \tag{5.28}$$

He was able to apply these results analytically and come up with a best fit for D_0 and v_0 for a given discharge. An attempt to model the JET data with this same parameterization for D and v was made, and it was found that it is not possible to reproduce the density evolution for a reasonable range of D_0 and v_0 in any of the discharges studied. This parameterization typically leads to parabolic profiles and does not lead to the peaked profile on an outer density pedestal. It seems that the highly anomalous inward pinch hypothesized in this model and predicted theoretically [65] is not needed to explain the JET data.

From the neoclassical theory discussed in Chapter 4 we would expect impurity density profiles to be highly peaked on axis whenever the electron density profile is peaked. Examples of experimental evidence for impurity accumulation were shown in Sect. 3.5. Behringer et al. [66] have examined the transport of impurities in these pellet fueled peaked density profile discharges with suppressed sawteeth. For high-Z impurities (namely Ni), the impurity ions are in the *Pfirsch-Schlüter* regime at the plasma periphery and are in the *plateau* regime in the plasma interior. In the interior, then, the ion temperature gradients are expected to lead to moderate inward driving forces. Their analysis used an anomalous diffusion coefficient that drops to a low value in the plasma core region during the peaked profile period. In the simulations, the anomalous diffusivity was reduced to $0.001\,\mathrm{m}^2/\mathrm{s}$ in the core region ($r < a/2$ initially, shrinking to $r = 0$) and was $1\,\mathrm{m}^2/\mathrm{s}$ in the region outside the core. Their results show good agreement with the measured soft X-ray profiles and impurity line radiation. The anomalous transport

coefficient used in their work correlates well with the anomalous electron diffusivity reported here. The primary difference is the shifting inward of the reduced diffusivity region with time. It is interesting to note that no anomalous inward velocity was assumed in their analysis, as is the case in the electron transport analysis here. It is also interesting to note that the neoclassical theoretical ∇T_i convective velocity is experimentally confirmed by the impurity behavior during the later phases of these heated plasmas.

5.3 Particle Transport Scaling

The scaling of transport coefficients with plasma parameters is of importance in predicting performance of future experiments and in extrapolating JET results to other tokamaks. A relatively small window of parameter space was used in these pellet fueling experiments, and therefore a complete investigation of transport scaling with all relevant parameters is not possible. Previous work by others [60] has shown weak scaling of global particle diffusion with plasma current. The higher currents in JET lead to different profile shapes (more peaked) and higher temperatures, and these may be the underlying causes that affect the transport. Sawteeth have also been shown to affect the transport in the core of the discharge, and for this reason we will concentrate on sawtooth-free discharges. It has been determined by others [60] that sawtoothing in the flattop of the discharge enhances the effective central particle diffusivity to values greater than the 0.4 m^2/s determined here.

The magnitude of central diffusion is found to be a function of the electron density profile peaking, as shown in Fig. 5.15. By using the particle balance diffusivity calculated, as described in Sect. 5.1, we can compare the diffusivity near the center of the discharge ($r/a = 0.3$) with the density peaking factor

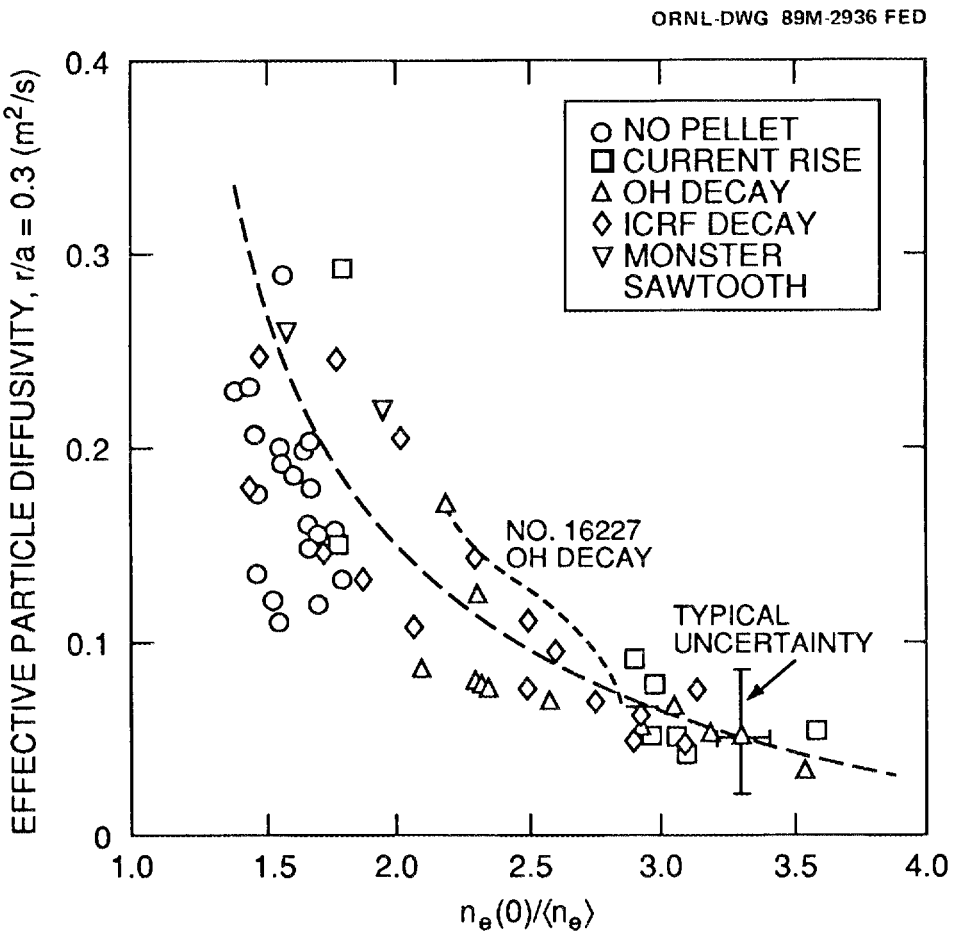

Fig. 5.15 Effective particle diffusivity (electron) at $r/a = 0.3$ as a function of density profile peakedness. The particle diffusivity is derived from a particle balance calculation assuming no anomalous inward particle convection. Values are averaged over 400 ms during a discharge, and each point represents a different discharge. The time history of ohmic discharge No. 16227 is shown on the same plot.

$[n_e(0)/\langle n_e \rangle]$. We see that for discharges where there is strong peaking, the diffusivity is much lower than for cases with no peaking. The data shown are limited to times early in the discharge before sawteeth appear. It is also seen that even in discharges where pellet injection with partial pellet penetration does not lead to increases in the density profile peakedness, the particle diffusivity in the core of the discharge is still of the same range as the non-pellet fueled case. The minimum central effective particle diffusivity seen is on the order of 0.04 m^2/s. This is found in discharges where the peaking factor is on the order of 3.5 for more than 400 ms.

As a check that the diffusivity is not simply an inverse function of density, we plot the diffusivity as a function of both local density and volume-averaged density in Fig. 5.16. We see from these plots that there is no clear dependence of diffusivity on density; clearly, it does not follow the proposed Alcator scaling of $D \sim 1/n_e$. The implication of the diffusion scaling with density peakedness is that peaked profiles should tend to remain peaked for a reasonable length of time due to the reduced central diffusivity compared to the nonpeaked case. This is in fact what is observed. When the peaked profile is ohmically heated, it can be seen to persist for more than 2 s, which implies central particle confinement times of that order. Only when auxiliary heating is applied that leads to possible temperature-dependent MHD disturbances do we see a rapid decrease in the central density. In these cases the density peaking factor can be seen to drop from 2.8 to 1.8 in only 200 ms.

It is also interesting to compare this diffusivity scaling with the scaling of density peakedness from pellet penetration, shown in Fig. 3.5. The two results when taken together suggest that the electron particle diffusivity should be a function of pellet penetration. One would expect that pellets with central penetration,

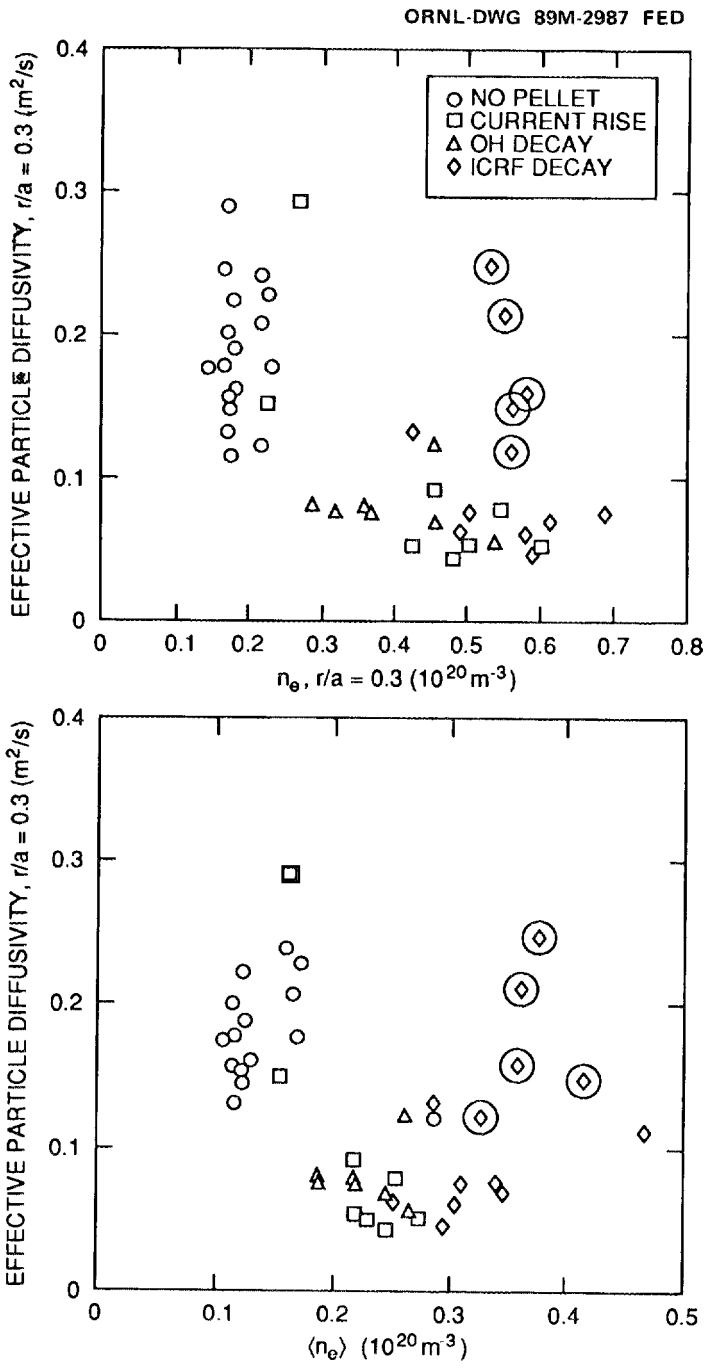

Fig. 5.16 Effective particle diffusivity (electron) at $r/a = 0.3$ plotted as a function of local density and volume-averaged density. Values are averaged over 400 ms during a discharge.

which generate peaked density profiles, would lead to plasmas with lower central particle diffusivity than plasmas that have partial pellet penetration and no significant increase in density profile peakedness. Except when the peaked density profile decays quickly due to perhaps an internal MHD instability as discussed in Sect. 3.4, the peaked density remains for over 1.5 s and the central diffusivity remains low until the peaked profile has dissipated.

We have also examined the diffusivity in the same data set to look for any kind of temperature dependence. When the particle balance diffusivity is plotted as a function of local electron temperature, as in Fig. 5.17, we see no trend for the diffusivity to increase with temperature except in the discharges that show the enhanced MHD activity (marked within circles in the figure) during the auxiliary heating phase of the discharge. These discharges show a larger diffusivity by a factor of ~2–3 at temperatures above 4 keV than the discharges with low MHD activity. Even the low-temperature discharges with enhanced MHD activity above the nominal ohmic value show a larger diffusivity than the low MHD level cases.

It is also possible to compare the determined diffusivities with the locally determined parameter $\eta_e = \frac{n/\nabla n}{T/\nabla T}$, which is the ratio of density scale length to temperature scale length. It is assumed that the value of η_i is somewhat similar to η_e. Figure 5.18 shows a plot of diffusivity versus η_e, and one can see generally a linear trend of higher diffusivities with values of η_e up to ~ 2. The data show a tendency to perhaps saturate at diffusivities on the order of $0.24\,\mathrm{m}^2/\mathrm{s}$ as η_e goes above ~ 2. This may indicate an actual saturation in the turbulence generated by η_i modes in the plasma, or it may just be related to the experimental uncertainty associated with the η_e parameter.

In addition to the scaling for the particle diffusivity, we have calculated the local effective electron thermal diffusivity for the same discharges using the interpretive transport code QFLUX as described in Sect. 5.1. There is much more

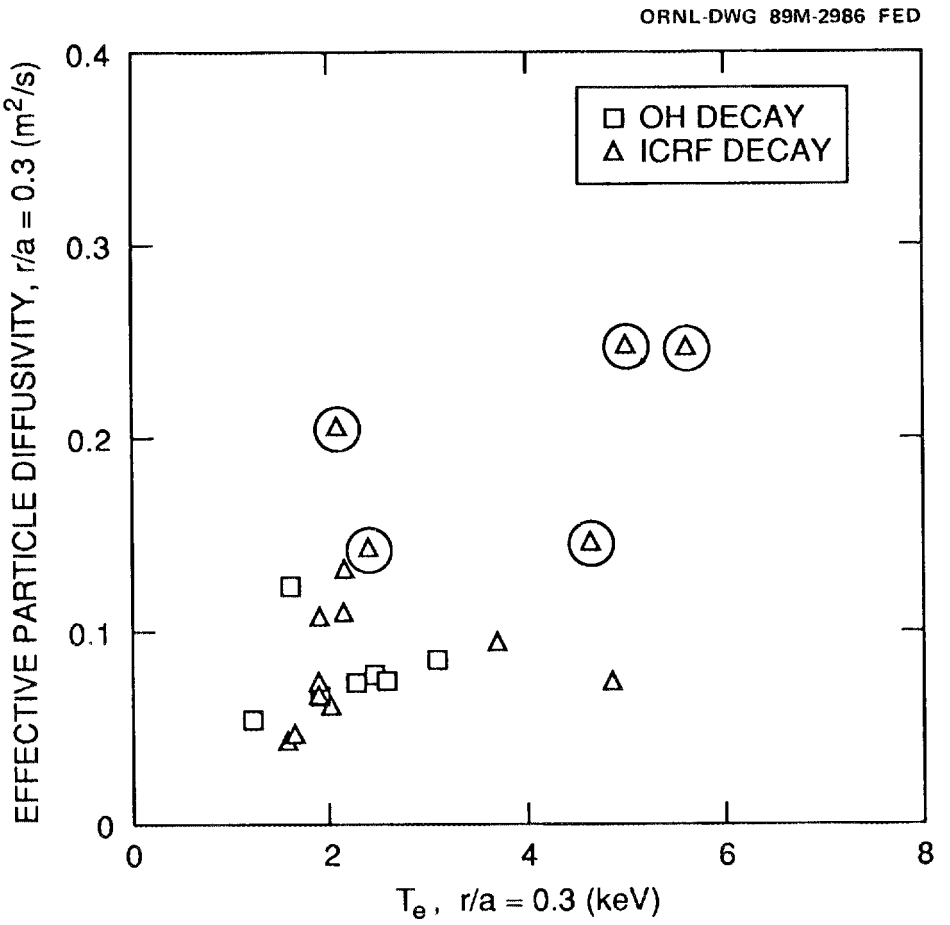

Fig. 5.17 Effective particle diffusivity (electron) at $r/a = 0.3$ as a function of local electron temperature. The circled data points are from discharges with enhanced levels of MHD activity measured at the plasma edge. Values are averaged over 400 ms during a discharge.

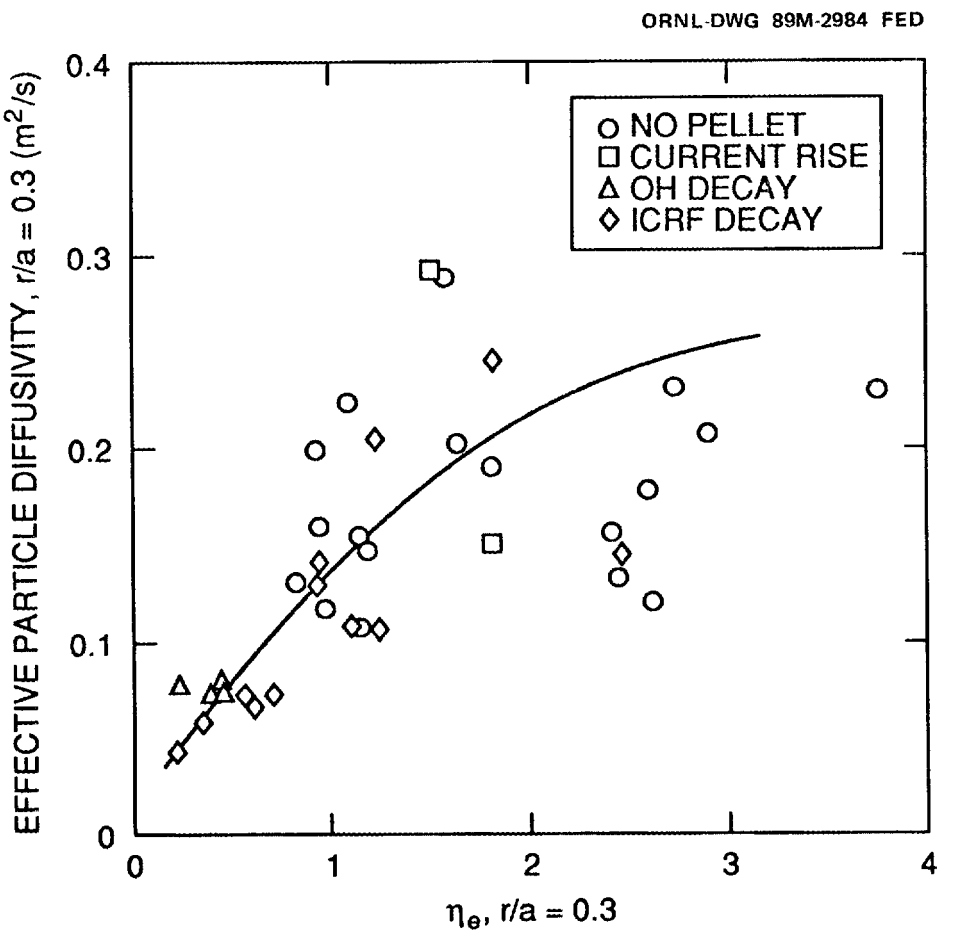

Fig. 5.18 Effective particle diffusivity (electron) at $r/a = 0.3$ as a function of local $\eta_e = L_{n_e}/L_{T_e}$. Values are averaged over 400 ms during a discharge.

uncertainty in the thermal diffusivity calculation because of uncertainty in the ICRF power deposition and in the split between electron heating and ion heating. The calculations done here assumed ion temperature profiles with the same profile shape as the electron profile with magnitude scaled to the central ion temperature. The ICRF power split was assumed to be 60% to the electrons. The local effective thermal diffusivity of the auxiliary heated discharges is plotted in Fig. 5.19 as a function of the density peakedness. The times chosen are during the steady-state period of the ICRF heating. We see that the effective thermal diffusivity shows a trend similar to the particle diffusivity at this radius. The normal L-mode limiter behavior is seen to yield effective thermal diffusivities on the order of $\sim 1.5\,\mathrm{m}^2/\mathrm{s}$ when the peaking factor is on the order of 1.4. The discharges with more peakedness due to pellet injection with central particle deposition show a decrease in effective thermal diffusivities to $\sim 0.5\,\mathrm{m}^2/\mathrm{s}$ for discharges with central to volume-averaged electron density ratios greater than 2.5. The ratio of the effective electron thermal diffusivity to the effective particle diffusivity for these discharges is in the range of 3 to 5.

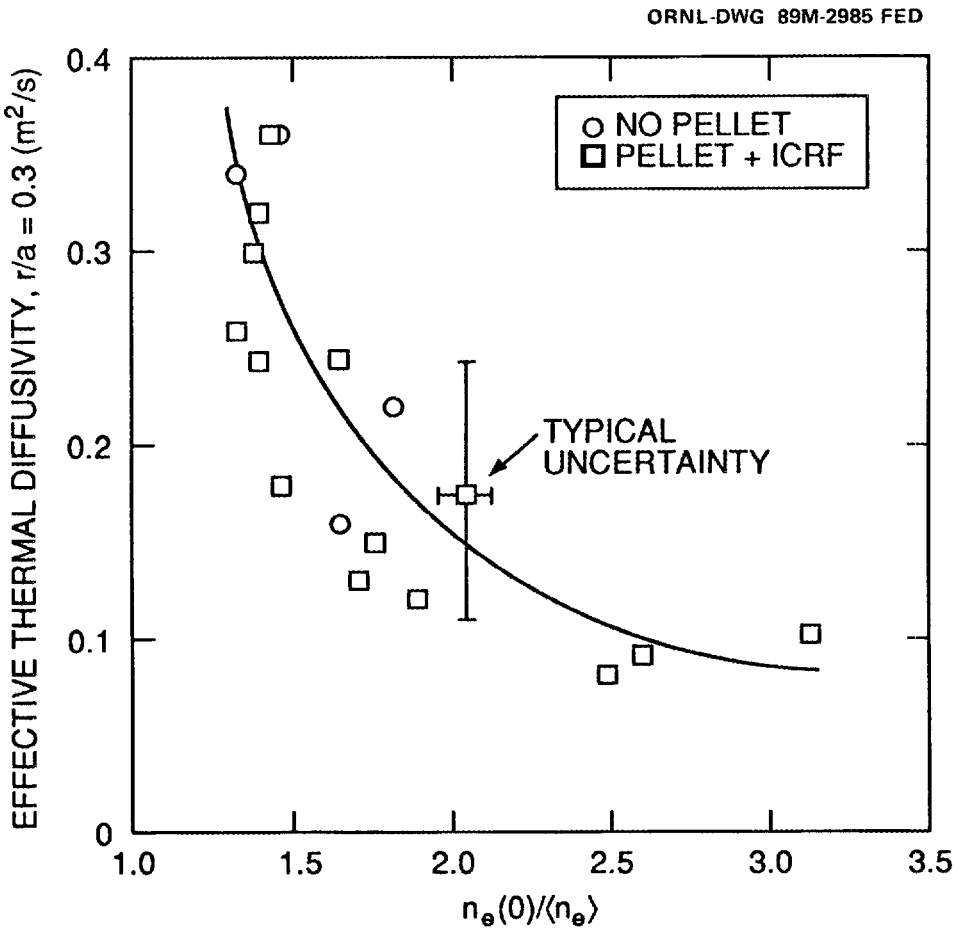

Fig. 5.19 Effective electron thermal diffusivity at $r/a = 0.3$ as a function of density profile peakedness. Values are averaged over 400 ms during a discharge.

CHAPTER 6

ANOMALOUS PARTICLE TRANSPORT

The transport of particles and energy in tokamaks is generally recognized as being highly anomalous, especially for electrons. In this chapter we examine some of the most plausible theoretical models for anomalous particle transport in tokamaks and discuss their relevance to the particle transport determined in the pellet fueling experiments on JET. In the first section, calculations of particle diffusion coefficients for different theories of anomalous transport are compared with the experimentally determined effective diffusivity. In the second section, we present calculations of fluctuation induced particle and heat fluxes from electrostatic fluctuations using a recently developed fluctuation induced neoclassical quasilinear transport theory. These calculated fluxes are then compared to the experimentally determined anomalous particle and heat transport fluxes to determine if the relationship predicted between them is upheld.

6.1 Anomalous Transport Mechanisms

Particle and heat transport have been analyzed in a number of tokamak experiments [49,67] over a wide range of conditions and have often shown good agreement with the neoclassical ion heat transport under some conditions, but have shown a large anomaly in both heat and particle transport for electrons. Explanations of the observed anomalous electron behavior usually depend on fluctuations of electric and magnetic fields [67,68] as discussed in Sect. 4.3. The fluctuations are believed to be generated by many different instability mechanisms causing plasma turbulence.

In this section we introduce the basic features of some of the most likely instability mechanisms that are thought to cause fluctuations and discuss their relevance to the particle transport in the JET pellet fueling experiments. Some of the models of turbulence and anomalous transport from these instabilities in tokamaks are introduced and their predictions are compared to the observed particle transport.

6.1.1 Electron drift wave instabilities

The most frequently mentioned cause of anomalous transport in tokamaks is the electron drift wave instability. The drift instability in magnetically confined plasmas has been believed to enhance the particle and/or thermal diffusivity across a confining magnetic field by orders of magnitude. The presence of plasma density fluctuations with frequency spectra that have dominant frequency components in the range of the drift frequency has been experimentally confirmed in CO_2 laser scattering experiments. The direction of poloidal propagation of these fluctuations has often been found to be in the electron diamagnetic direction [67]. The mechanism reponsible for this instability is the diamagnetic drift velocity, which is given by

$$\vec{v}_{de} = \frac{1}{eB^2 n_e} \vec{\nabla} p_e \times \vec{B}\,, \tag{6.1}$$

where e is the electron charge, n_e the electron density, and p_e the electron pressure. It is clear that the diamagnetic drift velocity given in Eq. (6.1) is not a guiding center velocity. The diamagnetic current is simply due to the nonuniform magnetic dipole moment density, as is shown in Fig. 6.1, and is primarily directed perpendicular to the magnetic field.

If we consider a wave with low phase velocity along B_0 that does not perturb B_0 but allows thermalization along the field line, we get in slab geometry from

ORNL-DWG 89M-2658 FED

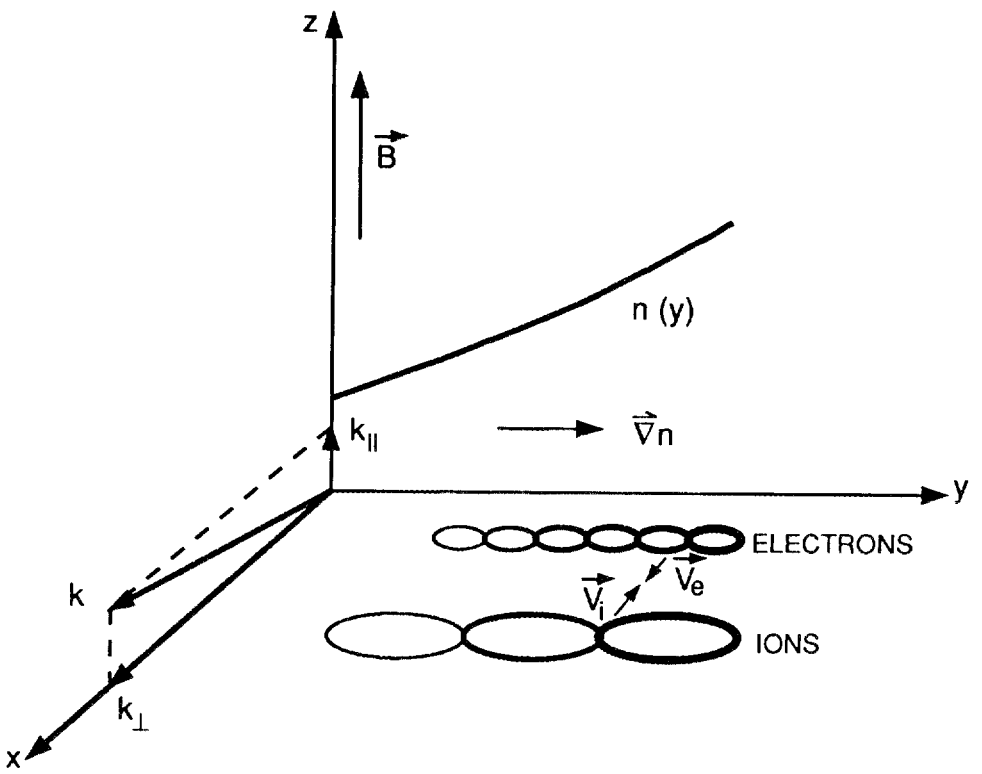

Fig. 6.1 Geometry for an electrostatic drift wave.

linearization of the ion continuity equation

$$-i\omega n_1 + \vec{v}_i \cdot \vec{\nabla} n_0 = 0\,, \tag{6.2}$$

where n_1 is the perturbed ion density and n_0 is the unperturbed density. Since v_i results primarily from the $\vec{E} \times \vec{B}$ drift, we have

$$n_1 = \frac{1}{i\omega}\vec{\nabla} n_0 \cdot \frac{\vec{E} \times \vec{B}_0}{B_0^2} = \frac{-1}{i\omega}\vec{\nabla} n_0 \cdot \frac{\vec{\nabla}\phi \times \vec{B}_0}{B_0^2}\,, \tag{6.3}$$

where ϕ is the scalar potential associated with the density perturbation. If both the density n and potential ϕ have a space-time dependence given by

$$e^{[i(\vec{k}\cdot\vec{x} - \omega t)]}\,, \tag{6.4}$$

with $k_\perp >> k_\parallel$, Eq. (6.3) becomes

$$n_1 = \frac{\omega_{*e}}{\omega}\frac{e\tilde{\phi}}{T_e} n_0\,, \tag{6.5}$$

where

$$\omega_{*e} = \frac{T_e}{eB_0^2}\left[\vec{\nabla}(\ln\, n_0) \times \vec{B}_0\right] \cdot \vec{k}_\perp = \frac{T_e}{eB_0 L_n} k_\perp \tag{6.6}$$

is the electron diamagnetic frequency, and the density scale length is given by

$$L_n^{-1} \equiv \frac{|\vec{\nabla} n_0|}{n_0} > 0\,. \tag{6.7}$$

For electrons, with finite $k_\parallel$ such that thermal equilibrium can be established along field lines ($k_\parallel v_{te} >> \omega$), the Boltzmann relation is obeyed:

$$n_e = n_0 \frac{e\tilde{\phi}}{T_e}\,. \tag{6.8}$$

Then by invoking quasineutrality (equating n_i to n_e), we get the relation

$$\omega = \omega_{*e} \,. \tag{6.9}$$

Drift waves are so called because their propagation velocity across the magnetic field is of the order of the electron diamagnetic drift velocity. We notice that the drift frequency depends on the density gradient scale length and not on the temperature gradient. Dependence on the temperature gradient appears as a higher order effect. The exchange of energy between the plasma and drift wave is controlled by the phenomenon of Landau damping. Interaction with ions damps the wave, but since the phase velocity of the wave parallel to the magnetic field, $\omega/k_{\|}$, is greater than the ion thermal velocity, only the ions in the energetic tail of the distribution have an effect, and the damping is weak. The Landau resonance with the electrons provides an energy input to destabilize the wave. Theory predicts that the toroidal variations in tokamaks can be strong enough to destabilize the drift wave [67]. Although the drift wave is primarily an electrostatic disturbance, a small magnetic component is also present and may drive anomalous electron thermal transport. This magnetic component is a function of β and therefore is expected to be more prevalent in high-temperature (pressure) cases.

6.1.2 Ion pressure gradient driven instabilities

Another important relevant instability mechanism is the ion pressure gradient driven mode or ion mixing mode (η_i-mode) [69,70], where $\eta_i = L_{n_i}/L_{T_i} = d\ln T_i/d\ln n_i$. It is essentially an electrostatic mode resulting from the coupling of sound waves with frequency $\omega^2 = k_{\|}^2 c_s^2$ to an ion diamagnetic thermal mode $\omega \approx w_{*i}\,\eta_i$ that is driven by the radial ion temperature gradient. It is predicted by

the fluid equations in a shear-free slab model with $\nabla n \to 0$, with the dispersion relation being [4]

$$\omega^2 = k_\parallel^2 c_s^2 \left[1 - \frac{\omega_{*i}\eta_i}{\omega} \left(1 + \frac{5}{3}\frac{T_i}{T_e} \right) \right], \tag{6.10}$$

which predicts unstable modes when $k_\parallel^2 c_s^2 \ll \omega_{*i}\eta_i$. The mode with magnetic shear has a threshold for $\eta_i > \eta_{ic} \sim 1.5$, so that it is expected to be important with broad density profiles ($\eta_i > 1.5$). Ultimately, ion Landau damping truncates the spectrum at $k_\theta \rho_s \approx 1$. The η_i-mode propagates in the ion diamagnetic direction (opposite the electron diamagnetic direction). It is expected to be difficult to distinguish η_i-modes from drift wave modes except in regard to the direction of propagation. However, in flat density regions, drift wave turbulence is expected to be weak, so that η_i-modes should dominate in these regions. It is also interesting to note that edge-peaked impurity concentrations enhance the turbulence, while centrally peaked concentrations tend to quench it [70]. This mode has also been assumed to be responsible for anomalous inward particle pinches that have been inferred by others [65].

It is important to note that ion pressure gradient modes have been experimentally inferred in the TEXT tokamak microturbulence spectrum from far-infrared scattering measurements [71]. The modes observed on TEXT propagated in the ion propagation direction and existed in high-density discharges where the density scale length L_n was relatively large. With pellet injection, the density profile was measured to be sharply peaked as compared to the gas fueled discharge, and the presumed η_i-mode features were not observed. The existence of the ion pressure gradient instability was also correlated with the saturation in energy confinement seen in TEXT with higher density. These results are consistent with other

tokamak results, which have seen improvement in confinement with pellet injection that leads to peaked density profiles.

The particle flux predicted by the η_i-mode transport theory of Lee and Diamond [70] can be written (for $\eta_e \approx \eta_i$) as:

$$\Gamma_\eta = -\mathrm{D}_\eta \left(\frac{\partial n}{\partial r} - \frac{1}{c_T} \frac{n}{T_e} \frac{\partial T_e}{\partial r} \right), \tag{6.11}$$

where D_η is nonzero only for the case $\eta_e > \eta_{\mathrm{crit}} \approx 1.5$ and positive values of c_T imply inward particle convection.

In the collisionless or banana regime ($\nu_e^* < 1$), the dissipative trapped-electron response results in a phase shift between the fluctuating particle density and the fluctuating electrostatic potential of the wave. The net particle flux, in this regime, is found to be directed radially outward ($c_T < 0$). Assuming that $\eta_i \approx \eta_e$, D_η can be written as [70]:

$$\mathrm{D}_\eta(\rho) = 2\,\epsilon^{3/2} \left[\frac{\pi}{2} \ln(1+\eta_i) \right]^2 \left(\frac{1+\eta_i}{\tau} \right)^3 \frac{c_s^2 \rho_s^2}{\nu_e L_s^2}, \tag{6.12}$$

where c_s is the ion sound speed ($c_s \equiv \sqrt{T_e/m_i}$), $\tau = T_e/T_i$, ρ_s is the ion Larmor radius with the electron temperature, $\rho_s \equiv c_s/\omega_{ci}$, where ω_{ci} is the ion cyclotron frequency, ϵ is the inverse aspect ratio ($\epsilon = r/R_0$), and L_s is the magnetic shear scale length $\left[L_s \equiv \frac{q^2}{\epsilon} \left(\frac{\partial q}{\partial \rho} \right)^{-1} \right]$.

Another recently proposed model for anomalous transport based on η_i-mode driven microinstabilities is that of Romanelli and Briguglio [72]. In their model the effect of trapped electrons on the η_i stability and the effect of the ion magnetic drift (ω_{di}) resonance are considered. In particular, the value of the critical η_i is found to be affected by the trapped electrons. The critical η_i from this theory for JET plasma conditions can be well above the nominal value of 1.5, as is shown in Fig. 6.2 along with the density and temperature scale lengths for a pellet fueled discharge.

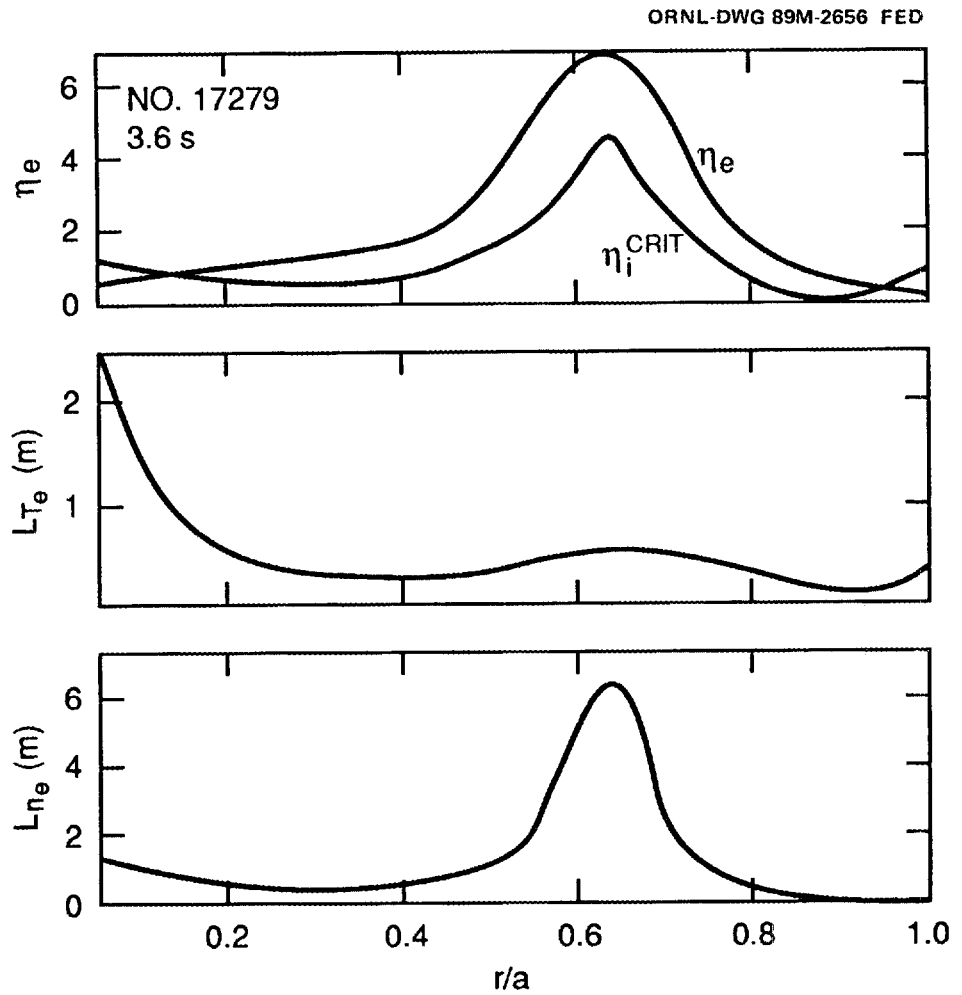

Fig. 6.2 Experimental η_e profile and calculated η_i^{CRIT} from Romanelli and Briguglio [72] along with temperature and density scale lengths. Note that η_i^{CRIT} can be far in excess of the nominal 1.5 value.

The particle flux predicted by this η_i-mode transport theory can be written (for $\eta_i \approx \eta_e$) as:

$$\Gamma_e = 4.3 \frac{v_{ti}\,\rho_i^2}{R} \frac{T_i}{T_e} \eta_e \nabla n \,(2\epsilon)^{1/2}\,\Gamma\,, \tag{6.13}$$

where Γ is given by the expression

$$\Gamma = \frac{R}{2L_n}\left(P_1 + P_2 \frac{T_e}{T_i}\eta_e\right), \tag{6.14}$$

with L_n being the density scale length. The terms P_1 and P_2 are given by the expressions

$$P_1 = \frac{0.1(1+5\epsilon_n)}{1+0.04\nu}\left[1 - \frac{60\epsilon_n/\epsilon_{nc}}{(1-6\epsilon_n/\epsilon_{nc})}\frac{10}{10+\nu}\right], \tag{6.15}$$

$$P_2 = \frac{0.05}{1+0.01\nu}\left\{1 - 2\left[1-(1-\epsilon_n/\epsilon_{nc})^2\right]\frac{3}{3+\nu}\right\}, \tag{6.16}$$

where the terms $\nu = 50\nu_e^* T_e/T_i$, $\epsilon_n = L_n/R$, and ϵ_{nc} is given by

$$\epsilon_{nc} = \frac{3}{2}\left[1 - \eta_i + \frac{(1-\eta_e)(2\epsilon)^{1/2}T_i}{T_e(1+2.5\nu)}\right]\Big/(1+T_i/T_e)\,. \tag{6.17}$$

From the particle flux relation in Eq. (6.13), we can see that there are two terms, a diffusive term proportional to ∇n and a convective term proportional to $n\nabla T/T$. The diffusivity given by this relation can then be written as

$$\mathrm{D}_e = 4.3 \frac{v_{ti}\,\rho_i^2}{R} \frac{T_i}{T_e} \eta_e \,(2\epsilon)^{1/2}\, P_1 \frac{1}{2\epsilon_n}\,, \tag{6.18}$$

and the convective term can be written as

$$v_e = 4.3 \frac{v_{ti}\,\rho_i^2}{R} \eta_e^2 \nabla n\,(2\epsilon)^{1/2}\, P_2 \frac{1}{2\epsilon_n}\,. \tag{6.19}$$

From these relations we can see that both the diffusivity and the convective velocity scale as $T_i^{3/2} L_T$ and therefore would be expected to be peaked toward the center of the discharge as the value of η_i rises above the critical value.

Another theory of ion pressure gradient driven instabilities by Biglari, Diamond, and Rosenbluth [73] that has been recently introduced takes into account trapped ion effects when the collisionality is low ($\nu_i/\epsilon < \omega_{*i}$). A scaling of particle diffusivity is obtained by making the usual mixing-length assumptions about the turbulence and is given by

$$\mathrm{D}_\eta \sim \epsilon^2 \rho_s^2 \frac{\omega_{*e}\omega_{de}}{b_\theta \hat{s}^2 \nu_e} \frac{1+\eta_i}{\tau}\,. \tag{6.20}$$

In this expression, $b_\theta = (k_\theta \rho_i)^2/2$, ω_{de} is the magnetic drift frequency given by $\omega_{de} = k_\theta \rho_e v_{te}/R$, $\hat{s}$ is the magnetic shear given by $\hat{s} = d\ln q/d\ln r = rq'/q$, and $\tau = T_e/T_i$. We have calculated the particle diffusivity based on this scaling using the experimental data and typically find diffusivity profiles much the same as those for the Lee and Diamond theory. This is not surprising, considering that both theories predict a similar $(1+\eta_i)/\tau$ dependence on the diffusivity.

An example of calculations of the diffusivity based on these collisionless η_i-mode theories is shown in Fig. 6.3 for the peaked density profile discharge described in Fig. 3.11. The values of D_η calculated from the three theories in Eqs. (6.12), (6.18), and (6.20) are shown along with the neoclassical diffusivity, Bohm diffusivity, and experimentally determined diffusivity for reference. The maximum diffusivity for the Lee and Diamond model is at $r/a \sim 0.6$ and has a value within an order of magnitude of the experimentally determined diffusivity; however, the profiles of the experimentally determined D and D_η

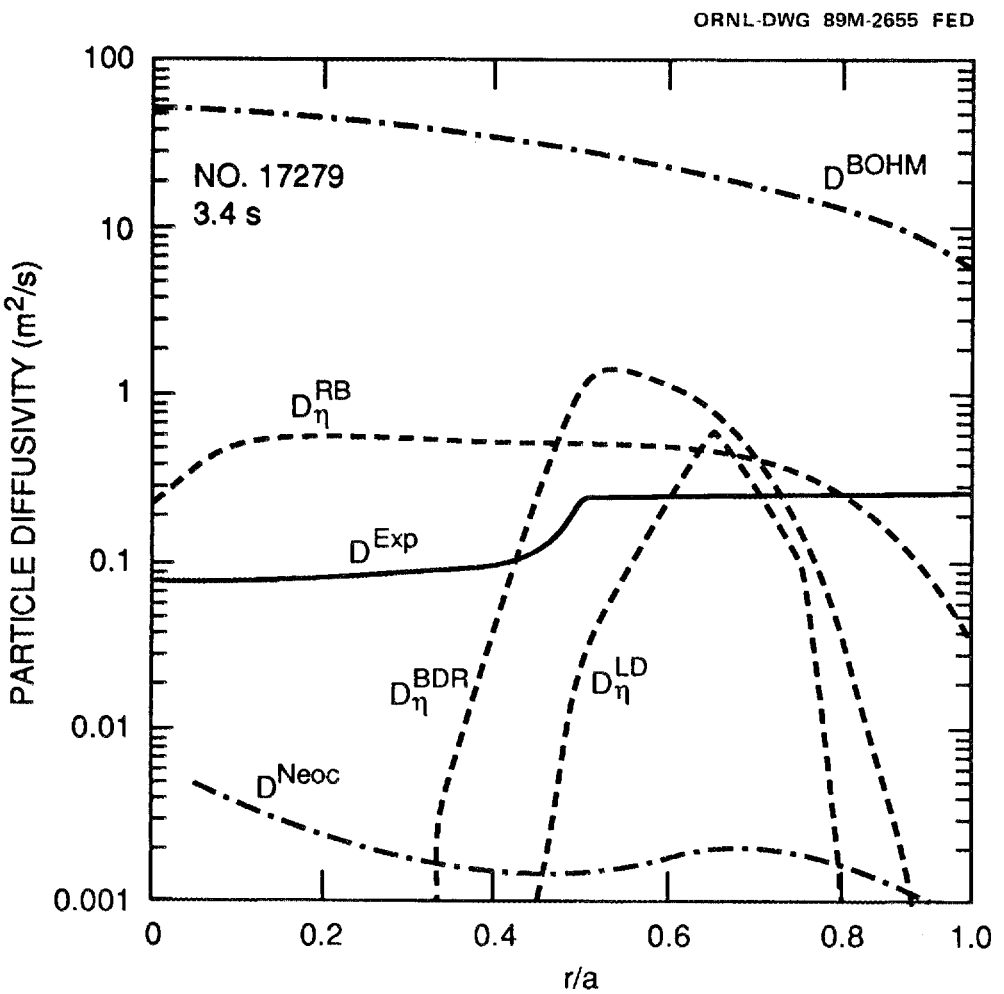

Fig. 6.3 Experimental particle diffusivity compared with theoretical η_i-mode diffusivities for a peaked density profile pellet fueled discharge. The values calculated from Lee and Diamond [70], Romanelli and Briguglio [72], and Biglari, Diamond, and Rosenbluth [73] are shown, as are the neoclassical and Bohm particle diffusivities for reference.

are significantly different. This comparison holds true also in the nonpeaked profile cases. In all cases, though, there is significant uncertainty in the measured η_i due to uncertainty in the ion density and temperature profiles, and therefore large uncertainties exist for D_η and v_η. The convective velocity predicted by the Lee and Diamond η_i theory [70] is outwardly directed and has a magnitude and profile similar to the D_η prediction, since the temperature scale length is of order 1 across most of the discharge minor radius. D_η and v_η are both predicted to be zero near the center of the discharge, which does not agree with the experimentally determined anomalous central diffusivity but does agree with the negligible anomalous convective velocity.

It is particularly interesting to look at the calculated particle transport coefficients from the η_i theory of Romanelli and Briguglio [72]. The particle diffusivity D and convective velocity v from this theory are driven primarily by the temperature gradient. The values calculated for D and v from this theory are shown in Fig. 6.4 for the same discharge whose temporal evolution is shown in Fig. 3.11. The value of diffusivity calculated from this theory is also plotted in Fig. 6.3 with the experimentally determined value, the neoclassical value, and the value from the other η_i theories. The evolution of the value of η_e is shown for this discharge in Fig. 6.5 for the same time steps as in Fig. 6.4. We can see that the value of electron diffusivity predicted by this theory is larger than the experimental value and becomes even greater as the temperature is increased due to the temperature gradient dependence of D. The convective velocity predicted from this theory is inward and has a large magnitude that is also due to the strong temperature gradient dependence. Clearly, the values of D and v predicted for the pellet fueled discharges are much larger than the determined values from the modeling described in Chapter 5.

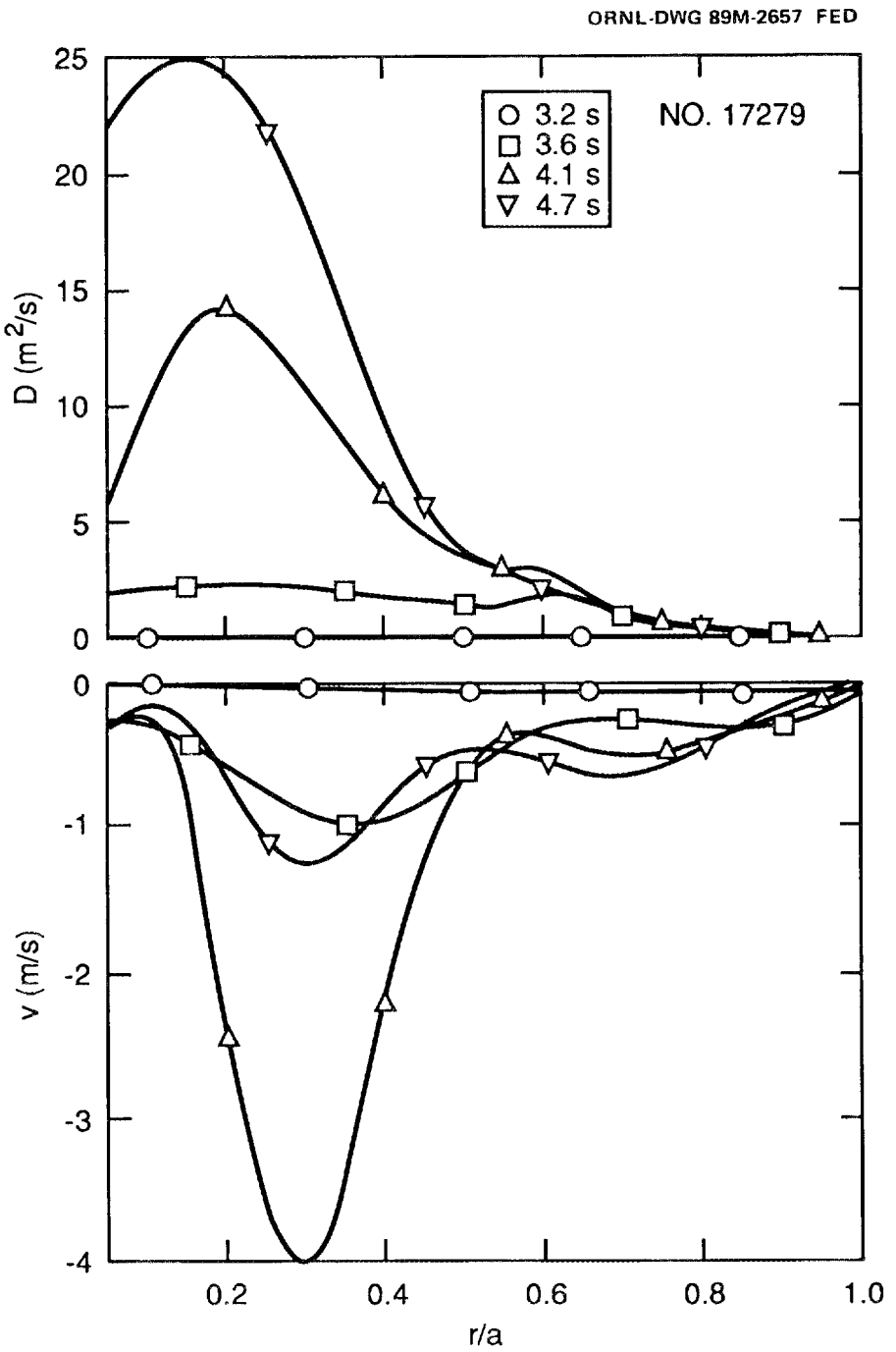

Fig. 6.4 Evolution of the calculated particle diffusivity D and convective velocity v from the Romanelli and Briguglio [72] η_i theory.

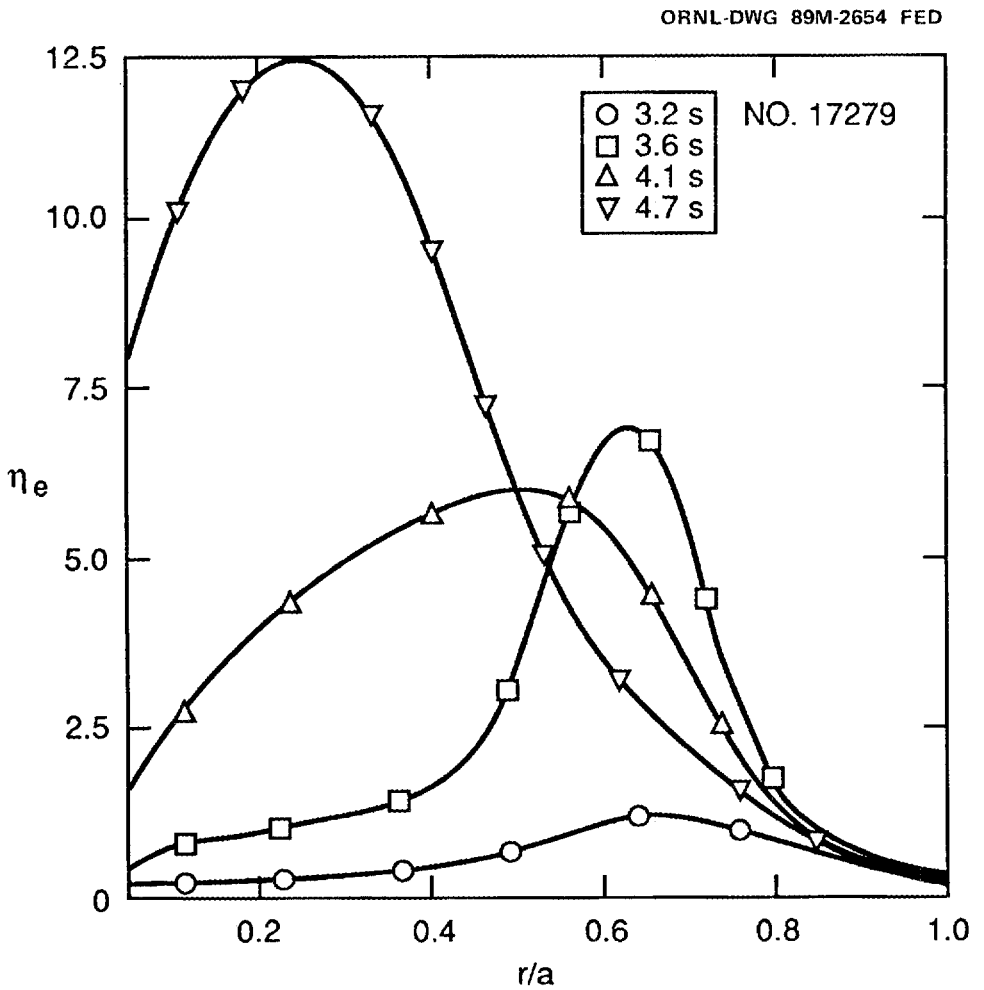

Fig. 6.5 Evolution of the parameter η_e during the auxiliary heated phase of a pellet fueled peaked density discharge. A 4 mm pellet is injected at 3 s and 7 MW of ICRF heating is applied from 3.2 s to 5.2 s.

None of the η_i transport theories investigated give particle transport coefficients that compare well with the determined values; however, strong inferences should not be drawn since the experimental ion profiles were not available. The different assumptions about the turbulence generated by the modes and their effect on particle transport can make a large difference in transport coefficients, as the comparison in Fig. 6.3 shows. All of the theories investigated show qualitative agreement with the increase in diffusivity as the density profile becomes less peaked. However, the very strong inward convective velocity predicted by the Romanelli and Briguglio theory is clearly not supported by the experimental data.

6.1.3 Magnetic field stochasticity

When the magnetic surfaces in a tokamak have a radial perturbation $\tilde{B}_r$ superimposed on the ideal magnetic surfaces, the resulting particle motion along the field lines will have a radial component $\tilde{v}_r$ which will lead to enhanced radial transport as discussed in Chapter 4. If the perturbation is large enough and many of the magnetic surfaces are involved, the field lines become stochastic. Calculations of the particle diffusion resulting from the diffusion of the stochastic field lines have been done [67], and it is found that the particle diffusion is limited by the ion diffusion, which is much slower than the electron diffusion because of the lower ion velocities. If the electrons attempt to diffuse faster than the ions, ambipolar electric fields will arise that serve to restrain the electrons and leave the particle flux ambipolar.

There have been several calculations of transport in specified stochastic magnetic fields. The particle transport calculations by Boozer and White [74] show a diffusion coefficient in the stochastic regime given approximately as

$$\mathrm{D}_s = v_{\|}\mathrm{D}_m = \frac{\rho}{a}\frac{\pi}{8\psi\epsilon}\sum_{m,n}\left[m\,\alpha_{m,n}(\psi)\right]^2, \tag{6.21}$$

where $\alpha_{m,n}$ is the magnitude of the perturbation, $\simeq (1/m)(\delta B/B)$, ρ is the gyroradius, and D_m is the diffusion coefficient for the magnetic field itself. Diffusion coefficients for electrons were calculated to be several orders of magnitude above neoclassical values for modest fluctuation levels ($\alpha \simeq 10^{-5}$) in the magnetic field.

Measurements of magnetic fluctuations at the plasma edge on JET have been made, and two types of fluctuation activity have been found [75]. Modes were found with relatively high m (up to $m \sim 100$) that propagated in the electron diamagnetic drift direction. It is quite possible that these modes are of a turbulent drift wave type as discussed in Sect. 6.1.1. There were also fluctuations observed with low m, n modes that appear as standing waves and dominate the magnetic spectrum in discharges with additional heating. It is this mode that is more likely similar to the MHD activity observed in the pellet fueled heating experiments discussed in Sect. 3.4. The cause of the mode may be low-n resistive modes or low-m tearing modes [75]. These magnetic fluctuations have been estimated to produce a radial perturbation that is large enough to produce a stochastic field. The transport from this stochasticity as discussed above is likely to be in excess of the neoclassical predictions. The actual level of the transport from the magnetic fluctuations is difficult to estimate, however, without more detailed measurements of the modes and their fluctuation amplitudes {i.e., $\sum_{m,n}\left[m\,\alpha_{m,n}(\psi)\right]^2$ from Eq. (6.21)}.

6.2 Calculations of Fluctuation Induced Transport in JET

In this section we analyze the particle and heat transport in JET pellet fueled discharges by examining the relationship between the anomalous electron

particle and the anomalous electron heat flux with the recently developed neoclassical quasilinear theory of fluctuation induced transport [76]. In this theory, the methodology developed for neoclassical transport theory is used to calculate the transport fluxes induced by electrostatic and magnetic fluctuations. The perturbed particle distribution function is substituted into the flux-force relationships. Only the coherent response is included, therefore leading to a quasilinear theory. The fluctuation spectrum is assumed as given with a real frequency ω (without a growth rate), as is appropriate for saturated turbulence. The fluctuation collisionality regime is assumed to be in the plateau regime in this formulation of the theory (i.e., the fluctuation is not far removed from the mode rational surface).

The complete set of transport fluxes induced by fluctuations in this theory satisfies Onsager symmetry. The anomalous electron transport matrix is given by [76]

$$\begin{pmatrix} \left(\Gamma_e^{\mathrm{AN}}\right)_r \\ \left(q_e^{\mathrm{AN}}/T_e\right)_r \\ J_{\parallel}/T_e \end{pmatrix} = \begin{pmatrix} D_e & -\frac{3}{2}D_e & W \\ -\frac{3}{2}D_e & \frac{13}{4}D_e & -0.87\,W \\ W & -0.87\,W & \sigma_{e\phi}/T_e \end{pmatrix} \begin{pmatrix} X_{1r} \\ X_{2r} \\ E_{\parallel}^{A} \end{pmatrix}, \tag{6.22}$$

where the forces are given by

$$X_{1r} = -\left\langle \frac{\omega_{mn}}{m} \right\rangle \frac{eBr}{cT_e} - \frac{T_i}{T_e}\frac{1}{P_i}\frac{dP_i}{dr} - \frac{e}{T_e}\frac{d\tilde{\Phi}}{dr} + \frac{T_e + T_i}{T_e}\frac{1}{P}\frac{dP}{dr},$$

$$X_{2r} = \frac{1}{T_e}\frac{dT_e}{dr},$$

and the coefficients for electrostatic fluctuations are

$$D_e = \frac{-\sqrt{\pi}}{4}\rho_e^2 \frac{v_{te}}{Rq} N \left[\sum_{m,n,\omega} \frac{m^2}{|m-nq|} \left(\frac{e\tilde{\Phi}_{mn\omega}}{\sqrt{2}T_e} \right)^2 \right],$$

$$W = \frac{-\sqrt{\pi}}{2} \frac{c}{B_\theta} \frac{v_{te}}{Rq} \frac{N}{\nu_{ei}} \left[\sum_{m,n,\omega} \frac{m(m-nq)}{|m-nq|} \left(\frac{e\tilde{\Phi}_{mn\omega}}{\sqrt{2}T_e} \right)^2 \right],$$

$$\sigma_{e\phi} = \sigma_s \left(1 - 0.35\sqrt{\pi} \frac{v_{te}}{Rq\,\nu_{ei}}\right) \left[\sum_{m,n,\omega} |m-nq| \left(\frac{e\tilde{\Phi}_{mn\omega}}{\sqrt{2}T_e} \right)^2 \right],$$

where m and n are poloidal and toroidal mode numbers of the fluctuation amplitude $\tilde{\Phi}$ with frequency ω, P is the plasma pressure, v_{te} is thermal electron velocity, N is the density, B_θ is the poloidal magnetic field strength, σ_s is the Spitzer conductivity, ρ_e is the electron cyclotron radius, ν_{ei} is the electron-ion collision frequency, and $E_\parallel^A$ is the inductive parallel electric field. The term $\langle \omega_{mn}/m \rangle$ is actually a summation over all modes given by

$$\left\langle \frac{\omega_{mn}}{m} \right\rangle = \sum_{m,n,\omega} \frac{m\omega}{|m-nq|} \tilde{\Phi}^2_{mn\omega} \left[\sum_{m,n,\omega} \frac{m^2}{|m-nq|} \tilde{\Phi}^2_{mn\omega} \right]^{-1} \tag{6.23}$$

In our analysis of the anomalous transport, we examine the anomalous particle and heat flux calculated in JET pellet fueled plasmas and determine whether the relationships

$$\begin{aligned} \Gamma_e^{AN} &= D_e X_{1r} - \frac{3}{2} D_e X_{2r} + W\, E_\parallel^A \\ q_e^{AN}/T_e &= -\frac{3}{2} D_e X_{1r} + \frac{13}{4} D_e X_{2r} - 0.87\, W\, E_\parallel^A, \end{aligned} \tag{6.24}$$

hold for specific cases. It is reasonable to assume that the last terms due to the so-called Ware pinch effect should be small since measurements of fluctuations on tokamaks have shown $k_\parallel \ll k_\theta$ [77] and W is proportional to $k_\theta k_\parallel / k_\parallel$, whereas the coefficient D_e is proportional to $k_\theta^2/k_\parallel$. The fluctuation spectrum

$\sum_{m,n,\omega}(m^2/|m-nq|)\left(e\tilde{\Phi}_{mn\omega}/\sqrt{2}T_e\right)^2$ is assumed constant during the time the flux is calculated. It should be noted that the corresponding results for magnetic fluctuations $\tilde{A}_{\|}$ can be obtained by making the substitution for the electrostatic fluctuation amplitude given by [76]

$$\tilde{\Phi}_{mnw} \leftrightarrow \tilde{A}_{mnw} w^E_{mn} / \left[c(\hat{n}\cdot\nabla\Theta)(m-nq)\right] . \tag{6.25}$$

The transport matrix in Eq. (6.22) is then the same for electrostatic and magnetic fluctuations with the only change being in the fluctuation spectrum amplitude.

The measurement of the radial electric field, $d\phi/dr$, is not available for JET, so a calculated radial electric field is used. This field is calculated from force balance considerations. For a single species of mass m_j and charge e_j the force is given by

$$\begin{aligned} \vec{F} &= m_j n_j \left[\frac{\partial \vec{v}_j}{\partial t} + (\vec{v}_j\cdot\nabla)\vec{v}_j\right] + m_j \vec{v}_j \left[\frac{\partial n}{\partial t} + \vec{v}_j\cdot\vec{\nabla} n_j\right] \\ &= -\vec{\nabla} P_j + e_j n_j(\vec{E} + \vec{v}_j\times\vec{B}) - \nabla\cdot\vec{\Pi} + \vec{R}^c_j , \end{aligned} \tag{6.26}$$

where $\vec{\Pi}$ is the viscosity tensor and $\vec{R}^c$ is the collisional friction between different ion species. The rotation velocities of impurities and ions are not necessarily the same but can differ only by a few percent. In the flux surface geometry the force balance from Eq. (6.26) can be written as

$$-U_{i\theta} + \frac{U_{i\phi}}{q} = -\frac{\langle T_i\rangle}{eB_\theta}\left(\frac{\langle P_i\rangle'}{\langle P_i\rangle} + \frac{e\langle\phi\rangle'}{\langle T_i\rangle}\right) , \tag{6.27}$$

where $U_{i\theta}$ and $U_{i\phi}$ are the poloidal and toroidal rotation velocities. We assume that there is no poloidal rotation ($U_{ip} \approx 0$) and use the measured toroidal rotation from Doppler-shifted impurity ions from the charge-exchange recombination spectrometer diagnostic when neutral beam injection heating is used. Therefore,

the radial electric field used in the calculations is given by

$$\langle\phi\rangle' = \frac{U_{\rm it}}{q} B_\theta + \frac{\langle P_{\rm i}\rangle'}{e\langle n_{\rm i}\rangle} . \tag{6.28}$$

In cases where there is no neutral beam heating, the poloidal and toroidal rotation is assumed to be negligible. In these cases the radial electric field is given by

$$\langle\phi\rangle' = \frac{\langle P_{\rm i}\rangle'}{e\langle n_{\rm i}\rangle} . \tag{6.29}$$

In our analysis we assume that the anomalous transport in JET plasmas is driven by electrostatic drift wave fluctuations. Since we have no measurement of the fluctuation spectrum, we assume that the fluctuations have a frequency spectrum dominated by either the electron or the ion diamagnetic drift frequency given by Eq. (6.6). In our analysis, we avoid using any discharges with enhanced levels of low-m MHD fluctuations (as discussed in Sect. 3.4) so as not to mask the transport possibly caused by the higher m mode electrostatic drift wave turbulence.

In calculating the diamagnetic drift frequency, we use measurements of plasma turbulence that have been made on other tokamaks. In particular, the perpendicular wavevector spectrum, $k_\perp$, has been determined in a number of fluctuation measurements on different tokamaks and a relatively homogeneous picture has emerged. The wavevector spectrum in these experiments has generally been a relationship between $k_\perp$ and ρ_s such that the mean wavenumber falls in the range [67]

$$\langle k_\perp\rangle\rho_s \cong 0.1\text{–}0.3 . \tag{6.30}$$

In this expression, $\rho_s = c_s/\omega_{\rm ci}$, where c_s is the sound speed $[c_s = (T_{\rm e}/m_{\rm i})^{1/2}]$ and $\omega_{\rm ci}$ is the ion cyclotron frequency. The wavevector parallel to the magnetic field,

$k_{\|}$, has been measured to be much smaller than the perpendicular wavevector, $k_{\|} \ll k_{\perp}$ [67,77]. The perpendicular wavevector, $k_{\perp}$, is a combination of a radial component k_r and a poloidal component k_θ. Measurements of $k_{\perp}$ on TEXT using a heavy-ion beam probe have suggested that there is little contribution to $k_{\perp}$ from k_r [53,77]. The poloidal wavenumber, k_θ, satisfies the relation

$$k_\theta = m/r\,, \tag{6.31}$$

where m is the poloidal mode number and r is the minor radius.

For our fluctuation spectrum in Eq. (6.23) we choose a discrete frequency based on the diamagnetic frequency such that

$$\frac{\omega_{mn}}{m} = \frac{T_e k_\theta}{eB_0 L_n}\frac{1}{rk_\theta} = \frac{T_e}{eB_0 L_n r}\,, \tag{6.32}$$

where we have used the relation in Eq. (6.31). Therefore, we can see that as long as the dispersion relation between w_{mn} and k_θ yields the diamagnetic drift velocity [defined in Eq. (6.1)], we will have a single value of ω_{mn}/m at each radial location in the plasma.

The calculated magnitude of the different generalized forces in Eq. (6.22) for the case of electrostatic drift wave driven fluctuations is shown in Fig. 6.6 for a pellet fueled peaked density profile discharge with ICRF heating. We see from this figure that the fourth term in the generalized force X_{1r} labeled X_{1r4} is the dominant term and is larger than the first term X_{1r1}, which is proportional to the fluctuation frequency ω_{mn}/m. The term X_{1r1} is effectively equal to $-L_n^{-1}$ from Eq. (6.32) and therefore has a relatively small magnitude since L_n is generally of order 1 or larger as shown in Fig. 6.2. The second and third terms, which have the opposite sign (due to the gradients), are effectively inward driving forces since they give an inward particle flux. These pinch terms are, however, smaller than

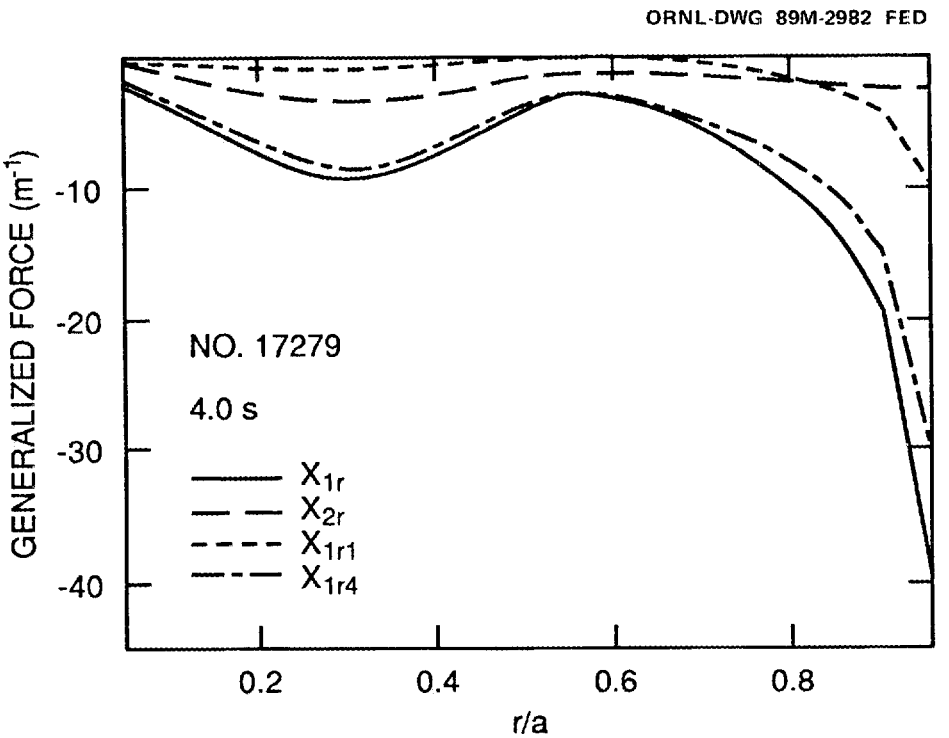

Fig. 6.6 Profiles of the calculated generalized forces in the quasi-linear fluctuation transport theory for an ICRF heated, pellet fueled discharge. The forces are defined in Eq. (6.22). The electron diamagnetic frequency is used for ω_{mn}/m in X_{1r1}.

the first and fourth terms, which give a net outward driving force and cancel each other when there is no rotation from Eq. (6.29). The outward force terms are seen to dominate especially in the outer half of the minor radius.

The amplitude of the fluctuations is calculated such that the anomalous particle flux is given by Eq. (6.24). Essentially, the value of the summation in the coefficient for D_e is adjusted to yield the measured anomalous particle flux. An example of the results of such a calculation is shown in Fig. 6.7, where both the electron diamagnetic drift frequency and the fluctuation amplitude profiles are shown for an ICRF heated pellet fueled discharge. For the same discharge, we show in Fig. 6.8 how the different terms of the calculated anomalous particle flux compare. We see that the dominant outward flux term is the $D_e X_{1r}$ term, while both the $-\frac{3}{2} D_e X_{2r}$ and $W E_{\parallel}^{A}$ terms give an inward particle flux that is of much smaller magnitude than the outward term. As expected, the Ware pinch effect term, $W E_{\parallel}^{A}$, is insignificant.

The same fluctuation amplitude that yields the anomalous particle flux is substituted into the equation for the anomalous heat flux [Eq. (6.24)] and used to calculate the fluctuation induced heat flux. This heat flux is then compared to the power balance calculated heat flux to determine whether the relation between the particle and heat flux predicted by this theory holds. A typical example of this heat flux comparison is shown in Fig. 6.9 for the same pellet fueled discharge shown above. We see that the power balance heat flux is larger than the calculated heat flux by about a factor of 2 in the core of the discharge and by a factor of 5 or more in the outer half of the discharge. The error bars on the power balance heat flux are primarily determined by the uncertainty in ICRF power deposition to the electrons. The curve labeled $Q_e^{\mathrm{FLUCT}^*}$ in Fig. 6.9 is generated by increasing the coefficient 13/4 in Eq. (6.24) to 5, which is an estimate of the coefficient if

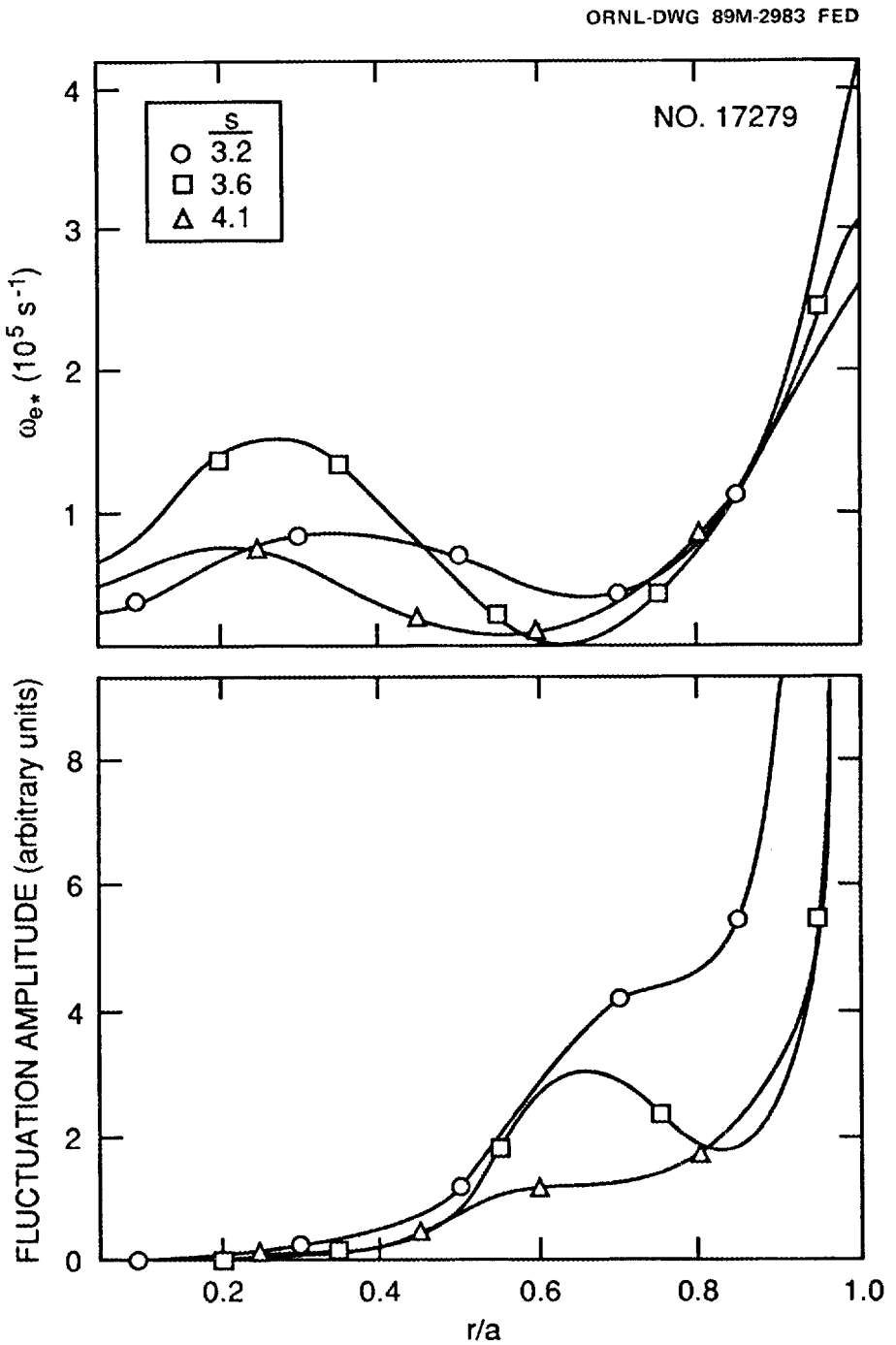

Fig. 6.7 Profiles of electron drift frequency and fluctuation amplitude calculated for an ICRF heated, pellet fueled peaked density profile discharge. The fluctuation amplitude is that necessary to account for the determined particle flux.

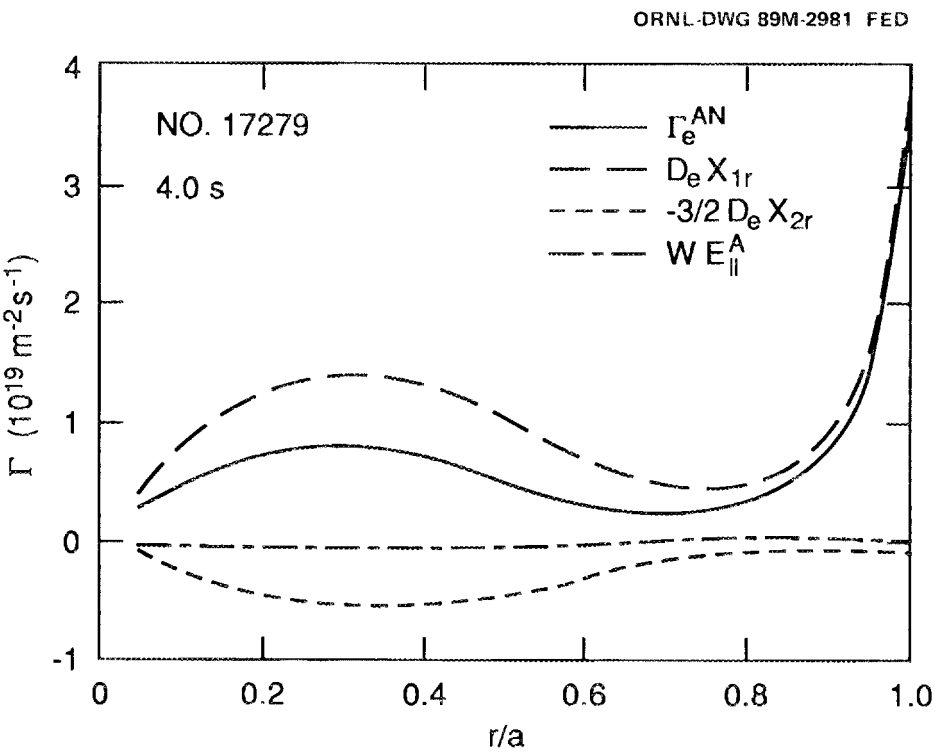

Fig. 6.8 Profiles of the relative magnitude of the particle flux terms from the quasilinear fluctuation transport theory. The terms are from the transport matrix in Eq. (6.22).

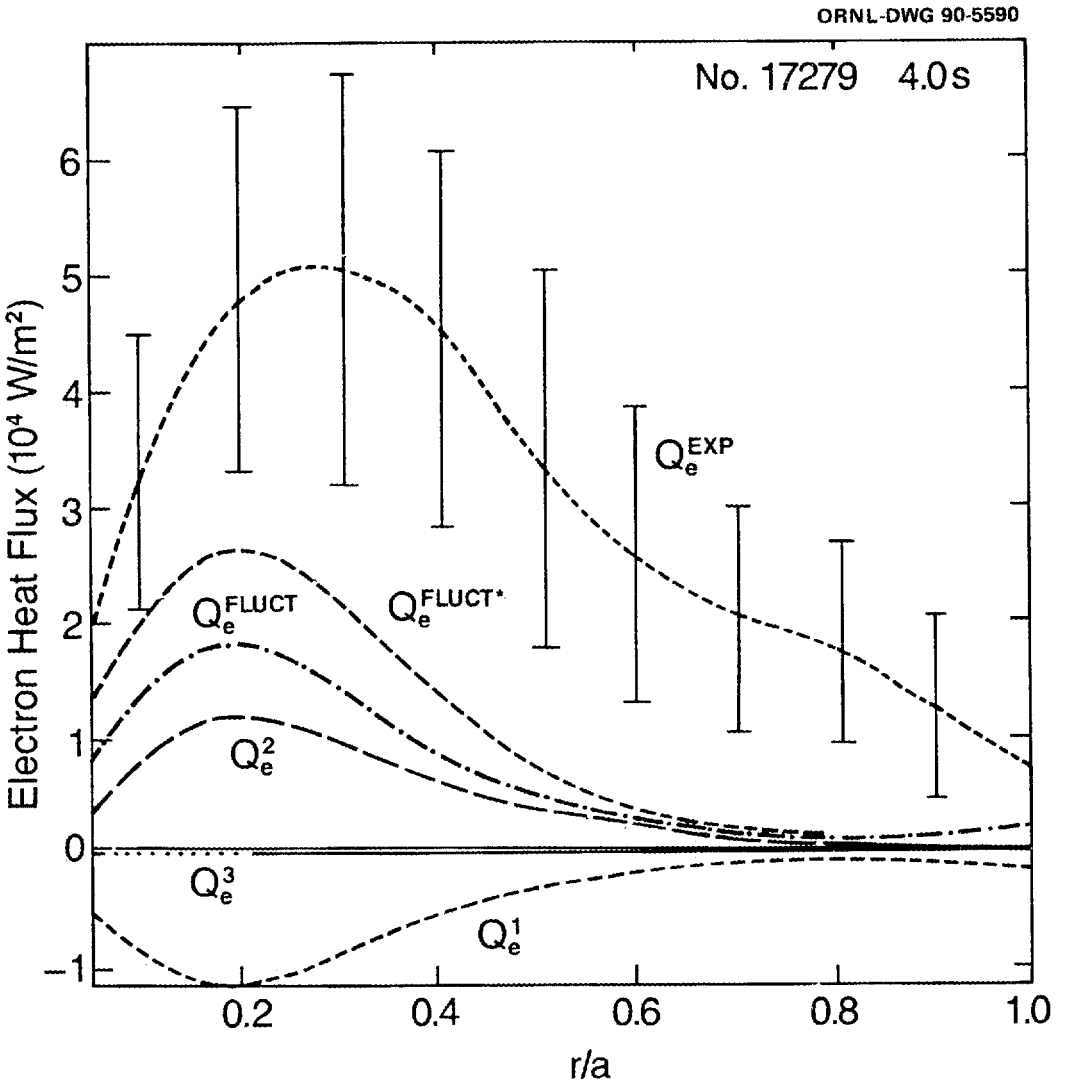

Fig. 6.9 Profiles of the experimentally determined electron heat flux and the calculated fluctuation induced heat flux. The total calculated heat flux, Q_e^{FLUCT}, and terms Q_e^1, Q_e^2, and Q_e^3, are from the neoclassical fluctuation theory of Shaing [76]. $Q_e^{\mathrm{FLUCT}^*}$ is the total calculated heat flux assuming the coefficient for Q_e^2 is increased from 13/4 to 5.

the fluctuation collisionality regime were in the banana regime (further away from the mode rational surface) [76].

Calculations of the fluctuation induced transport using this theory have been performed for over 10 of the pellet fueled JET discharges and have typically shown that electron drift wave driven electrostatic fluctuations in the quasilinear approximation do show some correlation between the determined anomalous electron particle and heat transport. The power balance electron heat flux is typically over a factor of 2–3 higher than the calculated fluctuation driven heat flux in the plasma core and a factor of 5 or more higher in the outer part of the discharge. The calculated heat flux does in general show a qualitatively similar profile shape to the power balance heat flux. In all the discharges studied, the calculated fluctuation amplitude shows a strong increase with increasing minor radius, as shown in Fig. (6.7). This is in qualitative agreement with the spatial variation in fluctuation amplitudes experimentally measured on TEXT [77].

Similar calculations have been done assuming that the fluctuation propagation is in the ion drift direction, as is the case for fluctuations driven by the ion pressure gradient driven instability (Sect. 6.1.2). The term with $\langle \omega_{mn}/m \rangle$ in Eq. (6.22) for the ion drift case has the opposite sign to that for the electron drift case due to the propagation in the opposite direction. These calculations have been performed for plasmas with relatively flat density profiles where the parameter η_i is large and the η_i-mode driven turbulence is expected to be large. The results show very little difference from the electron drift wave case since the first term of X_{1r} with $\langle \omega_{mn}/m \rangle$ in it is smaller in magnitude than the fourth term, as pointed out above.

Transport calculations utilizing quasilinear neoclassical fluctuation driven transport theory in the plateau regime indicate that electrostatic fluctuations

driven with an electron or ion drift wave spectrum are not sufficient alone to fully correlate the resulting anomalous electron particle and heat transport. Other mechanisms driving magnetic fluctuations presumably exist in parallel especially in the outer portion of the discharge, and may contribute more to the anomalous heat transport. It is also possible that the turbulence is not adequately described by a quasilinear theory or that the fluctuation collisionality is not in the plateau regime. An extension of the theory to the collisionless banana fluctuation collisionality regime is needed to determine if that more adequately describes the data.

CHAPTER 7

DISCUSSION OF RESULTS

Peaked electron density profiles are generated in JET discharges from pellet injection with central penetration. These density profiles are frequently found to slowly decay to a peaked profile on a broad pedestal. The decay of the peaked profile is sometimes accelerated by the application of ICRF heating on axis and NBI. In the cases where accelerated profile decay is seen, an enhanced level of MHD activity is measured at the plasma edge, and a broad, flat density profile quickly appears that is characteristic of all auxiliary heated limiter discharges. It is found that the neoclassical (Ware) pinch velocity is reduced when the auxiliary heating is applied due to the change in electric field and collisionality. This reduced pinch velocity appears to play a role in the peaked profile decay.

The period of the peaked density profile in sawtooth-free limiter discharges has been analyzed and the electron profile evolution modeled by the use of a neoclassical pinch velocity and a time independent diffusion coefficient that has strong increase at the radial position of the density pedestal formation near the $q = 2$ surface, as shown in Fig. 5.9. The diffusivity in the model used is more than an order of magnitude larger than the neoclassical value. This same transport model is found to be applicable in both ohmic and ICRF heated discharges although the heated case shows a slightly higher diffusivity. Calculations of the density evolution using the $(r/a)^2$-dependent diffusion coefficient suggested by Hulse [59] for TFTR ohmic discharges do not yield the observed density profile pedestal on the outer half of the minor radius.

In discharges where the peaked density profile rapidly decays to a flat one, the diffusion coefficient can be modeled as a function of local electron temperature such that the diffusivity in the core rapidly evolves from the ohmic post-pellet case to a diffusivity profile that is more nearly flat, as shown in Fig. 5.11. This rapid change in diffusivity suggests that another mechanism is present in these discharges that further accelerates the central electron density decay. In discharges where there is a clear transition from the ohmic-like transport to one in which MHD activity is observed in the external loop measurements, the profile evolution can be modeled by a transition from the ohmic-like diffusion to the temperature-dependent diffusion. The effective diffusivity determined from particle balance calculations of the electron flux agrees well with the best-case diffusive models used in the discharges that have been modeled.

A large number of particle transport models have been used to analyze a variety of JET pellet fueled discharges including a model that originated from ALCATOR-C results [61] and has been used to predict the performance of future ignition machines. This model uses $\mathrm{D} = [n_e(\mathrm{m}^{-3})/10^{19}]^{-1}$ and $v = -2\,\mathrm{D}\,r/a^2$. The results from this model, as shown in Fig. 5.14, typically yield peaked parabolic density profiles when the measured density profile is seen to remain flat in the center. If these JET results scale to smaller ignition machines now being designed, the currently predicted performance may be overestimated.

The implications of these results for future tokamaks are perhaps not as promising as one would like. First of all, the lack of a strong inward pinch velocity in JET pellet fueled discharges (either thermally driven or otherwise) leads to the observation that central deposition of pellet mass is needed to result in highly peaked profiles. Since pellet ablation is a strong function of electron temperature and has been shown on JET to have a velocity dependence similar to the neutral

shielding model, pellets with much higher speeds than those currently produced will be needed to penetrate deeply into a fusion-grade plasma. The improvement in confinement and reduction in transport coefficients has been observed to be a function of increased density peakedness. The necessity of central pellet penetration to produce peaked density profiles makes the task even more difficult in future devices, with plasma temperatures $\sim$ 10 keV, than it is in JET. Secondly, a lack in obvious confinement improvement with shallow penetrating pellets in JET makes the need for pellet fueling as a performance enhancement less certain than other experiments have shown. Further research into this area is needed to ascertain what advantages pellet fueling provides in partial penetrating conditions and what the fueling efficiency from pellets fueling is in reactor grade divertor plasmas.

Analysis of the experimentally determined anomalous fluxes has been done using the quasilinear neoclassical fluctuation transport theory [76] to compare with the relationship predicted between the anomalous particle and heat flux. Calculations have been performed for a number of different pellet fueled discharges and have typically shown that electron drift wave driven electrostatic fluctuations in the quasilinear approximation show some qualitative agreement with the theoretical relationship predicted between the anomalous electron particle and heat transport. The experimental power balance heat flux is typically a factor of 2–3 higher than the calculated fluctuation driven heat transport in the core of the discharge but shows a qualitatively similar profile shape. An anomalous inward pinch driven by temperature gradients that is predicted from this theory is not very significant when compared to the diffusive transport. An enhancement to the Ware pinch due to fluctuations is also very small compared to the neoclassical value. The relatively small inward particle flux calculated from this neoclassical

fluctuation theory supports the modeling results of the density evolution, which shows good agreement without a large anomalous inward pinch. Also, the fluctuation amplitude calculated to yield the anomalous particle flux increases with minor radius, as shown in Fig. 6.7. This agrees qualitatively with measurements of the spatial variation in fluctuation amplitude on TEXT [77].

CHAPTER 8

SUMMARY AND CONCLUSIONS

The pellet fueling experiments on JET have shown that the fueling efficiency of pellet injection is much greater than that of edge fueling. The pellet fueling efficiency is near 100% with ohmic heating; however, it is seen to drop to $\sim$ 60% during auxiliary heating. This implies that edge ablation of the pellet may be enhanced by both neutral beam injection and ICRF heating. Future reactor-relevant machines may need to be able to handle the extra fuel exhaust from pellet fueling during auxiliary heating. The electron density is found to peak dramatically only when the pellet penetrates near or beyond the plasma magnetic axis and shows no increase in peaking with partial penetrating pellets. This implies that a strong inward particle pinch does not exist in the core of JET plasmas. The desirability of peaked density profiles then implies that for future reactor-grade machines, more exotic pellet injection techniques will be required to obtain central pellet penetration and peaked density profiles.

Particle transport analysis of JET sawtooth-free discharges has shown that the density evolution following peaked profiles from pellet injection can be modeled with a neoclassical pinch velocity and a diffusion coefficient that is low in the core and increases steeply at the radius of the density plateau (near the $q = 2$ surface). This type of transport model works in both ohmic and central ICRF heated discharges that have low levels of MHD activity. Some of the auxiliary heated cases show rapid central density decay, which is correlated with higher levels of edge measured MHD activity. The profile evolution in these discharges can be modeled with a temperature-dependent diffusion coefficient and the neoclassical

pinch velocity. Discharges with noncentral pellet penetration show no significant density peaking and cannot be modeled with the same transport models as the peaked profile cases.

The scaling of the determined particle transport diffusion coefficient shows that there is a strong correlation of lower electron particle and thermal diffusivity in the core region of the plasma with increased density profile peakedness. The particle diffusivity also shows an increase with the local parameter η_e. It is possible that suppression of η_i-modes in the plasma core during peaked profile periods is responsible for the improvement observed in particle and energy confinement. It is clear, however, that if η_i turbulence is being suppressed, then other mechanisms are responsible for the underlying anomalous electron transport.

Transport analysis utilizing the theory of quasilinear neoclassical fluctuations in the plateau regime indicates that electrostatic fluctuations driven with an electron or ion drift wave spectrum are not sufficient alone to fully explain the experimental relationship between the anomalous particle and heat transport, especially in the outer half of the plasma. Other mechanisms driving magnetic fluctuations presumably exist in parallel and may contribute more to the anomalous heat transport.

Recommended future work consists of further analysis into the mechanisms behind the anomalous transport. Measurements are needed of density and potential fluctuations in the interior of JET and can be made with various electromagnetic scattering techniques. These measurements would make it possible to determine what kind of fluctuation spectrum exists in the JET plasmas and what effect pellet injection and peaked density profiles have on them. Further detailed measurements can also be made of the magnetic fluctuations detected at the edge of the plasma. Correlation of such fluctuation measurements with the determined

transport may shed more light on the mechanisms behind the anomalous particle and thermal transport. Without such measurements, one can only speculate that the reduced particle diffusivity seen after pellet injection with central deposition is the result of a damping of one or more fluctuation mechanisms.

LIST OF REFERENCES

[1] Spitzer, L., Grove, D.J., Johnson, W.E., Tonks, L., Westendorp, W.F., "Problems of the Stellarator as a Useful Power Source", USAEC Report NYO-6047 (1954).

[2] Artsimovich, L.A.,"Tokamak Devices", *Nucl. Fusion* **12**, 215 (1972).

[3] Furth, H.P., "Tokamak Research", *Nucl. Fusion* **15**, 487 (1975).

[4] Wesson, J.A., *Tokamaks*, Oxford University Press, Oxford, 1987.

[5] Miyamoto, K., *Physics for Nuclear Fusion*, MIT Press, Cambridge, Mass., Revised edition, 1989.

[6] Milora, S.L., "Review of Pellet Fueling", *J. Fusion Energy* **1**, 15 (1981).

[7] Kaufmann, M., "Review on Plasma Fueling", *Plasma Phys. Controlled Fusion* **28**, 1341 (1986).

[8] Foster, C.A., Colchin, R.J., Milora, S.L., Kim, K., Turnbull, R.J., "Solid Hydrogen Pellet Injection into the ORMAK Tokamak", *Nucl. Fusion* **17**, 1067 (1977).

[9] Milora, S.L., Foster C.A., Edmonds, P.H., "Hydrogen Pellet Fueling Experiments on the ISX-A Tokamak", *Phys. Rev. Lett.* **42**, 97 (1979).

[10] Milora, S.L., et al., "Results of Hydrogen Pellet Injection into ISX-B", *Nucl. Fusion* **20**, 12 (1980).

[11] Milora, S.L., Schmidt, G.L., Houlberg, W.A., et al., "Pellet Injection into PDX Diverted Plasmas", *Nucl. Fusion* **22**, 10 (1982).

[12] Greenwald, M., Gwinn, D., Milora, S., et al., "Energy Confinement of High-Density Pellet-Fueled Plasmas in the Alcator C Tokamak", *Phys. Rev. Lett.* **53**, 352 (1984).

[13] Milora, S.L., Schmidt, G.L., et al., "Confinement of High-Density Pellet-Fueled Discharges in TFTR", *Plasma Phys. and Contr. Fusion* **28**, 1435 (1986).

[14] Schmidt, G.L., Milora, S.L., et al., "Pellet Injection Results During TFTR Ohmic and Neutral Beam Heating Experiments", in *Plasma Physics and Controlled Nuclear Fusion Research (1986)*, (Proc. 11th Int. Conf., Kyoto, 1986), Vol. 1, IAEA, Vienna (1987) 171.

[15] Kaufmann, M., Büchl, K., et al., "Pellet Injection with Improved Confinement in Asdex", *Nucl. Fusion* **28**, 827 (1988).

[16] Vlases, G.C., Gruber, O., Kaufmann, M., Büchl, K., et al., "Quasi-Stationary Pellet Fueled Ohmic Discharges with Medium Density in ASDEX ", *Nucl. Fusion* **27**, 351 (1987).

[17] Sengoku, S., et al., "Improvement of Energy Confinement Time by Continuous Pellet Fueling in Beam-Heated Doublet III Limiter Discharges", *Nucl. Fusion* **25**, 1475 (1985).

[18] Schissel, D.P., et al., "Results of Pellet Fuelled Discharges on the Doublet III Tokamak", *Nucl. Fusion* **27**, 1063 (1987).

[19] TFR Group, "Pellet Injection Experiments on the TFR Tokamak", *Nucl. Fusion* **27**, 12 (1987).

[20] Parks, P.B., Turnbull, R.J., Foster, C.A., "A Model for the Ablation Rate of a Solid Hydrogen Pellet in a Plasma", *Nucl. Fusion* **17**, 539 (1977).

[21] Parks, P.B., Turnbull, R.J., "A Model for the Ablation Rate of a Solid Hydrogen Pellet in a Plasma", *Phys. Fluids* **21**, 1735 (1978).

[22] Milora, S.L., Foster, C.A., "A Revised Neutral Gas Shielding Model for Pellet-Plasma Interactions", *IEEE Trans. Plasma Sci.* **PS-6**, 578 (1978).

[23] Kaufmann, M., Lackner, L., Lengyel, L., Schneider, W., "Plasma Shielding of Hydrogen Pellets", *Nucl. Fusion* **26**, 171 (1986).

[24] Houlberg, W.A., Milora, S.L., Attenberger, S.E., "Neutral and Plasma Shielding Model for Pellet Ablation", *Nucl. Fusion* **28**, 595 (1988).

[25] Watkins, M.L., Houlberg, W.A., Cheetham, A.D., Gondhalekar, A., Granetz, R., Hendriks, F., O'Rourke, J., Stubberfield, P.M., "A Model for Pellet Ablation in JET", in *Proc. 14th Eur. Conf. on Cont. Fusion and Plasma Heating*, Madrid, 1987, Europhys. Conf. Abstracts, EPS (1987), Vol. 11D, Part I, p. 201.

[26] Büchl, K., Vlases, G.C., et al., "Correlation of Pellet Penetration Depths on ASDEX for Ohmic and Auxiliary Heated Discharges", *Nucl. Fusion* **27**, 1939 (1987).

[27] Rebut, P.H., Keen, B.E., "The JET Experiment: Evolution, Present Status, and Prospects", *Fusion Technology* **11**, 13 (1987).

[28] Combs, S.K., Milora, S.L., Baylor, L.R., Foust, C.R., Gethers, F.E. , Sparks, D.O., "A Three Barrel Pneumatic Repeating Pellet Injector for Plasma Fueling of the Joint European Torus", *J. Vac. Sci. Technol. A* **6** (3), (1988).

[29] Milora, S.L., Combs, S.K., Baylor, L.R., Foust, C.R., Gethers, F.E., "Design of a Repeating Pneumatic Pellet Injector for the Joint European Torus", in *Proc. 12th Symposium on Fusion Engineering*, Monterey, 1987 (Institute of Electrical and Electronics Engineers, New York, 1987), Vol. 2, p. 784.

[30] Souers, C.J., *Properties of Hydrogen for Nuclear Fusion*, University of California Press, Berkeley, CA (1986).

[31] Kupschus, P., Bailey, W., Gadeberg, M., Hedley, L., Twynam, P., Szabo, T., Evans, D.,"The JET Multi-Pellet Injector Launcher - Machine Interface", in *Proc. 12th Symposium on Fusion Engineering*, Monterey, 1987 (Institute of Electrical and Electronics Engineers, New York, 1987), Vol. 2, p. 788.

[32] Baylor, L.R., Burris, R.D., Greenwood, D.E., Stewart, K.A., "Design and Implementation of a Control and Data Acquisition System for Pellet Injectors", in *Proc. of the 11th Symposium on Fusion Engineering*, Austin, 1985 (Institute of Electrical and Electronics Engineers, New York, 1985), Vol. 2, pp. 602–604.

[33] Burris, R.D., Baylor, L.R., Greenwood, D.E., Stewart, K.A., "Design and Implementation of a Control System for a Deuterium Pellet Injector", *Rev. Sci. Instrum.* **57**, 1901 (1986).

[34] Bailey, W., Kupschus, P., Gadeberg, M., "Diagnostics for the JET Multi-Pellet Injector", Fusion Technology 1988: *Proc. 15th Symposium*, Utrecht, Netherlands (1988), Vol. 1, p. 720.

[35] Stott, P.E., "Review of JET Diagnostics and Results", in "Course on Basic and Advanced Fusion Plasmas – Diagnostic Techniques", Varenna, Sept. 1986, EUR 8351-IIEN, Vol. II, Pergamon Press, Oxford (1987).

[36] Braithwaite, G., et al., "The Multichannel Far Infared Interferometer (KG1) on JET", JET-IR(85)08, unpublished (1985).

[37] Costley, A.E., et al., "Integrated Electron Temperature and Density Measurements on JET", in *Proc. 15th Eur. Conf. on Controlled Fusion and Plasma Heating*, Dubrovnik, 1988, Europhys. Conf. Abstracts, EPS (1988), Vol. 12B, Part III, p. 1119.

[38] Veron, D., in "Diagnostics for Fusion Reactor Conditions", Varenna, Sept. 1982, EUR 8351 - IIEN, Vol.II, Pergamon Press, Oxford (1983), pp.283-293.

[39] Hutchinson, I.H., *Principles of Plasma Diagnostics*, Cambridge University Press, Cambridge, 1987.

[40] Christiansen, J.P., "Integrated Analysis of Data from JET", *J. Comput. Phys.* **73**, 85 (1987).

[41] The JET Team, "Heating of Peaked Density Profiles Produced by Pellet Injection in JET", in *Plasma Physics and Controlled Nuclear Fusion Research* (Proc. 12th Int. Conf. Nice, 1988), Vol. 1, IAEA, Vienna (1989), 171.

[42] Goldston, R.J., "Energy Confinement Scaling on Tokamaks: Some Implications of Recent Experiments with Ohmic and Strong Auxiliary Heating", *Plasma Phys. Controlled Fusion* **26**, 87 (1984).

[43] Morgan, P.D., et al.,"Studies of Visible Impurity Radiation from JET Plasmas During Heating and Fuelling Experiments", *Proc. 16th Eur. Conf. on Controlled Fusion and Plasma Heating*, Venice, 1989, Europhys. Conf. Abstracts, EPS (1989), Vol. 13B, Part I, p. 95.

[44] Roth, J.R., *Introduction to Fusion Energy*, Ibis Publishing, Charlottesville, VA 1986.

[45] Stacey, W.M., *Fusion Plasma Analysis*, John Wiley & Sons, New York, 1981.

[46] Hinton, F.L., Hazeltine, R.D., "Theory of Plasma Transport in Toroidal Confinement Systems", *Rev. Mod. Phys.* **48**, 239 (1976).

[47] Kadomstev, B.B., Pogutse, O.P., "Trapped Particles in Toroidal Magnetic Systems", *Nucl. Fusion* **11**, 67 (1971).

[48] Ware, A.A., "Pinch Effect for Trapped Particles in a Tokamak", *Phys. Rev. Lett.* **25**, 15 (1970).

[49] Callen, J.D., "Physics Models Used to Describe Plasma Confinement and Heating", JET-IR(87)07, unpublished (1987).

[50] Hirshman, S.P., Sigmar, D.J., "Neoclassical Transport of Impurities in Tokamak Plasmas", *Nucl. Fusion* **21**, 1079 (1981).

[51] TFR Group, "Light Impurity Transport in the TFR Tokamak: Comparison of Oxygen and Carbon Line Emission with Numerical Simulations", *Nucl. Fusion* **22**, 1173 (1982).

[52] Haas, F.A., Thyagaraja, A., "The Nature of Turbulent Particle Transport in Toroidal Plasma Confinement", submitted to *European Phys. Lett.* (1989).

[53] Ritz, Ch.P., Powers, E.J., Rhodes, R.D., et al., "Advanced Plasma Fluctuation Analysis Techniques and Their Impact on Fusion Research", *Rev. Sci. Instrum.* **59**, 1739 (1988).

[54] Keilhacker, M., et al., "H-Mode Confinement in JET", in *Proc. 14th Eur. Conf. on Controlled Fusion and Plasma Physics*, Madrid, 1987, Europhys. Conf. Abstracts, EPS 1339 (1987), Vol. 11D, Part III, p. 1339.

[55] Simonini, R., Taroni, A., " 3-D Monte-Carlo Computations of the Neutral Temperature and Density Distribution in JET Discharges", in *Proc. 13th Eur. Conf. on Controlled Fusion and Plasma Physics*, Schliersee, 1986, Europhys. Conf. Abstracts, EPS (1986), Vol. 10D, Part I, p. 164.

[56] Lao, L.L., Hirshman, S.P., Wieland, R.M., "Variational Moment Solution to the Grad-Shrafranov Equation", *Phys. Fluids* **24**, 1431 (1981).

[57] Hawryluk, R.J., "An Empirical Approach to Plasma Transport", *Physics of Plasmas Close to Thermonuclear Conditions*, Vol. 1, Proc. Course held in Varenna, 1979, 19 (1980).

[58] Gondhalekar, A., Cheetham, A.D., et al., "Correlation of Heat and Particle Transport in JET", in *Proc. IAEA Technical Committee Meeting on Pellet Injection and Toroidal Confinement*, Gut Ising, W. Germany, 1988, IAEA, Vienna (1989).

[59] Hulse, R.A., et al., "Particle Transport in TFTR Ohmic Pellet Injection Experiments", in *Proc. 14th Eur. Conf. on Cont. Fusion and Plasma Heating*, Madrid, 1987, Europhys. Conf. Abstracts, EPS (1987), Vol. 11D, Part I, p. 318.

[60] Gondhalekar, A., Cheetham, A.D., et al., "Control of Density Profile and Particle Exhaust in JET", *Bull. Am. Phys. Soc.* **32** (1987) 9 paper 5V9.

[61] Staumbagh, R.D., Rawls, J.M., "Anomalous Diffusion and Transport Beta Limits in Dense Tokamak Plasmas", *Nucl. Fusion* **19**, 983 (1979).

[62] Coppi, B., Sharky, N., "Model for Particle Transport in High-Density Plasmas", *Nucl. Fusion* **21**, 1363 (1981).

[63] O'Rourke, J., "Modelling of Pellet Injection Experiments with Onsager-Symmetric Transport Relations", *Nucl. Fusion* **27**, 2075 (1987).

[64] Foord, M.E., Ph.D. Thesis, "Visible Continuum Measurements on the Alcator C Tokamak: Changes in Particle Transport During Pellet Fuelled Discharges", MIT-PFC/RR-87-2, Massachusetts Institute of Technology (1987).

[65] Antonsen, T., Coppi, B., Englade, R., "Inward Particle Transport by Plasma Collective Modes", *Nucl. Fusion* **19**, 641 (1979).

[66] Behringer, K., et al., "Impurity Accumulation After Pellet Injection in JET", in *Proc. IAEA Technical Committee Meeting on Pellet Injection and Toroidal Confinement*, Gut Ising, W. Germany, 1988, IAEA Vienna (1989).

[67] Liewer, P.C., "Measurements of Microturbulence in Tokamaks and Comparisons with Theories of Turbulence and Anomalous Transport", *Nucl. Fusion* **25**, 543 (1985).

[68] Haas, F.A., Thyagaraja, A., "Conceptual and Experimental Bases of Theories of Anomalous Transport in Tokamaks", *Phys. Rep.* **143** (4), 240 (1986).

[69] Coppi, B., Rosenbluth, M.N., Sagdeev, R.Z., "Instabilities due to Temperature Gradients in Complex Magnetic Field Configurations", *Phys. Fluids* **10**, 582 (1967).

[70] Lee, G.S., Diamond, P.H., "Ion Temperature Gradient Driven Turbulence in Tokamaks", *Phys. Fluids* **29**, 3291 (1986).

[71] Brower, D.L., et al.,"Observation of a High-Density Ion Mode in Tokamak Microturbulence", *Phys. Rev. Lett.* **59**, 49 (1987).

[72] Romanelli, F., Briguglio, S., "Toroidal Semicollisional Microinstabilities and Anomalous Electron and Ion Transport", JET-P(88)31, submitted to *Phys. Fluids*.

[73] Biglari, H., Diamond, P.H., Rosenbluth, M.N., "Toroidal Ion Pressure Gradient Driven Drift Instabilities and Transport Revisited", *Phys. Fluids B* **1**, 109 (1989).

[74] Boozer, A.H., White, R.B., "Particle Diffusion in Tokamaks with Partially Destroyed Magnetic Surfaces", *Phys. Rev. Lett.* **49**, 786 (1982).

[75] Malacarne, M., Duperrex, P.A., "Turbulent Fluctuations and Confinement in JET", *Nucl. Fusion* **27**, 2113 (1987).

[76] Shaing, K.C., "Neoclassical Quasilinear Transport Theory of Fluctuations in Toroidal Plasmas", *Phys. Fluids* **31**, 2249 (1988).

[77] Wootton, A.J., et al., "Fluctuations and Anomalous Transport in Tokamaks", FRCR #340 (1989), to be published.

[78] Ames, W.F., *Numerical Methods for Partial Differential Equations*, Academic Press, New York, 2nd Ed., 1977.

[79] Press, W.H., Flannery, B.P., Teukolsky, S.A., Vetterling, W.T., *Numerical Recipes*, Cambridge Press, Cambridge, 1986.

APPENDIX A

PTRANS NUMERICAL METHODS

In this appendix we describe the PTRANS code and show the numerical methods used to solve the continuity equation. PTRANS works by starting at a known density profile and solving Eq. (5.16) for a series of time steps. The calculated density profile is then compared with the experimentally measured density profile at a number of time steps after the start of the calculation. By comparing the results for a large number of trial particle transport models [$D(\rho, t)$ and $v(\rho, t)$], it is possible to find a reasonable model fairly quickly.

For the purposes of a numerical solution, Eq. (5.16) may be written in the form

$$\frac{\partial n_i}{\partial t} = \frac{-1}{\Delta V_i}\Big(V'\nabla\rho\,\Gamma\Big)\Big|_{i-1/2}^{i+1/2} + s_i\,, \tag{A.1}$$

where the subscript i corresponds to the ith point on a radial grid. If we define a radial mesh such that the index $i = 1$ defines the magnetic axis and $i = N$ is the last closed flux surface as shown in Fig. A.1, we may write Eq. (A.1) in the following differencing scheme:

$$\frac{n_i^{j+1} - n_i^j}{\Delta t} = \frac{-1}{V_{i+1/2} - V_{i-1/2}}\Big(V'\nabla\rho\Gamma\Big)\Big|_{i-1/2}^{i+1/2} + s_i\,, \tag{A.2}$$

where the superscript j refers to the current time step and $j+1$ is the next time step that we are solving for. This differencing scheme is subject to the boundary

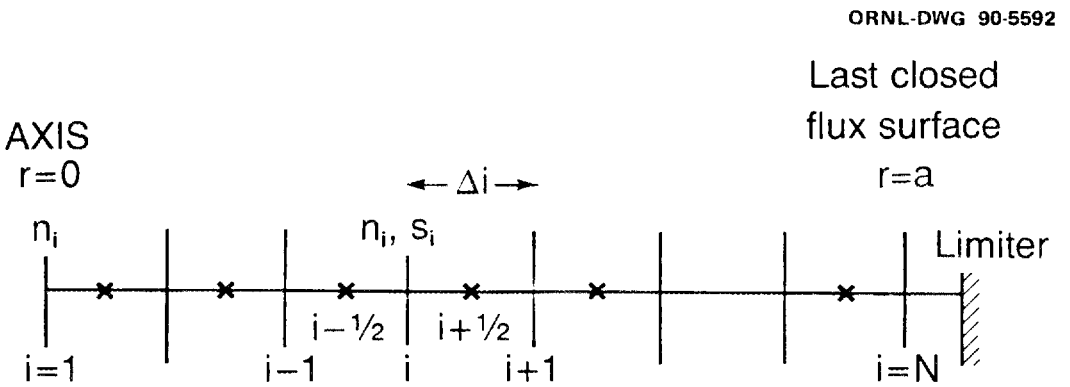

Fig. A.1 PTRANS finite difference mesh.

conditions that $n_N = 0$ and $\Gamma_{1-1/2} = 0$. If we let $\Delta V_i \equiv V_{i+1/2} - V_{i-1/2}$ then we may rewrite the differencing scheme as

$$n_i^{j+1} - n_i^j = \frac{-\Delta t}{V_{i+1/2} - V_{i-1/2}} \left(V'_{i+1/2} \nabla \rho_{i+1/2} \Gamma_{i+1/2} - V'_{i-1/2} \nabla \rho_{i-1/2} \Gamma_{i-1/2} \right) + s_i \Delta t \,. \tag{A.3}$$

We use the following differencing scheme for $\Gamma_{i+1/2}$:

$$\Gamma_{i+1/2} = -D_{i+1/2} \left[(1-\lambda) \frac{(n_{i+1}^j - n_i^j)}{(\rho_{i+1} - \rho_i)} \nabla \rho_{i+1/2} + \lambda \frac{(n_{i+1}^{j+1} - n_i^{j+1})}{(\rho_{i+1} - \rho_i)} \nabla \rho_{i+1/2} \right] + v_{i+1/2} \left[(1-\lambda) \frac{(n_{i+1}^j + n_i^j)}{2} + \lambda \frac{(n_{i+1}^{j+1} + n_i^{j+1})}{2} \right], \tag{A.4}$$

and similarly for $\Gamma_{i-1/2}$. By introducing a weighting factor λ into the differencing equation for Γ, we may adjust the relative weighting between the implicit (n^{j+1}) and explicit (n^j) terms of the differencing equation and end up with a fully implicit equation, an explicit equation, or anything in between [78]. $\lambda = 0.5$ yields the well-known Crank-Nicholson scheme and is usually the weighting factor that is used. To solve Eq. (A.3), one has to solve a set of simultaneous linear equations at each time step for the ${n_i}^{j+1}$. This is a simple problem because the system is tridiagonal. The terms in Eq. (A.3) may be grouped appropriately:

$$X_{i-1} n_{i-1}^{j+1} + X_i n_i^{j+1} + X_{i+1} n_{i+1}^{j+1} = Y_{i-1} n_{i-1}^j + Y_i n_i^j + Y_{i+1} n_{i+1}^j + {s_i}^j \Delta t, \tag{A.5}$$

where

$$X_{i-1} = \frac{\Delta t}{\Delta V_i} V'_{i-1/2} \nabla \rho_{i-1/2} \lambda \left(\frac{-D_{i-1/2}}{(\rho_i - \rho_{i-1})} \nabla \rho_{i-1/2} - \frac{v_{i-1/2}}{2} \right),$$

$$X_{i+1} = \frac{\Delta t}{\Delta V_i} V'_{i+1/2} \nabla \rho_{i+1/2} \lambda \left(\frac{-D_{i+1/2}}{(\rho_{i+1} - \rho_i)} \nabla \rho_{i+1/2} + \frac{v_{i+1/2}}{2} \right),$$

$$\begin{aligned} X_i = 1 &+ \frac{\Delta t}{\Delta V_i} V'_{i-1/2} \nabla \rho_{i-1/2} \lambda \left(\frac{D_{i-1/2}}{(\rho_i - \rho_{i-1})} \nabla \rho_{i-1/2} - \frac{v_{i-1/2}}{2} \right) \\ &+ \frac{\Delta t}{\Delta V_i} V'_{i+1/2} \nabla \rho_{i+1/2} \lambda \left(\frac{D_{i+1/2}}{(\rho_{i+1} - \rho_i)} \nabla \rho_{i+1/2} + \frac{v_{i+1/2}}{2} \right), \end{aligned}$$

$$Y_{i-1} = \frac{\Delta t}{\Delta V_i} V'_{i-1/2} \nabla \rho_{i-1/2} (1 - \lambda) \left(\frac{D_{i-1/2}}{(\rho_i - \rho_{i-1})} \nabla \rho_{i-1/2} + \frac{v_{i-1/2}}{2} \right),$$

$$Y_{i+1} = \frac{\Delta t}{\Delta V_i} V'_{i+1/2} \nabla \rho_{i+1/2} (1 - \lambda) \left(\frac{D_{i+1/2}}{(\rho_{i+1} - \rho_i)} \nabla \rho_{i+1/2} - \frac{v_{i+1/2}}{2} \right),$$

$$\begin{aligned} Y_i = 1 &+ \frac{\Delta t}{\Delta V_i} V'_{i-1/2} \nabla \rho_{i-1/2} (1 - \lambda) \left(\frac{-D_{i-1/2}}{(\rho_i - \rho_{i-1})} \nabla \rho_{i-1/2} + \frac{v_{i-1/2}}{2} \right) \\ &+ \frac{\Delta t}{\Delta V_i} V'_{i+1/2} \nabla \rho_{i+1/2} (1 - \lambda) \left(\frac{-D_{i+1/2}}{(\rho_{i+1} - \rho_i)} \nabla \rho_{i+1/2} - \frac{v_{i+1/2}}{2} \right). \end{aligned} \tag{A.6}$$

This tridiagonal set of equations may be written in matrix form as

$$\begin{pmatrix} X_{11} & X_{12} & 0 & \dots & 0 \\ X_{21} & X_{22} & X_{23} & \dots & \vdots \\ \vdots & \vdots & \ddots & \vdots & 0 \\ 0 & \dots & X_{N-1,N-2} & X_{N-1,N-1} & X_{N-1,N} \\ 0 & \dots & 0 & X_{N,N-1} & X_{NN} \end{pmatrix} \begin{pmatrix} n_1^{j+1} \\ n_2^{j+1} \\ \vdots \\ n_{N-1}^{j+1} \\ n_N^{j+1} \end{pmatrix} =$$

$$\begin{pmatrix} Y_{11} & Y_{12} & 0 & \dots & 0 \\ Y_{21} & Y_{22} & Y_{23} & \dots & \vdots \\ \vdots & \vdots & \ddots & \vdots & 0 \\ 0 & \dots & Y_{N-1,N-2} & Y_{N-1,N-1} & Y_{N-1,N} \\ 0 & \dots & 0 & Y_{N,N-1} & Y_{NN} \end{pmatrix} \begin{pmatrix} n_1^j \\ n_2^j \\ \vdots \\ n_{N-1}^j \\ n_N^j \end{pmatrix} + \begin{pmatrix} s_1^j \\ s_2^j \\ \vdots \\ s_{N-1}^j \\ s_N^j \end{pmatrix} \Delta t, \tag{A.7}$$

which can be solved by decomposition followed by forward and back substitution [79].

The code is written to solve up to 32 independent models for $D(\rho, t)$ and $v(\rho, t)$ in parallel by iterating through each model at every time step. Each of these models may include the neoclassical terms as calculated by the interpretive code QFLUX and read in by PTRANS. The geometry data used in PTRANS (ΔV, V', and $\nabla\rho$) are also calculated externally from an equilibrium magnetic representation (in QFLUX) and read in. The radial shape of the edge source $s(\rho, t)$ is obtained from external neutral deposition calculation (QFLUX) using H_α edge measurement to determine the magnitude. Optional source feedback capability built into the code can adjust the magnitude of the source profile for each model to keep the number of particles in the plasma the same as that determined from the experimental density profiles. This is used in ICRF heated plasmas when the ICRF is initially turned on since the H_α detectors used to measure the source magnitude are located away from the antennas (as shown in Fig. 2.2) and do not see the particle source from the antennae until approximately a particle confinement time later.

PTRANS is run at JET on the IBM 3090 mainframe computer in batch mode. A control namelist file that contains the controls for running the code and switches for the 32 models is embedded in the JCL file that is submitted to run the code. An output file is used for debug information and error logging. A log file is kept that is updated after every run with information about that run. The results may be stored in a PPF (JET specific postprocessed data file) for later examination of the output data, and a plot file (GHOST grid file) may be created and plotted after the run.

APPENDIX B

PTRANS SOURCE CODE LISTING

In this appendix we present the pertinent subroutines used in the particle transport modeling code PTRANS used to solve the system of equations, Eqs. (A.1)–(A.7). It is written in FORTRAN and is run on the JET IBM 3090 mainframe computer.

The PTRANS code loops through each of the transport models and loads in the transport coefficients and input data for that model as shown in the flow chart in Fig. B.1. The main computational subroutine CALDEN is called for each time step in the calculation for each transport model. The coefficients to the difference equations [Eq. (A.6)] are then calculated in the subroutine CALCOF. Then a numerical subroutine TRIDAG is called from within CALDEN and performs the matrix solution to the tridiagonal set of equations [Eq. (A.7)]. The calculated density for each point in the radial grid is then saved and the new total number of particles for that model is calculated. The measured number of particles is then calculated for that time step and saved. If source feedback is enabled, the feedback gain factor is determined for each model and used in the next time step. The variables used in the calculation are in one of several COMMON blocks which are saved for output or use in the next time step.

ORNL-DWG 90-5591

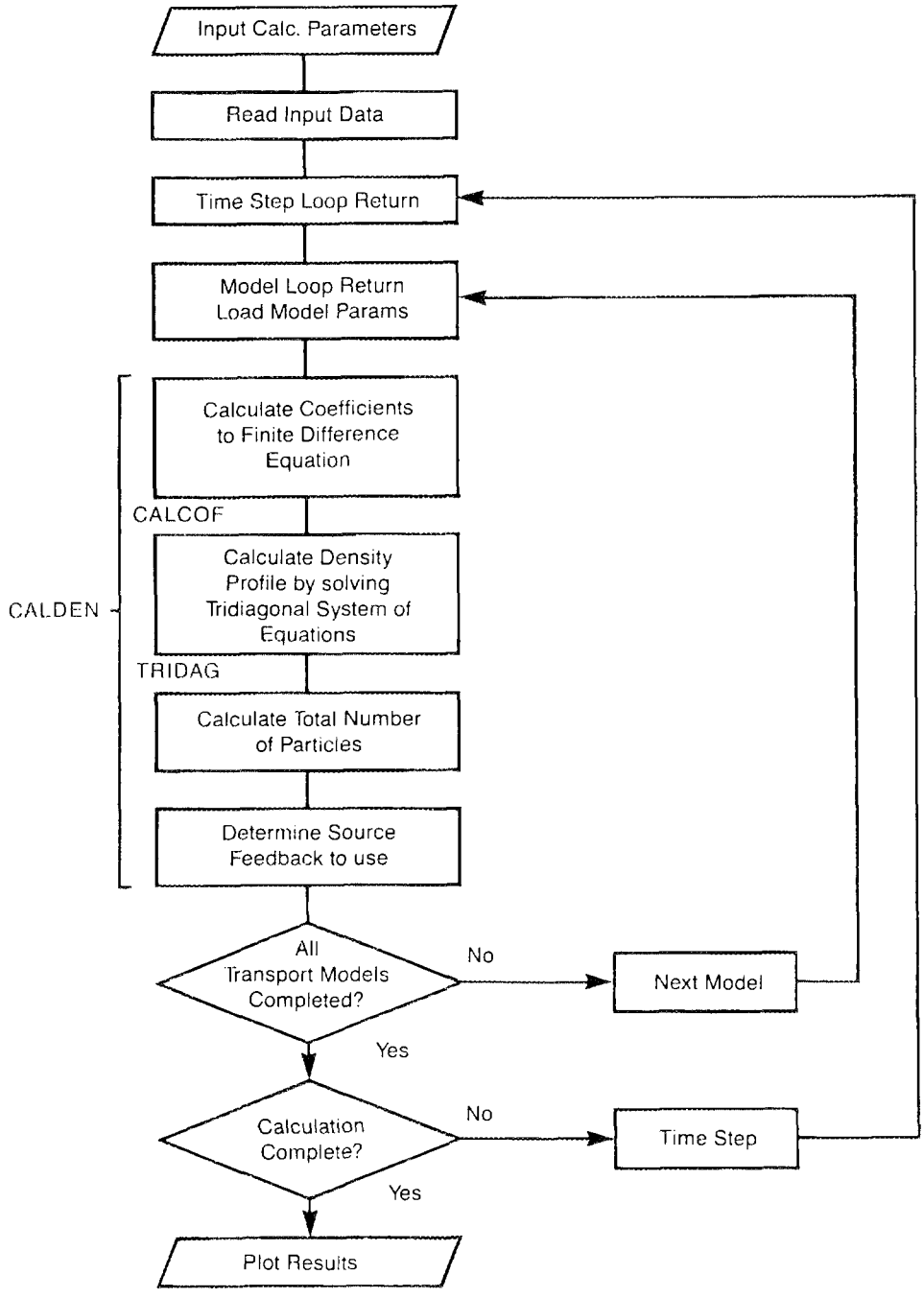

Fig. B.1 Flowchart of the particle transport modeling code PTRANS. The subroutines described in this appendix are labeled.

```
C++++++++++++++++++++++++++++++++++++++++++++++++++++++++++++++++++++++++++++
C
C     SUBROUTINE CALDEN
C
C
C Calculate new density from finite difference equation.
C See TM for description of method used.
C
C  Revisions:
C  ----------
C   1-SEP-1988    Fixed GRHO problem with Gamma.
C-----------------------------------------------------------------------
      SUBROUTINE CALDEN
C
C Include files
C
      INCLUDE(COMGVL)
      INCLUDE(COMCON)
      INCLUDE(COMGOM)
      INCLUDE(COMCAL)
      INCLUDE(COMSAV)
C
C Local data
C
      INTEGER*4 I, J, K
      REAL*4 MAXFB
      PARAMETER (MAXFB = 5.0)
C
C-----------------------------------------------------------------------
C 1. LOOP THROUGH EACH TRANSPORT MODEL
C
      DO 10 I=1,NMODEL
         IF (MERFLG(I)) GOTO 10
C
C-----------------------------------------------------------------------
C 2. LOAD IN APPROPRIATE TRANSPORT COEFFICIENTS AND INICOND FOR MODEL
C     (NOTE: V2MDL IS NEGATED HERE )
C
         DO 20 J = 1, NPSI
            NE(J) = NEMDL(J,I)
            SE(J) = SEMDL(J,I)*DELTIM
            D2(J) = D2MDL(J,I)
            V2(J) = -1.0 * V2MDL(J,I)
 20      CONTINUE
C        IF (DEBUG) THEN
C           WRITE(DUNIT,*) 'CALDEN N,S', (NE(K),SE(K),K=1,3)
C        ENDIF
```

```
C
C-----------------------------------------------------------------------
C 3. CALCULATE COEFFICIENTS TO DIFFERENCE EQUATION
C
         CALL CALCOF(IERR)
         IF (IERR.NE.0) THEN
            WRITE(DUNIT,*) 'ERROR IN CALCOF: ITSTEP, MODEL', ITSTEP, I
            MERFLG(I) = .TRUE.
            GOTO 10
         ENDIF
C
C-----------------------------------------------------------------------
C 4. CALCULATE DENSITY PROFILE
C
         CALL TRIDAG(AI, BI, CI, RE, NPRME, NPSI, IERR)
         IF (IERR.NE.0) THEN
            CALL ERRMSG('CALDEN', 'TRIDAG', NSTR, NSTR, IERR)
            WRITE(DUNIT,*) 'AI:',(AI(K),K=1,NPSI)
            WRITE(DUNIT,*) 'BI:',(BI(K),K=1,NPSI)
            WRITE(DUNIT,*) 'CI:',(CI(K),K=1,NPSI)
            WRITE(DUNIT,*) 'RE:',(RE(K),K=1,NPSI)
            MERFLG(I) = .TRUE.
            GOTO 10
         ENDIF

         NPRME(NPSI) = 1.E16
C
C-----------------------------------------------------------------------
C 5. SAVE DATA FOR THIS MODEL
C
        DO 50 J = 1,NPSI
           IF (NPRME(J).LE.0.) THEN
              NPRME(J) = 1.0E16
           ENDIF
           NEMDL(J,I) = NPRME(J)
 50     CONTINUE
C
C-----------------------------------------------------------------------
C 6. CALCULATE MODEL TOTAL NUMBER OF PARTICLES
C
        NTOTL(I) = 0.0
        STOTL(I) = 0.0
        DO 60 J = 1,NPSI-1
           NTOTL(I) = NTOTL(I) + NEMDL(J,I)*DELVOL(J)
           STOTL(I) = STOTL(I) + SEMDL(J,I)*DELVOL(J)*DELTIM
 60     CONTINUE
C
 10   CONTINUE
C
C-----------------------------------------------------------------------
C 7. CALCULATE MEASURED TOTAL NUMBER OF PARTICLES
C
        NATOTL = 0.0
        SATOTL = 0.0
        DO 70 J = 1,NPSI-1
           NATOTL = NATOTL + NEACT(J)*DELVOL(J)
           SATOTL = SATOTL + SEACT(J)*DELVOL(J)*DELTIM
 70     CONTINUE
```

```
C
C-----------------------------------------------------------------------
C 8. DETERMINE SOURCE FEEDBACK TO USE IN NEXT TIME STEP
C
        DO 80 I = 1,NMODEL
           IF (STOTL(I).LE.0.0) THEN
              SCEFB(I) = 1.
           ELSE
              SCEFB(I) = 1.+ ((NATOTL-NTOTL(I))/STOTL(I))*S1(I)
           ENDIF
           IF (SCEFB(I).GT.MAXFB) THEN
              SCEFB(I) = MAXFB
           ELSE IF (SCEFB(I).LT.0.2) THEN
              SCEFB(I) = 0.2
           ENDIF
 80     CONTINUE
C
C
C-----------------------------------------------------------------------
C
      RETURN
      END
```

```
C++++++++++++++++++++++++++++++++++++++++++++++++++++++++++++++++++++++++
C
C     SUBROUTINE CALCOF
C
C
C Calculate coefficients for terms in the finite difference eqn.
C See TM for description of method used.
C
C-----------------------------------------------------------------------
      SUBROUTINE CALCOF(IERR)
C
C Include files
C
      INCLUDE(COMGVL)
      INCLUDE(COMCON)
      INCLUDE(COMGOM)
      INCLUDE(COMCAL)
C
C Arguments
C
      INTEGER*4 IERR
C
C-----------------------------------------------------------------------
C 1. Calculate common coefficients used in terms
C
      IERR = 0
      IF (DELVOL(1).LE.0.0) THEN
         IERR = -1
         RETURN
      ENDIF
      XC1(1) = (DELTIM/DELVOL(1))*VPRIME(1)*GRHO(1)*WHTFCT
      XC2(1) = 0.
      YC1(1) = (DELTIM/DELVOL(1))*VPRIME(1)*GRHO(1)*(1.-WHTFCT)
      YC2(1) = 0.
      DO 10 I=2, NPSI
         IF (DELVOL(I).LE.0.0) THEN
            IERR = -1 * I
            RETURN
         ENDIF
         XC1(I) = (DELTIM/DELVOL(I))*VPRIME(I)*GRHO(I)*WHTFCT
         XC2(I) = (DELTIM/DELVOL(I))*VPRIME(I-1)*GRHO(I-1)*WHTFCT
         YC1(I) = (DELTIM/DELVOL(I))*VPRIME(I)*GRHO(I)*(1.-WHTFCT)
         YC2(I) = (DELTIM/DELVOL(I))*VPRIME(I-1)*GRHO(I-1)*(1.-WHTFCT)
 10   CONTINUE
```

```
C
C-----------------------------------------------------------------------
C 2. Calculate implicit terms
C
      IF (DEBUG.AND.(ITSTEP.EQ.1)) THEN
         WRITE(DUNIT,*) 'CALCOF:',(D2(J)/((RMINOR(J+1)-RMINOR(J))/
     >            GRHO(J+1)) ,V2(J),J=2,NPSI-1)
      ENDIF

      AI(1) = 0.
      CI(1) = XC1(1)*(-1.*D2(1)/((RMINOR(2)-RMINOR(1))/GRHO(2))+V2(1)/2)
      BI(1) = 1. -
     >       XC1(1)*(-1.*D2(1)/((RMINOR(2)-RMINOR(1))/GRHO(2))-V2(1)/2)
      DO 20 I=2, NPSI-1
         AI(I) = XC2(I)*(-1.*D2(I-1)/
     >          ((RMINOR(I)-RMINOR(I-1))/GRHO(I))-V2(I-1)/2.)
         CI(I) = XC1(I)*(-1.*D2(I)/
     >          ((RMINOR(I+1)-RMINOR(I))/GRHO(I+1))+V2(I)/2.)
         BI(I) = 1. -
     >           XC2(I)*(-1.*D2(I-1)/
     >          ((RMINOR(I)-RMINOR(I-1))/GRHO(I))+V2(I-1)/2.) -
     >           XC1(I)*(-1.*D2(I)/
     >          ((RMINOR(I+1)-RMINOR(I))/GRHO(I+1))-V2(I)/2.)
 20   CONTINUE
      AI(NPSI) = XC2(NPSI)*(-1.*D2(NPSI-1)/
     >     ((RMINOR(NPSI)-RMINOR(NPSI-1))/GRHO(NPSI))+V2(NPSI-1)/2.)
      CI(NPSI) = 0.
      BI(NPSI) = 1. -
     >     XC2(NPSI)*(-1.*D2(NPSI-1)/
     >     ((RMINOR(NPSI)-RMINOR(NPSI-1))/GRHO(NPSI))+V2(NPSI-1)/2.)
C
C-----------------------------------------------------------------------
C 3. Calculate explicit terms
C
      AE(1) = 0.
      CE(1) = YC1(1)*(D2(1)/((RMINOR(2)-RMINOR(1))/GRHO(2))-V2(1)/2.)
      BE(1) = 1. -
     >        YC1(1)*(D2(1)/((RMINOR(2)-RMINOR(1))/GRHO(2))+V2(1)/2.)
      DO 30 I=2, NPSI-1
         AE(I) = YC2(I)*(D2(I-1)/
     >          ((RMINOR(I)-RMINOR(I-1))/GRHO(I))+V2(I-1)/2.)
         CE(I) = YC1(I)*(D2(I)/
     >          ((RMINOR(I+1)-RMINOR(I))/GRHO(I+1))-V2(I)/2.)
         BE(I) = 1. -
     >           YC1(I)*(D2(I)/
     >          ((RMINOR(I+1)-RMINOR(I))/GRHO(I+1))+V2(I)/2.) -
     >           YC2(I)*(D2(I-1)/
     >          ((RMINOR(I)-RMINOR(I-1))/GRHO(I))-V2(I-1)/2.)
 30   CONTINUE
      AE(NPSI) = YC2(NPSI)*(D2(NPSI-1)/
     >     ((RMINOR(NPSI)-RMINOR(NPSI-1))/GRHO(NPSI))+V2(NPSI-1)/2.)
      CE(NPSI) = 0.
      BE(NPSI) = 1. -
     >      YC2(NPSI)*(D2(NPSI-1)/
     >     ((RMINOR(NPSI)-RMINOR(NPSI-1))/GRHO(NPSI))-V2(NPSI-1)/2.)
```

```
C
C-----------------------------------------------------------------------
C 4. Do matrix mult to get resultant explicit vector
C
      RE(1) = BE(1)*NE(1) + CE(1)*NE(2) + SE(1)
      DO 40 I=2, NPSI-1
         RE(I) = BE(I)*NE(I) + AE(I)*NE(I-1) + CE(I)*NE(I+1) + SE(I)
 40   CONTINUE
      RE(NPSI) = AE(NPSI)*NE(NPSI-1) + SE(NPSI)

      IF (DEBUG.AND.(ITSTEP.EQ.1)) THEN
         WRITE(DUNIT,*) 'AE,BE,CE,AI,BI,CI,RE'
         DO 50 I = 1, NPSI
            WRITE(DUNIT,*) AE(I), BE(I),
     >                     CE(I), AI(I), BI(I), CI(I), RE(I)
 50      CONTINUE
      ENDIF
C
C Return to caller
C
      RETURN
      END
```

ORNL/TM-11420
Dist. Category UC-421

INTERNAL DISTRIBUTION

1–10. L. R. Baylor
11. S. K. Combs
12. R. A. Dory
13. B. C. Duggins
14. J. L. Dunlap
15. M. J. Gouge
16. H. H. Haselton
17. W. H. Houlberg
18. T. C. Jernigan
19. S. L. Milora
20. M. Murakami
21. A. L. Qualls
22. K. C. Shaing
23. J. Sheffield
24. D. W. Swain
25. N. A. Uckan
26. R. J. Wood
27–28. Laboratory Records Department
29. Laboratory Records, ORNL-RC
30. Central Research Library
31. Document Reference Section
32. Fusion Energy Division Library
33–34. Fusion Energy Division Publications Office
35. ORNL Patent Office

EXTERNAL DISTRIBUTION

36. G. H. Neilson, Princeton Plasma Physics Laboratory, P.O. Box 451, Princeton, NJ 08543
37. Office of the Assistant Manager for Energy Research and Development, U.S. Department of Energy, Oak Ridge Operations Office, P.O. Box 2001, Oak Ridge, TN 37831
38. S. E. Attenberger (ORNL), JET Joint Undertaking, Abingdon, Oxon OX14 3EA, United Kingdom
39. W. Bailey, JET Joint Undertaking, Abingdon, Oxon OX14 3EA, United Kingdom
40. D. Beard, Plasma Technologies Branch, Division of Development and Technology, Office of Fusion Energy, Office of Energy Research, ER-531 Germantown, U.S. Department of Energy, Washington, DC 20545
41. K. H. Behringer, Max-Planck Institut für Plasmaphysik, D-8046 Garching, Federal Republic of Germany
42. J. D. Callen, Department of Nuclear Engineering, University of Wisconsin, Madison, WI 53706-1687
43. M. Chatelier, CEN/Cadarache, F-13108 St.-Paul-lez-Durance Cedex, France
44. A. D. Cheetham, JET Joint Undertaking, Abingdon, Oxon OX14 3EA, United Kingdom

45. R. W. Conn, Department of Chemical, Nuclear, and Thermal Engineering, University of California, Los Angeles, CA 90024
46. J. G. Cordey, JET Joint Undertaking, Abingdon, Oxon OX14 3EA, United Kingdom
47. N. A. Davies, Office of the Associate Director, Office of Fusion Energy, Office of Energy Research, ER-50 Germantown, U.S. Department of Energy, Washington, DC 20545
48. S. O. Dean, Fusion Power Associates, Inc., 2 Professional Drive, Suite 248, Gaithersburg, MD 20879
49. H. K. Forsen, Bechtel Group, Inc., Research Engineering, P. O. Box 3965, San Francisco, CA 94119
50. M. Gadeberg, JET Joint Undertaking, Abingdon, Oxon OX14 3EA, United Kingdom
51. T. V. George, Plasma Technologies Branch, Division of Development and Technology, Office of Fusion Energy, Office of Energy Research, ER-531 Germantown, U.S. Department of Energy, Washington, DC 20545
52. J. R. Gilleland, L-644, Lawrence Livermore National Laboratory, P.O. Box 5511, Livermore, CA 94550
53. A. Gondhalekar, JET Joint Undertaking, Abingdon, Oxon OX14 3EA, United Kingdom
54. N. Gottardi, JET Joint Undertaking, Abingdon, Oxon OX14 3EA, United Kingdom
55. R. W. Gould, Department of Applied Physics, California Institute of Technology, Pasadena, CA 91125
56. R. A. Gross, Plasma Research Laboratory, Columbia University, New York, NY 10027
57. G. W. Hammett, Princeton Plasma Physics Laboratory, P.O. Box 451, Princeton, NJ 08543
58. E. G. Harris, Department of Physics, The University of Tennessee, Knoxville, TN 37916
59. L. Hedley, JET Joint Undertaking, Abingdon, Oxon OX14 3EA, United Kingdom
60. R. A. Hulse, Princeton Plasma Physics Laboratory, P.O. Box 451, Princeton, NJ 08543
61. P. Kupschus, JET Joint Undertaking, Abingdon, Oxon OX14 3EA, United Kingdom
62. G. S. Lee, Plasma Fusion Center, Massachusets Institute of Technology, 77 Massachusetts Ave., Cambridge, MA 02139
63. D. M. Meade, Princeton Plasma Physics Laboratory, P.O. Box 451, Princeton, NJ 08543
64. D. Muir, JET Joint Undertaking, Abingdon, Oxon OX14 3EA, United Kingdom

65. E. Oktay, Division of Confinement Systems, Office of Fusion Energy, Office of Energy Research, ER-55 Germantown, U.S. Department of Energy, Washington, DC 20545
66. J. O'Rourke, JET Joint Undertaking, Abingdon, Oxon OX14 3EA, United Kingdom
67. M. Roberts, International Programs, Office of Fusion Energy, Office of Energy Research, ER-52 Germantown, U.S. Department of Energy, Washington, DC 20545
68. J. R. Roth, Department of Electrical Engineering, The University of Tennessee, Knoxville, TN 37916
69. D. P. Schissel, General Atomics, P.O. Box 85608, San Diego, CA 92138-5608
70. G. L. Schmidt, Princeton Plasma Physics Laboratory, P.O. Box 451, Princeton, NJ 08543
71. W. M. Stacey, School of Nuclear Engineering and Health Physics, Georgia Institute of Technology, Atlanta, GA 30332
72. H. S. Staten, Plasma Technologies Branch, Division of Development and Technology, Office of Fusion Energy, Office of Energy Research, ER-531 Germantown, U.S. Department of Energy, Washington, DC 20545
73. D. Steiner, Nuclear Engineering Department, NES Building, Tibbetts Avenue, Rensselaer Polytechnic Institute, Troy, NY 12181
74. B. Tubbing, JET Joint Undertaking, Abingdon, Oxon OX14 3EA, United Kingdom
75. R. Varma, Physical Research Laboratory, Navrangpura, Ahmedabad 380009, India
76. M. Watkins, JET Joint Undertaking, Abingdon, Oxon OX14 3EA, United Kingdom
77. A. J. Wootton, Fusion Research Center, University of Texas, Austin, TX 78712
78. Bibliothek, Max-Planck Institut für Plasmaphysik, Boltzmannstrasse 2, D-8046 Garching, Federal Republic of Germany
79. Bibliothek, Institut für Plasmaphysik, KFA Jülich GmbH, Postfach 1913, D-5170 Jülich, Federal Republic of Germany
80. Bibliothek, KfK Karlsruhe GmbH, Postfach 3640, D-7500 Karlsruhe 1, Federal Republic of Germany
81. Bibliotheque, Centre de Recherches en Physique des Plasmas, Ecole Polytechnique Fédérale de Lausanne, 21 Avenue des Bains, CH-1007 Lausanne, Switzerland
82. R. Aymar, CEN/Cadarache, Departement de Recherches sur la Fusion Contrôlée, F-13108 Saint-Paul-lez-Durance Cedex, France
83. Bibliothèque, CEN/Cadarache, F-13108 Saint-Paul-lez-Durance Cedex, France
84. Library, Culham Laboratory, UKAEA, Abingdon, Oxfordshire, OX14 3DB, England
85. Library, JET Joint Undertaking, Abingdon, Oxfordshire OX14 3EA, England

86. Library, FOM-Instituut voor Plasmafysica, Rijnhuizen, Edisonbaan 14, 3439 MN Nieuwegein, The Netherlands
87. Library, Institute of Plasma Physics, Nagoya University, Chikusa-ku, Nagoya 464, Japan
88. Library, International Centre for Theoretical Physics, P.O. Box 586, I-34100 Trieste, Italy
89. Library, Centro Richerche Energia Frascati, C.P. 65, I-00044 Frascati (Roma), Italy
90. Library, Plasma Physics Laboratory, Kyoto University, Gokasho, Uji, Kyoto 611, Japan
91. Plasma Research Laboratory, Australian National University, P.O. Box 4, Canberra, A.C.T. 2601, Australia
92. Library, Japan Atomic Energy Research Institute, Naka Fusion Research Establishment, 801-1 Mukoyama, Naka-machi, Naka-gun, Ibaraki-ken, Japan
93. G. A. Eliseev, I. V. Kurchatov Institute of Atomic Energy, P.O. Box 3402, 123182 Moscow, U.S.S.R.
94. V. A. Glukhikh, Scientific-Research Institute of Electro-Physical Apparatus, 188631 Leningrad, U.S.S.R.
95. I. Shpigel, Institute of General Physics, U.S.S.R. Academy of Sciences, Ulitsa Vavilova 38, Moscow, U.S.S.R.
96. D. D. Ryutov, Institute of Nuclear Physics, Siberian Branch of the Academy of Sciences of the U.S.S.R., Sovetskaya St. 5, 630090 Novosibirsk, U.S.S.R.
97. O. Pavlichenko, Kharkov Physical-Technical Institute, Academical St. 1, 310108 Kharkov, U.S.S.R.
98. Deputy Director, Southwestern Institute of Physics, P.O. Box 15, Leshan, Sichuan, China (PRC)
99. Director, The Institute of Plasma Physics, P.O. Box 26, Hefei, Anhui, China (PRC)

100–138. Given distribution as shown in DOE/OSTI-4500, Energy Research (Distribution Category UC-421)